The Characterisation of InGaN/GaN Quantum Well Light Emitting Diodes

Iestyn A. Pope

PhD Thesis

Department of Physics and Astronomy
Cardiff University

September 2004

UMI Number: U584655

UMI

Dissertation Publishing

UMI U584655

ProQuest

Abstract

By focussing on the properties of InGaN/GaN quantum well (QW) LEDs the key physical processes relevant to all InGaN/GaN light emitters are studied. These include the strength of the piezoelectric field, the important current pathways and the effect doping densities and anneal temperatures have on device performance.

Photocurrent absorption spectra, of 35Å $In_{0.1}Ga_{0.9}N$ QW LEDs, were measured for a range of reverse bias. A bias of 8.5 V was necessary to counteract the affect of the internal piezoelectric field. Using this value and an appropriate approximation for the depletion width of a p-i-n junction the calculated piezoelectric field was (1.9 ± 0.15) MVcm^{-1}, in good agreement with 1.8 MVcm^{-1} calculated using piezoelectric constants interpolated from the binaries.

The absorption spectra of 26Å wide $In_{0.16}Ga_{0.84}N$ QW LEDs exhibit a band tail extending to low photon energies whereas emission occurs from the low energy side of this band tail, suggesting emission occurs from localised potential minima.
Light-current (LI) characteristics, measured as a function of temperature, are sublinear and exhibit a distinctive temperature dependence. These characteristics are explained in terms of drift leakage which is exacerbated due to the large acceptor activation energy in Mg doped GaN. The data was simulated using a drift diffusion model and good agreement between experimental and simulated results is obtained providing the model includes the band tailing.

Emission and absorption spectra and LI characteristics were measured for 25Å $In_{0.1}Ga_{0.9}N$/GaN QW LEDs subject to four different anneal temperatures of 700, 750, 850 and 900°C. Using a drift diffusion model, incorporating different acceptor concentrations to simulate the effect of different anneal temperatures, good agreement was achieved between the trends seen in the experimental results and those produced by the simulations. This confirms the important roles drift leakage and thermal annealing have on these devices.

Acknowledgements

Contents

1 Introduction and Background

1.1 Project Aim and Thesis Outline

Commercial GaN based lasers and light emitting diodes (LEDs) are now widely available and can be seen in everyday life such as in LED traffic lights, shop lighting displays and large screens at sports grounds. Despite this, many of the fundamental properties of III − Nitrides are not known to any degree of certainty and many of the physical process occurring within the devices are not fully understood. Examples include the literature values of the theoretically calculated piezoelectric field being larger than the values determined experimentally and the emission spectra of devices which appear to be red-shifted compared to absorption spectra. Although commercial GaN based lasers are available, they are only produced by a small number of companies and, outside industry, long lifetime low threshold current lasers are yet to be realised, illustrating the difficulties involved in GaN growth technology and device processing. Therefore continuing research into III − Nitrides is essential both to improve current device performance and to further the intellectual understanding of the material system and device operation.

The initial proposal was to study the gain and recombination processes in InGaN laser structures. However, it became apparent that a number of technical issues had to be resolved before progress could be made. Therefore the revised aim, encompassed in the thesis, is to study issues relevant to all InGaN/GaN light emitters by focussing on the properties of InGaN/GaN quantum well (QW) LEDs. The key physical processes include the strength of the piezoelectric effect, the important current pathways within working devices and the effect doping densities and anneal temperatures have on device performance.

The first chapter of this thesis provides an introduction to III − Nitrides, outlining their importance and providing a review of the development of semiconductor light emitters in general and GaN based devices in particular. This is followed by a description of some of the important properties of quantum well LEDs introducing the idea of quantised energy levels, a density of states and electron

transition mechanisms and transition strength. Section three of chapter 1 is dedicated to the properties of III – Nitrides describing their crystal structure, alloy system, the effects of strain, substrates and buffer layers and parameter values. This is followed by a description of the cause of the piezoelectric effect and how it may be calculated. In the final part of chapter 1 the role of hydrogen in dopant passivation is discussed.

Since there are large differences in the literature between experimentally and theoretically derived values of the piezoelectric field, the piezoelectric field within a set of InGaN/GaN quantum well devices was derived experimentally using reverse bias photocurrent absorption. The theoretical value was also calculated using piezoelectric constants interpolated from the binary values of InN and GaN. These results are presented in chapter 2 and a comparison is made between the theortical and experimental values.

InGaN/GaN quantum well LEDs, which emit at 480nm and appear blue/green to the human eye, are characterised in chapter 3, both as a function of current and temperature. This was achieved using light-current-voltage and emission/absorption measurement techniques.

In chapter 4 it is postulated that the sublinear light-current curves and the distinctive temperature dependence, described in chapter 3, may be explained via thermally activated leakage currents through the p-doped layers. To test the validity of the postulate the light-current characteristics were simulated using a drift/diffusion model.

Finally, in chapter 5 experimental results for an InGaN/GaN laser structure, operated as an LED, are presented. The wafer from which all the devices were fabricated was cleaved into four sections and different post growth anneal temperatures were used to activate the p-type dopant in each section. The different anneal temperatures (700, 750, 850 and 900°C) mean the concentration of activated Mg acceptors is different for each set of LEDs, thus allowing an investigation into the affect anneal temperature and Mg concentration has on internal leakage currents and light output.

The thesis is concluded with a summary of experimental findings and suggestions for future work.

1.2 Introduction

In this section the importance and uses of III-nitrides are discussed and a brief review of the development of semiconductor light emitters and GaN based devices is given.

1.2.1 Why III – Nitrides are Important

The Wurtzite polytypes of AlN, GaN and InN form a continuous direct bandgap alloy system ranging from 6.2eV down to 0.9eV, potentially allowing III-nitrides to span wavelengths ranging from the infrared to the UV regions of the electromagnetic spectrum. Injection lasers operating at short wavelengths have long been desired for digital data storage and retrieval and recently they have become a commercial reality. In addition blue LEDs with phosphor coatings provide a white light source 5 times more efficient than conventional incandescent light bulbs. The large bandgap of GaN also makes it suitable for high temperature applications and solar-blind detectors, making GaN of interest for space applications. There are countless other applications such as bipolar transistors, photo-transistors, thyristors, piezoelectronics, pyroelectricity and acousto-optic modulation, to name but a few.

1.2.2 Brief History of Semiconductor Light Emitters

A thorough review of the development of the MASER and LASER is given by Bertolotti[1], from which, developments relevant to semiconductor light emitters are summarised below.

The history of semiconductor light emitters could be said to go back as far as 1907 when H. J. Round[2] discovered that placing silicon carbide in an electric field caused it to emit light. However a big jump needed to be made both intellectually and technologically before the first semiconductor light emitting diodes were realised.

From the early stages of the development of the first MASER (Microwave Amplification by Stimulated Emission of Radiation) by C. H. Townes[3] in 1954, semiconductors were considered as means of achieving stimulated emission, with Y. Watanabe et al. filing a patent for a semiconductor maser in 1957[4] (published later in 1960). In 1959 N. G. Basov et al. proposed a method for producing light by exciting a homogeneous semiconductor with electrical pulses[5], and this mechanism led to laser action several years later[6]. Basov et al. also proposed the use of a *p-n*

junction to produce stimulated emission in 1961[7], which proved to be more successful than the earlier method. Then, in 1962, Robert Hall produced the first diode laser[8]. The laser, which emitted at 840nm and was made from a GaAs *p-n* junction, required a current density 10,000Am^{-2} and produced so much heat it could only be operated pulsed at 77K[8]. At the same time several other groups also announced diode lasers with similar characteristics[9-11].

The next key development came in 1963 when Kroemer[12] suggested the double heterostructure and this led to the first room temperature diode laser in 1970[13].

Mass production of LEDs began in 1972 and the laser diodes used in compact disk players were created in 1982. This was followed in 1995 by the release of DVD players, which use a laser emitting at 650nm. The most recent breakthrough has been the development of commercial LEDs and lasers operating in the blue/violet range of the spectrum, based on the III-nitride material system. The development of III-nitrides is discussed below.

1.2.3   Brief History of GaN Development

Despite its reputation as being a new material system GaN has been investigated since the beginning of research into semiconductors as light emitters. In 1959 Grimmeiss et al. [14] employed the same technique as Johnson et al. [15] and Juza and Hahn[16] to produce small crystals of GaN for the purpose of measuring their photoluminescence spectra. However this technique only produced small needles and platelets of GaN. Large area layers of GaN were first produced in 1969, by Maruska and Tietjen, who used a chloride vapour technique to deposit GaN films on sapphire[17]. The success of Maruska and Tietjen led to a flurry of activity and in 1971 Dingle et al. [18] demonstrated stimulated emission from optically pumped GaN. This was closely followed by the demonstration of an electrically pumped Zn doped M-*i-n* (M: metal) device emitting in the blue region of the spectrum, by Pankove et al. in 1972[19], and an Mg-doped violet M-*i-n* structure in 1973, by Maruska et al. [20]. Although this initial progress was promising the production of p-type GaN proved to be elusive and, without the ability to produce p-n junctions in nitrides, researchers turned their attentions to other material, such as ZiSe and SiC, to produce blue/violet light emitters.

It took a further 15 years before Amano et al. [21, 22] managed to crack the problem of producing p-type GaN. They discovered by chance that after Low-Energy Electron Beam Irradiation (LEEBI) the previously highly resistive Mg doped GaN had become conductive. To explain this process Van Vechten et al. [23] proposed that hydrogen formed a complex with the Mg acceptor level which compensated the material; the energy of the LEEBI broke this bond producing a shallow Mg acceptor level. Investigations by Nakamura et al. [24, 25] showed the p-type material could also be achieved by thermal annealing at temperatures above 600°C (doping and the role of hydrogen is discussed in detail in section 1.6). Nakamura then went on to lead the development of GaN, producing the first high brightness (over 1 candela) InGaN/AlGaN blue LED[26]. In 1995 Nichia announced commercial green InGaN based LED. Nakamura produced the first nitride based laser and first violet nitride laser in 1997[27, 28] and in 1999 Nichia announced commercial violet laser diodes.

Although the development of nitride-based devices has expanded enormously and commercial devices are now available, many of the key parameters are still uncertain, suitable lattice-matched substrates still need to be developed and the presence of large piezoelectric fields means there is still an enormous amount of research needed before the level of understanding in the nitride material approaches that of the well-established and less complicated GaAs material system.

1.3 Properties of Semiconductor Light Emitters

1.3.1 Quantum Wells

If a semiconductor with a bandgap, Eg_1, is embedded in another semiconductor with a larger bandgap, $Eg_2 > Eg_1$, a potential minimum or well is formed. If the thickness of the embedded semiconductor, L_z, is reduced to less than or equal to λ_d (the de Broglie wavelength) for an electron, quantum mechanical effects become significant and the embedded semiconductor is referred to as a quantum well (QW). The spatial confinement of electrons in the z-direction separates the continuum of energy levels associated with a bulk material within the QW, as discussed below.

1.3.1.1 Quantised Energy Levels

The calculation of energy levels within a QW is covered in a large number of textbooks. The method adopted here is that taken by Coldren and Corzine[29]. To determine the quantised energy levels within a QW it is necessary to solve the time-independent part of Schrödinger's equation:

$$\frac{-\eta^2}{2m} \nabla^2 \psi + V\psi = E\psi$$

<div align="right">**Equation 1.1**</div>

where, m, ψ and E are the particle's mass, wavefunction and energy, and V is the potential profile of the QW. The general solution for a uniform potential, such as a QW, may be expressed as the sum of two counter-propagating plane waves,

$$\psi(r) = Ae^{ikz} + Be^{-ikz}$$

<div align="right">**Equation 1.2**</div>

$$k^2 = \frac{2m}{\eta^2}(E - V)$$

<div align="right">**Equation 1.3**</div>

As an example, take a QW of width L_z and depth V_o, symmetrical about z=0, which may be split into three regions, as shown in Figure 1.1. For $E < V_o$, region II, the general solution, Equation 1.2, may be written as

$$\psi_{II} = \begin{cases} A\cos kz & \text{(symmetric solutions)} \\ A\sin kz & \text{(anti - symmetric solutions)} \end{cases}$$

<div align="right">**Equation 1.4**</div>

where $k^2 = 2mE/\hbar^2$, and

$$\psi_{III} = Be^{-\gamma z}$$

<div align="right">**Equation 1.5**</div>

for region III where $\gamma^2 = 2m(V_0-E)/\hbar^2$. In region I $\psi_I = Be^{\gamma z}$, however due to symmetry we only need to consider the single boundary at $z = L_z/2$. Assuming the particle mass is the same in all regions we can develop a complete wavefunction by requiring that

the value and first derivative, of the constituent solutions, are equal at the boundaries (i.e. $\psi_{II} = \psi_{III}$ and $\psi'_{II} = \psi'_{III}$). For the symmetric case this gives

$$A\cos\left(\frac{kL_z}{2}\right) = B\exp\left(-\frac{\gamma L_z}{2}\right)$$

Equation 1.6

$$Ak\sin\left(\frac{kL_z}{2}\right) = B\gamma\exp\left(-\frac{\gamma L_z}{2}\right)$$

Equation 1.7

Dividing Equation 1.7 by Equation 1.6 (and similarly for the anti-symmetric solution) leads to the characteristic equations

$$k\tan\left(\frac{kL_z}{2}\right) = \gamma \qquad \text{(symmetric solution)}$$

Equation 1.8

$$k\cot\left(\frac{kL_z}{2}\right) = \gamma \qquad \text{(anti-symmetric solution)}$$

Equation 1.9

The individual energy levels may be found by plotting $k\tan(kL_z/2)$ and $k\cot(kL_z/2)$ (right-hand-side, LHS, of Equation 1.8 and Equation 1.9 respectively), and γ (right-hand-side, RHS, of Equation 1.8 and Equation 1.9) as a function of energy and noting the energies at which the RHS intersects with the LHS. Figure 1.1 shows the first few wavefunctions drawn schematically on their respective energy levels.
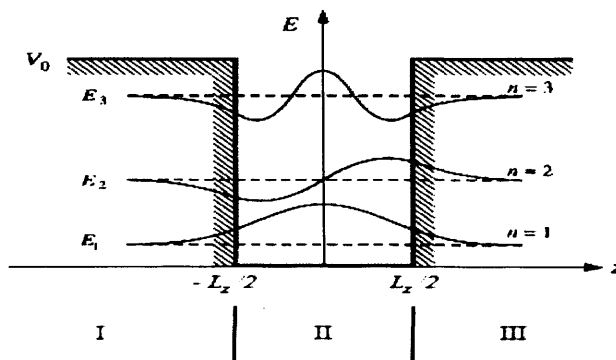
Figure 1.1 – Schematic representation of the potential energy profile of a 1-D QW. The first three wavefunctions are illustrated on their appropriate energy levels. Adapted from Coldren and Corzine[29].

1.3.2 Density of States

To calculate semiconductor properties or analyse device behaviour it is often necessary to know the carrier density, or the Fermi level energy needed to achieve a particular carrier density. The common method is to define a *density of states* (DOS), ρ, which when integrated over some range gives the number of states, N_s, in that range:

$$N_s(E) = V \int_o^E \rho(E)dE$$

<div align="right">**Equation 1.10**</div>

where E is the energy over which the number of states is to be calculated and V is the volume. Differentiating Equation 1.10 thus defines the DOS as:

$$\rho(E)dE = \frac{1}{V}dN_s(E)$$

<div align="right">**Equation 1.11**</div>

The following standard procedure can then be used to determine $\rho(E)$: firstly determine the volume in state or n-space over which the integral is to be carried out; secondly solve for n in terms of E; finally substitute these values into Equation 1.11, resulting in the following definitions

$$\rho(E) = \frac{1}{2\pi^2}\left[\frac{2m^*}{\eta^2}\right]^{3/2} E^{1/2} \qquad \text{for bulk } (m^{-3})$$

<div align="right">**Equation 1.12**</div>

$$\rho(E) = \frac{1}{L_z}\sum_i \frac{m^*}{\pi\eta^2} \mathcal{H}(E - E_i) \qquad \text{for QW } (m^{-3})$$

<div align="right">**Equation 1.13**</div>

where, $\mathcal{H}(E - E_i)$ is the Heaviside unit step function.

1.3.3 Electron Transition Mechanisms

Figure 1.2 illustrates the four important electronic transitions possible within semiconductor devices: (a) *spontaneous emission*, (b) *induced absorption*, (c) *stimulated emission* and (d) *non-radiative recombination*. A fifth transition, known as *Auger recombination*, is also possible but is insignificant within large bandgap devices and thus is not considered.
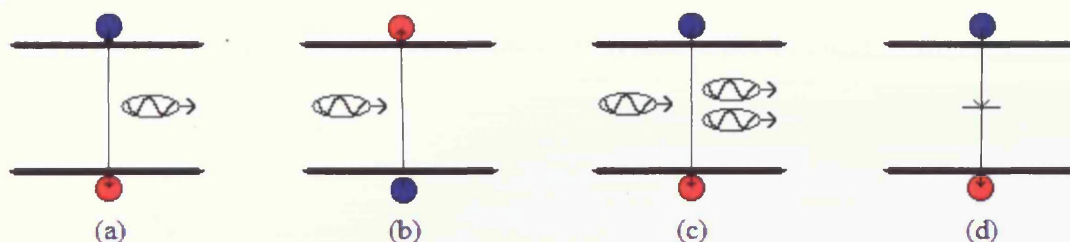
Figure 1.2 – Electron transitions between conduction band (top) and valence band (bottom); a) spontaneous recombination, b) induced absorption, c) stimulated emission and d) non-radiative recombination.

Spontaneous emission occurs when an electron in the conduction band spontaneously recombines with a hole in the valence band emitting a photon. The direction, frequency and polarisation of the emitted photon are random and thus spontaneous recombination does not produce a coherent radiation field. This is the predominant radiative mechanism in light-emitting diodes (LEDs), since photon feedback is not usually provided.

Induced absorption involves the absorption of a photon of light. The energy associated with the photon is transferred to the electron, which is excited from the valence band to the conduction band if the energy of the photon is greater than or equal to the transition energy.

Stimulated emission is similar to stimulated absorption only the position of the electron is reversed. The incident photon perturbs the system, stimulating an electron in the conduction band to recombine with a hole in the valence band. The energy the electron loses in the transition is emitted as a photon. This photon will have exactly the same frequency, polarisation and be emitted in the same direction as the incident photon. Stimulated emission is the process which provides the coherent radiation field produced by lasers.

Finally non-radiative recombination involves an electron in the conduction band transferring to the valence band via localised defects, without producing any useful

light. Since the capture of electrons and holes onto the defect state are independent processes the overall capture rate will be limited by the slowest capture process (either electron or hole capture) therefore the non-radiative recombination rate tends to be proportional to the carrier density.

The equations describing the above electron transition mechanisms are given below.

$$R_r = \int r_{sp}(h\nu)dh\nu, \quad \text{(which, within a Boltzman approximation} = Bnp)$$

<div align="right">Equation 1.14</div>

$$R_{nr} = \frac{n}{\tau_{nr}}$$

<div align="right">Equation 1.15</div>

where, R_r is the total spontaneous radiative recombination rate, $r_{sp}(h\nu)$ is the radiative recombination rate at frequency ν, B is the radiative recombination coefficient, n and p are the number of electrons and holes, R_{nr} is the total non-radiative recombination rate and τ_{nr} is the non-ratiative lifetime.

1.3.4 Electron Transition Strength

Due to the periodicity of a semiconductor crystal the wavefunction (ψ) of an electron may be defined using Bloch functions (u) as

$$\psi = e^{i\mathbf{k}\cdot\mathbf{r}}u(\mathbf{k},\mathbf{r})$$

<div align="right">Equation 1.16</div>

where, $\mathbf{r}$ and $\mathbf{k}$ are the position vector and wavevector and the Bloch function has the property that it is periodic with the crystal lattice. Each band within the semiconductor may be viewed as originating from the discrete atomic energy levels of the isolated atoms that compose the crystal[29]. In this sense the conduction band can be thought of as the remnant of the s-orbital and the three valence bands are remnants of the three p-orbitals, the corresponding Bloch "*basis*" functions may be denoted as u_s, u_x, u_y, u_z respectively. Therefore using symmetry relations the following selection rules may be defined[29]:

$$\langle u_s | p_i | u_j \rangle = 0 \qquad \text{for } i \neq j$$

<div align="right">**Equation 1.17**</div>

$$\langle u_s | p_i | u_i \rangle = M$$

<div align="right">**Equation 1.18**</div>

$$\langle u_s | p_i | \overline{u_i} \rangle = 0$$

<div align="right">**Equation 1.19**</div>

where, p_i is the momentum operator ($i = x$, y, z), u_i and $\bar{u}_i$ indicate spin-up and spin-down and M is a constant defined as the basis function momentum matrix element.

Assuming the electron wavevector (**k**) is aligned along the z-axis, the valence band Bloch functions, defined as a linear combination of the "basis" functions, are:

$$u_{hh} = -\frac{1}{\sqrt{2}} \left(u_x + i u_y \right) \qquad \overline{uhh} = \frac{1}{\sqrt{2}} \left(\overline{ux} - i \overline{uy} \right)$$

$$u_{lh} = -\frac{1}{\sqrt{6}} \left(\overline{ux} + i \overline{uy} - 2 u_z \right) \qquad \overline{ulh} = \frac{1}{\sqrt{6}} \left(u_x - i u_y + 2 \overline{uz} \right)$$

$$u_{so} = -\frac{1}{\sqrt{3}} \left(\overline{ux} - i \overline{uy} + u_z \right) \qquad \overline{uso} = \frac{1}{\sqrt{3}} \left(u_x - i u_y - \overline{uz} \right)$$

<div align="right">**Equation 1.20**</div>

where, u_{hh}, u_{lh} and u_{so} are the heavy hole (hh), light hole (lh) and split-off (so) valence band Bloch functions respectively.

The probability of an electron transition between the conduction and valence band energy levels is determined by the transition matrix element $|M_T|^2$, defined as:

$$|M_T|^2 = \left| \langle u_c | \hat{\mathbf{e}} \cdot \mathbf{p} | u_v \rangle \right|^2 \left| \langle F_2 | F_1 \rangle \right|^2$$

<div align="right">**Equation 1.21**</div>

where, $<F_2|F_1>$ is the envelope function overlap integral and $\hat{\mathbf{e}}$ is a unit polarisation vector in the direction of the field.

The lh and so valence band Bloch functions contain both spin-up and spin-down basis functions, therefore to take account of spin degeneracy the $u_c \rightarrow \bar{u}_v$ and $\bar{u}_c \rightarrow u_v$ transitions as well as the $u_c \rightarrow u_v$ and $\bar{u}_c \rightarrow \bar{u}_v$ must be summed over. However it is common to take account of spin in the density of states function, therefore the

transitions are summed over and then divided by 2, thus removing spin degeneracy form the expression for $|M_T|^2$. This approach is followed below:

$$|M_T|_v^2 = \frac{1}{2} \sum_{u_c u_c} \sum_{u_v u_v} \left| \langle u_c | \hat{e} \cdot \mathbf{p} | u_v \rangle \right|^2$$

Equation 1.22

where the envelope function overlap integral has been set equal to unity, assuming the electron and hole wavefunctions overlap exactly. By replacing the dot product, $\hat{e} \cdot \mathbf{p}$, with the expansion $e_x p_x + e_y p_y + e_z p_z$ and using the selection rules given by Equation 1.17 through to Equation 1.19 in combination with the valence band Bloch functions (Equation 1.20), the expression for $|M_T|^2$ can be reduced to:

$$\frac{|M_T|_v^2}{|M|^2} = \begin{cases} \frac{1}{2}\left(e_x^2 + e_y^2\right) = \frac{1}{2}\left(1 - \left|\hat{k} \cdot \hat{e}\right|^2\right) & \text{for } hh \text{ band} \\[2ex] \frac{1}{6}\left(e_x^2 + e_y^2 + 4e_z^2\right) = \frac{1}{2}\left(\frac{1}{3} + \left|\hat{k} \cdot \hat{e}\right|^2\right) & \text{for } lh \text{ band} \\[2ex] \frac{1}{3}\left(e_x^2 + e_y^2 + e_z^2\right) = \frac{1}{3} & \text{for } so \text{ band} \end{cases}$$

Equation 1.23

where, the substitution $e_x^2 + e_y^2 = 1 - e_z^2$ has been made, placing everything in terms of e_z and allowing us to set $e_z = \mathbf{k} \cdot \hat{e}$ (since $\mathbf{k}$ is directed along z). The use of the dot product has removed any reference to a coordinate system indicating that it is the relative orientation between the field polarisation $\hat{e}$ and the electron k-vector that is important. In a QW, where all k-vectors point along the same axis[29] due to quantum confinement, choosing the direction of confinement to correspond with the z-axis Equation 1.23 leads to the following directional dependence of the transition strength, as illustrated in Figure 1.3 below.
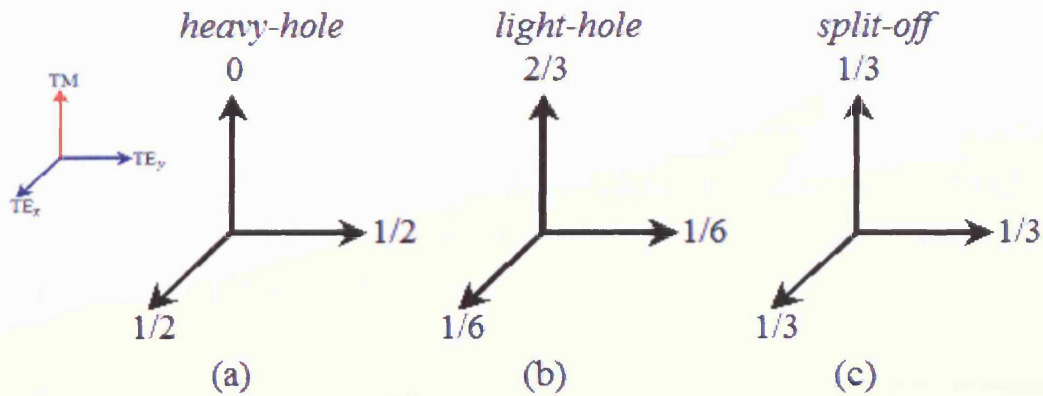
Figure 1.3 – Relative band edge transition strengths for a quantum well, a) heavy-hole transition strength, b) light-hole transition strength and c) split-off transition strength.

$|M_T|^2$ will also have a dependence on the envelope function overlap integral since in reality it is not equal to unity. However at the band edge the overlap integrals are close to unity (typically within 5-10%[29]) and would be exactly equal to unity if the conduction and valence band effective masses were identical. Also the presence of piezoelectric fields within the QW, which cause the QW to be triangular rather than square, means the envelope function overlap integral will not be equal to unity and thus should be included in the determination of $|M_T|^2$.

1.4   Properties of III – Nitrides

The natural thermodynamically stable structure for GaN and its alloys is the hexagonal wurtzite form, however it is possible to grow stable GaN, InN and AlN in the zincblende structure by utilising cubic Si, MgO and GaAs as substrates and growing on the (011) plane. Although crystallographic properties of these two structures are very similar there are noticeable differences in their material parameters. A third state is also possible, under high external pressure wurtzite undergoes a phase transformation towards the rock-salt structure, this transformation is predominantly found in ionic bonded crystals.

The experimental results discussed in the later chapters of this thesis are for devices with the common wurtzite structure, for this reason only the properties of wurtzite GaN will be discussed below.

1.4.1   Crystal Structure

Wurtzite GaN consists of two hexagonal close-packed (*hcp*) sublattices, each with one set of atoms, offset along the *c*-axis by 5/8. A stick and ball diagram of the

nitrogen *hcp* unit cell is illustrated in Figure 1.4a along with the crystallographic axes. It is common in the literature to refer to the axis normal to the basal plane as the *c*-axis, in GaN this corresponds to the [0001] direction. The three other axes (labelled a_1, a_2 and a_3 in Figure 1.4a) are all in the basal plane, each separated by an angle of $120°$ and are equal in length ($a_1 = a_2 = a_3 = a$-lattice constant). The *a* and *c* lattice constants for GaN, InN and AlN are given in Table 1.1, page 19.
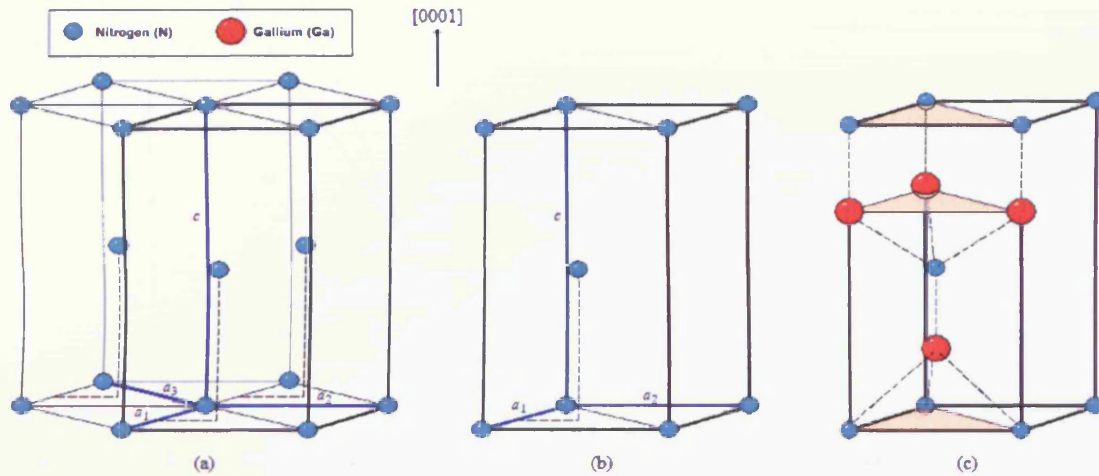
Figure 1.4 – a) hexagonal close-packed structure with principal axes highlighted in blue; the primitive unit cell is indicated by thick black lines; b) wurtzite primitive unit cell; the two basis atoms are located at ⅔,⅓,½ and 0,0,0; c) wurtzite primitive unit cell, with the inclusion of Ga atoms; the Ga–N bonds are indicated by dashed lines.

The primitive unit cell of the *hcp* is a rhomboid with two basis atoms, one at the origin and the other located at (⅔ ⅓ ½) as illustrated in Figure 1.4b. Figure 1.4c depicts the same primitive cell with the inclusion of the Ga atoms along with the atomic bonds (dashed lines), which are covalent with four tetrahedral bonds per atom. Due to the large difference in electronegativity between nitrogen and its constituents there is also a significant ionic contribution to the bond.

1.4.2   Alloys

Together, the wurtzite III – Nitride materials form a continuous direct bandgap alloy system ranging from 0.9 to 6.2eV, thus allowing the fabrication of light emitting devices which stretch from the infrared, cover the entire visible spectrum and go far into the UV. This alloy system is illustrated in Figure 1.5, along with some of the more commonly used substrates.
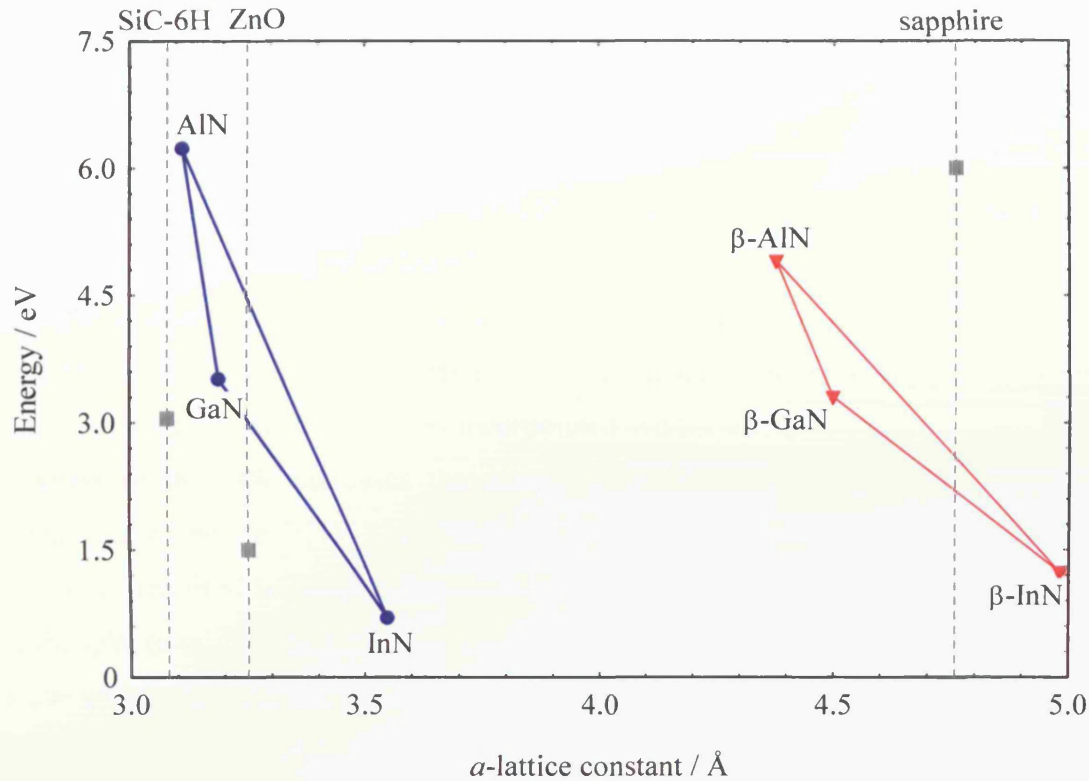
Figure 1.5 – The bandgaps and lattice constants of, wurtzite (blue circles) and zincblende (red triangles), III – Nitrides and commonly used substrates, silicon carbide (SiC-6H), zinc oxide (ZnO) and sapphire.

GaN alloys are used primarily to achieve increased device performance or attain a specific emission wavelength, however many of the important parameters such as bandgap energy are dependent on the alloy composition. The bandgap ($E_g(x)$) of the alloy $A_xGa_{1-x}N$ (where A is the material being alloyed to GaN) may be determined using the equation[30]:

$$E_g(x) = xE_g(AN) + (1-x)E_g(GaN) - bx(1-x)$$

Equation 1.24

where, x is the composition ratio and b is the bowing parameter. The above equation is a form of Vegard's law, where the bowing parameter is added to improve the fit. A similar equation may also be used to calculate other material parameters such as lattice constants, piezoelectric constants and dielectric constant, to name a few, however it is important to remember the fit may break down if different bands come into play in the process.

1.4.3 Strain

There is a considerable difference in the lattice constants of AlN, GaN and InN (Figure 1.5 and Table 1.1) therefore an epilayer made from one these materials, sandwiched between another will inevitably be under strain. We may take as an example a QW consisting of an InGaN epilayer embedded between two GaN barriers. The QW is under biaxial compression such that its basal plane lattice constant, a, is forced to equal that of the GaN barriers. For a sufficiently thin QW it is reasonable to assume that almost all the strain is incorporated within the QW, Figure 1.6. As the thickness of the QW increases the energy stored per unit area, within the QW, increases at a linear rate[31, 32]. When the energy stored in the QW is equivalent to the energy required to break a line of bonds it will become energetically favourable for the QW to relieve the strain via dislocations. Thus there exists a critical thickness below which the strained InGaN QW can be considered to be dislocation-free and thermodynamically stable.
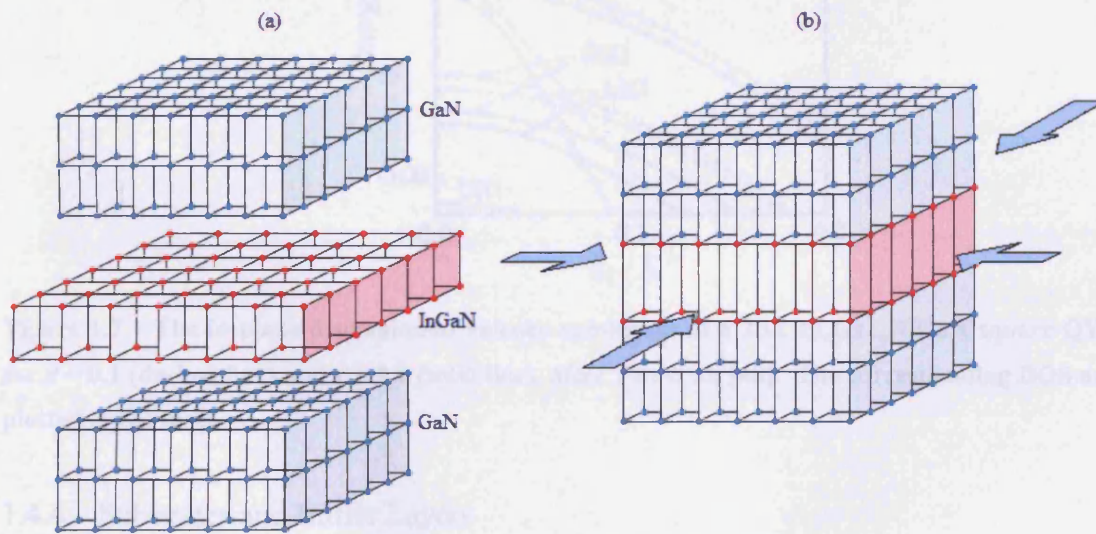
Figure 1.6 – Schematic representation of a) separate InGaN epilayer and GaN bulk layers, b) a strained InGaN epilayer embedded between GaN bulk barrier layers.

The critical thickness for an InGaN QW emitting in the green region of the spectrum has been calculated to be 30Å[33], which is large enough to allow InGaN QWs to be used in practical devices and indeed green InGaN QW LEDs are commercially available. However strain is not the only problem affecting InGaN layers. During growth In atoms are not incorporated in the epilayer swiftly but remain on the surface for long enough periods of time to travel sizable distances (~1μm), during which time they are able to seek lower energy configuration. This results in

composition fluctuations within the QW and the formation of indium rich quantum dots or quantum disks[34-39]; for very high In ratios indium–metal droplets may be formed[33].

Strain also affects the valence band structure of the epilayer. The strain breaks the symmetry of the semiconductor and splits the degeneracy of the light and heavy hole states at the Γ point, Figure 1.7. For an InGaN eplilayer under compression the mean energy gap increases and the splitting of the degeneracy at the Γ point places the *hh* above the *lh* band as shown in Figure 1.7 and anisotropy is also introduced. If the epilayer is under tension the bandgap is reduced and the *lh* moves above the *hh*.
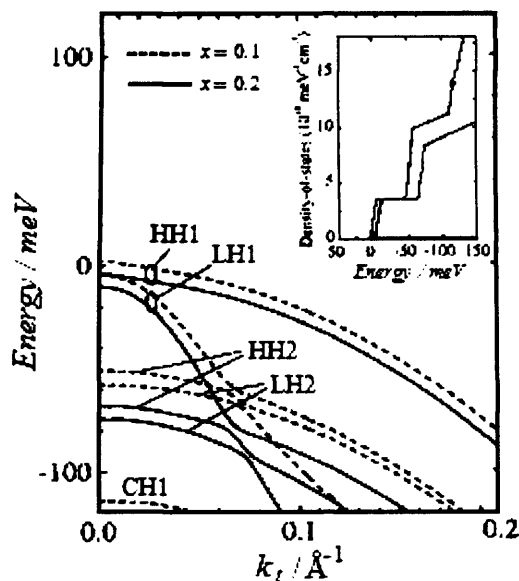
Figure 1.7 – The in-plane dispersion of valence sub-bands of a 25Å In$_x$Ga$_{1-x}$N/GaN square QW, for x = 0.1 (dashed line) and x = 0.2 (solid line), after Yeo et al. [40]. The corresponding DOS are plotted in the inset.

1.4.4   Substrates and Buffer Layers

Many of the epitaxial growth problems associated with nitrides are due to the lack of single crystalline GaN substrates, due to the high melting point of GaN (1700°C), which makes growth of GaN from a liquid melt difficult. In the absence of crystalline GaN the two main substrates used are sapphire and silicon carbide (SiC), although other material such as ZnO, MgO, InP and GaP are being examined as alternatives. Of the two main substrates silicon carbide is the more closely latticed matched to GaN, (a 3.5% lattice miss-match compared to 13% for sapphire) however SiC is very expensive, leaving sapphire as the predominant substrate for nitride growth.

Despite being the substrate of choice, there is still a large lattice mismatch (13%) and GaN epilayers grown directly on sapphire suffer from cracking and threading dislocations which propagate from the substrate to the surface. These cracks and dislocations severely degrade performance and allow metals, deposited to form contacts, to migrate deep into the device, leading to shorting of the p-n junction.

To improve the quality of the GaN epilayers a number of authors[41, 42] have demonstrated that low temperature (450 – 600°C) AlN or GaN buffer layers (or nucleation layers) drastically improve the quality of subsequent GaN films grown at temperatures above 1000°C. The purpose of the low temperature buffer layer is to optimise the transition between the sapphire and the GaN device layers, allowing the nitride layer to assume its own lattice constant with as few defects as possible. The subsequent GaN device layers can then be assumed to be strain free.

Further improvements in crystalline quality can be achieved using an epilayer of InGaN. The epilayer reduces the defect density by reducing the strain in the GaN layers[43].

1.4.4.1   III – Nitride Parameter Values

Below are summarised some of the important/useful parameters for wurtzite GaN. An excellent review of the material parameters of III – nitrides is given by Vurgaftman et al. [44] and unless specifically stated all the parameters in Table 1.1 are taken from this review. Equation 1.25 and Equation 1.26 illustrate the non-zero components of the elastic tensor and the piezoelectric strain and stress coefficient tensors used in determining the piezoelectric field, taken from Caddy[45].

$$
C_{ij} = \begin{pmatrix}
C_{11} & C_{12} & C_{13} & 0 & 0 & 0 \\
C_{12} & C_{11} & C_{13} & 0 & 0 & 0 \\
C_{13} & C_{13} & C_{33} & 0 & 0 & 0 \\
0 & 0 & 0 & C_{44} & 0 & 0 \\
0 & 0 & 0 & 0 & C_{44} & 0 \\
0 & 0 & 0 & 0 & 0 & C_{66}
\end{pmatrix}
$$

Equation 1.25

$$e_{ij} = \begin{pmatrix} 0 & 0 & 0 & 0 & e_{15} & 0 \\ 0 & 0 & 0 & e_{15} & 0 & 0 \\ e_{31} & e_{31} & e_{33} & 0 & 0 & 0 \end{pmatrix} \qquad d_{ij} = \begin{pmatrix} 0 & 0 & 0 & 0 & d_{15} & 0 \\ 0 & 0 & 0 & d_{15} & 0 & 0 \\ d_{31} & d_{31} & d_{33} & 0 & 0 & 0 \end{pmatrix}$$

Equation 1.26

Parameter	Symbol	Units	AlN	GaN	InN
Bandgap	$E_g(0)$	eV	6.23	3.51	0.9^a
Piezoelectric Constants	d_{31}	pm/V	-2.1	-1.4	-3.5
	d_{33}	pm/V	5.5	2.7	7.6
	d_{15}	pm/V	2.9	1.8	5.5
	e_{31}	C/m2	-0.5	-0.35	-0.57
	e_{33}	C/m2	1.79	1.27	0.97
	e_{15}	C/m2			
Elastic Tensors Constants	C_{11}	GPa	396	390	223
	C_{12}	GPa	137	145	115
	C_{13}	GPa	108	106	92
	C_{33}	GPa	373	398	224
	C_{44}	GPa	116	105	48
	C_{66}	GPa		123^b	
Lattice Constants	a	Å	3.112	3.189	3.545
	c	Å	4.982	5.185	5.703
Effective Mass	m_e	m_0		0.2	
	m_{hh}	m_0		1.76^c	
	m_{lh}	m_0		1.76^c	
	m_{so}	m_0		0.17	

Table 1.1 – Wurtzite III – nitride material parameters.

[a] **Matasuka et al. [46]**   [b] **Perlin et al. [47]**   [c] **Suzuki et al. [48]**

1.5 Piezoelectric Effect

The piezoelectric field generated within InGaN/GaN QWs grown on [0001] orientated sapphire substrates is considerable, of the order of 1-2 MV/cm (for indium compositions of 7 to 15%)[49-53] compared to 100kV/cm (for 10% indium)[54, 55] in InGaAs/GaAs QWs grown along the [111] axis. The aim of this section of chapter 1 is thus to define the piezoelectric effect, outlining its physical causes and secondly

to show how the field may be calculated. Detailed theory of piezoelectricity may be found in Cady[45].

1.5.1 Cause of the Piezoelectric Field

The piezoelectric effect may be defined as the generation of electricity or electric polarity within a crystal when pressure is applied, or the deformation of a crystal when placed in an electric field[45], the former being the direct effect and the latter being the converse effect. Whether a crystal exhibits piezoelectricity depends on its crystal structure and degree of symmetry, as will be discussed below.
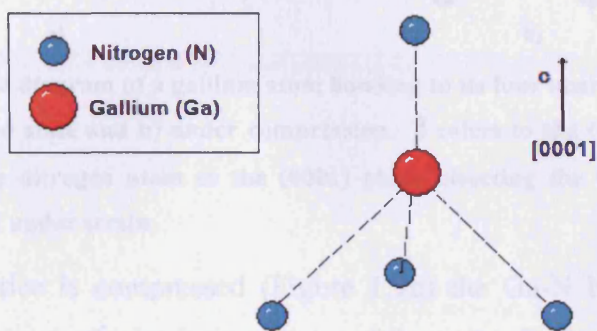
Figure 1.8 – Schematic representation of a gallium atom bonding to its four nearest neighbour nitrogen atoms in the hexagonal wurtzite formation.

Figure 1.8 gives a schematic representation of a single Ga atom bonding to its four nearest neighbour nitrogen atoms in the hexagonal wurtzite structure, as depicted in Figure 1.4. Looking at Figure 1.8 we see that in this particular orientation there are three nitrogen atoms below the Ga atom but only one above. Although in their relaxed state the net dipole moment about the Ga atom is zero, it is this lack of symmetry about the (0001) plane which ultimately leads to the piezoelectricity in wurtzite GaN.

Figure 1.9 gives a schematic representation of a Ga atom bonding to its four nearest neighbour N atoms, a) in their relaxed state and b) under compression. In the case of Figure 1.9a the distance, x, of the three N atoms below the plane is equal to one third of the Ga-N bond length, assuming the bond length to be 1.94Å[56] this gives an angle ϕ of 70.53°. Resolving the individual dipole moments about the Ga atom we see that in the relaxed state the total dipole moment about the Ga atom is zero since the negative charge felt from the N atom above the plane is balance by the negative charge of the N atoms below the plane.
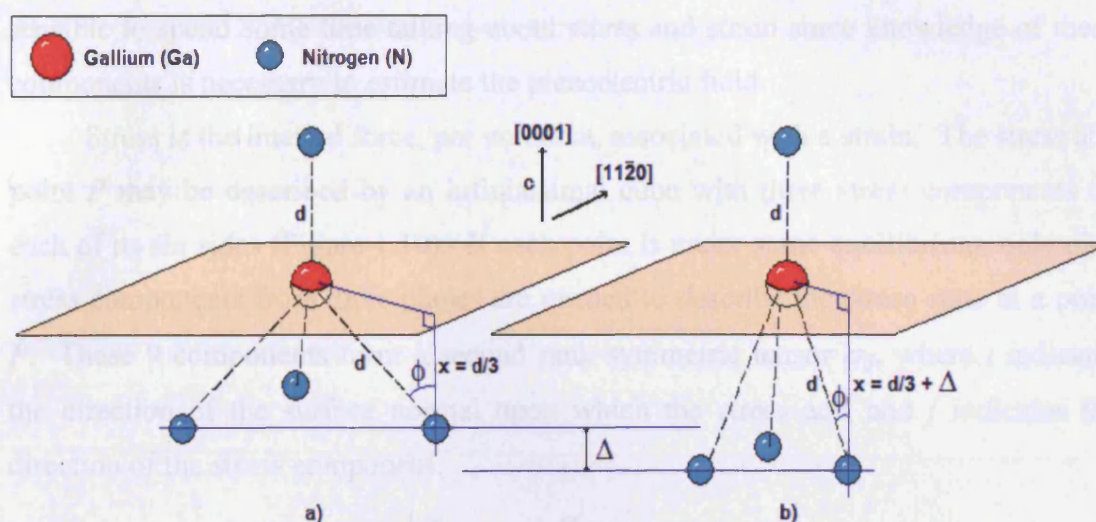
Figure 1.9 – Schematic diagram of a gallium atom bonding to its four nearest neighbour nitrogen atoms, a) in its relaxed state and b) under compression. d refers to the Ga-N bond length, x is the distance from the nitrogen atom to the (0001) plane bisecting the Ga atom and Δ is the amount x increases by under strain.

When the lattice is compressed (Figure 1.9b) the Ga-N bond length remains constant, thus to maintain the intrinsic volume of the unit cell, the unit cell is stretched normal to the plane of compression (this is known as pseudomorphic growth). Examining Figure 1.9b we see the distance x has increased by an amount Δ, resulting in a decrease in the angle φ, as compared the relaxed state. Resolving the dipole moments about the Ga atom we now see that the total dipole moment is no longer zero and the resulting field is known as the piezoelectric field (E_{pz}).

The compression, or negative strain, which gives rise to the piezoelectric field is due the lattice mismatch between the substrate and the deposited epilayer. Although this mismatch is large in the case of GaN grown on sapphire (16%) the use of a low temperature nucleation layer and a GaN buffer layer accommodates the strain, allowing the subsequent GaN layers to assume their natural structure with as few defects as possible[47]. Consequently the piezoelectric field generated in InGaN/GaN QWs is a result of the lattice mismatch between InGaN and GaN, rather than the sapphire substrate.

1.5.2   Calculating the Piezoelectric Field

The piezoelectric field within an epilayer is a result of the strain placed on the unit cell of the epilayer, as it is forced to adopt the same lattice constant as the bulk

material it is grown on. Therefore before stating the piezoelectric equation it seems sensible to spend some time talking about stress and strain since knowledge of these components is necessary to estimate the piezoelectric field.

Stress is the internal force, per unit area, associated with a strain. The stress at a point P may be described by an infinitesimal cube with three stress components on each of its six sides (Figure 1.10). If each point is under static equilibrium, only nine stress components from three planes are needed to describe the stress state at a point P. These 9 components form a second rank symmetric tensor σ_{ij}, where i indicates the direction of the surface normal upon which the stress acts and j indicates the direction of the stress component.
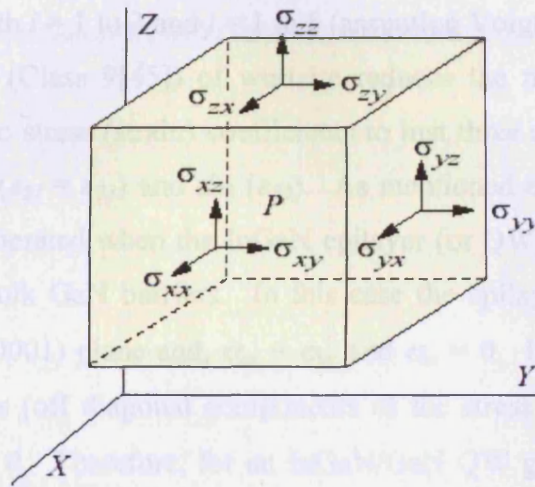
Figure 1.10 – Infinitesimal cube, indicating the 9 individual stress components, about a point P.

Consider now the deformation of the infinitesimal cube about point P. If after deformation the point P has moved to P', the strain-displacement relationship may be described as,

$$\varepsilon_{ij} = \frac{1}{2}\left(\frac{\partial u_i}{\partial x_j} + \frac{\partial u_j}{\partial x_i}\right)$$

Equation 1.27

where, u is the displacement vector, x is the coordinate, $i, j = 1, 2$ or 3 and ε_{ij} is the strain tensor which is related to the stress tensor via Hooke's law[57]:

$$\sigma_i = \sum_j C_{ij}\varepsilon_j$$

Equation 1.28

Where, C_{ij} is the elastic tensor and Voigt's notation is applied. The piezoelectric polarisation (P_i) can thus be defined either in terms of stress or strain[45] as

$$P_i = \sum_{j}^{6} d_{ij} \sigma_j \qquad \text{(Stress definition)}$$

<div align="right">**Equation 1.29**</div>

$$P_i = -\sum_{j}^{6} e_{ij} \varepsilon_j \qquad \text{(Strain definition)}$$

<div align="right">**Equation 1.30**</div>

where, d_{ij} is the piezoelectric stress coefficient tensor and e_{ij} is the piezoelectric strain coefficient tensor, with $i = 1$ to 3 and $j = 1$ to 6 (assuming Voigt's notation).

The symmetry (Class 9[45]) of wurtzite reduces the number of independent non-zero piezoelectric stress (strain) coefficients to just three and these are, $d_{15} = d_{24}$ $(e_{15} = e_{24})$, $d_{31} = d_{32}$ $(e_{31} = e_{23})$ and d_{33} (e_{33}). As mentioned earlier the piezoelectric field of interest is generated when the InGaN epilayer (or QW) is forced to adopt the same lattice as the bulk GaN barriers. In this case the epilayer experiences biaxial compression of the (0001) plane and, $\sigma_{xx} = \sigma_{yy}$ and $\sigma_{zz} = 0$. It may also be assumed that the shear stresses (off diagonal components of the stress tensor) are negligible, i.e. $\sigma_{xy} = \sigma_{xz} = \sigma_{yz} = 0$. Therefore, for an InGaN/GaN QW grown along the [0001] axis, the only non-zero component of the piezoelectric polarisation is along the z-direction or c-axis of the wurtzite crystal (a direct result of the lack of symmetry about the (0001) plane (Figure 1.9)).

$$P_z = 2d_{31}\sigma_{xx}$$

<div align="right">**Equation 1.31**</div>

Using Equation 1.28 to define the stress in terms of strain, Equation 1.31 becomes:

$$P_z = 2d_{31}\left[C_{11} + C_{12} - 2\frac{C_{13}^2}{C_{33}} \right]\varepsilon_{xx}$$

<div align="right">**Equation 1.32**</div>

ε_{xx} is simply the component of strain along the x axis which may be defined in terms of lattice constants as $\varepsilon_{xx} = (a_b - a_e)/a_e$ where, a_e and a_b are the lattice constants of the

epilayer and bulk material respectively[58]. Therefore provided the relevant piezoelectric and elastic constants are known (at present there a range of published values) the piezoelectric polarization may be calculated from the lattice constants. The strain induced piezoelectric field (E_{pz}) along the [0001] axis, in the absence of free charges, is then given by[57]:

$$E_{pz}^z = -\frac{P_z}{\varepsilon_r \varepsilon_o} = -\frac{2d_{31}}{\varepsilon_r \varepsilon_o}\left[C_{11} + C_{12} - 2\frac{C_{13}^2}{C_{33}}\right]\varepsilon_{xx}$$

<div align="right">Equation 1.33</div>

where, ε_r and ε_o are the dielectric constant of the material and the permittivity of free space. The elastic constants present in Equation 1.33 are all positive for GaN and InN where as the piezoelectric coefficient d_{31} is negative[59]; this is always true. Thus the direction of the piezoelectric field depends on whether the epilayer in under compression or tension. Compression results in a negative value of ε_{xx} and a negative field direction; tension produces a positive value of ε_{xx} and hence the direction of the piezoelectric field is positive. As discussed earlier, an InGaN/GaN QW experiences biaxial compression in the (0001) plane and thus the strain-induced piezoelectric field will be in the negative z (or c) axis, along the [0001] growth direction.
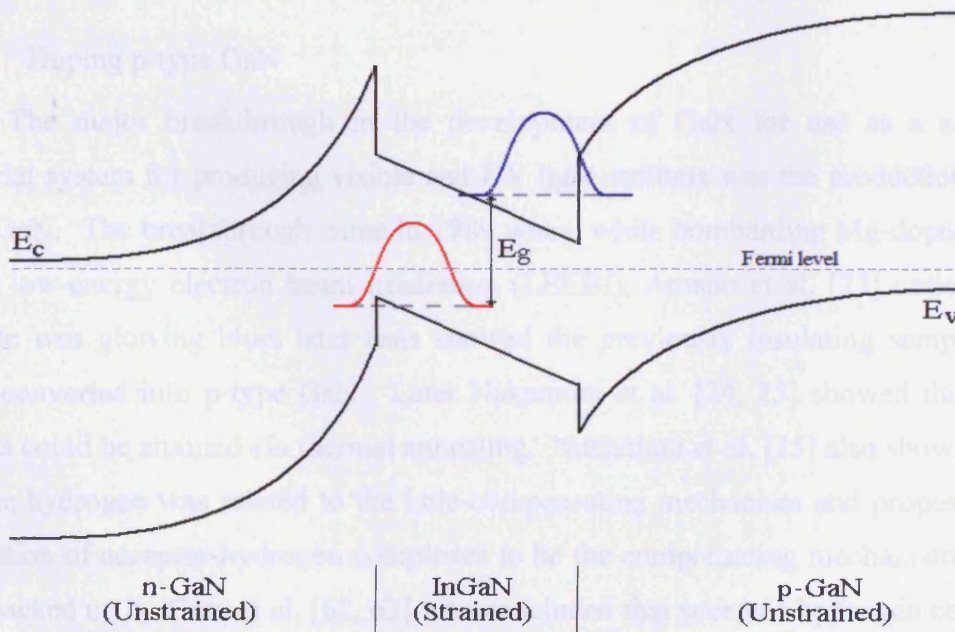

Figure 1.11 – Schematic potential energy band diagram of an InGaN/GaN QW illustrating how the piezoelectric field skews the QW, separating the electron and hole wave functions and counteracting the built in p-i-n field.

The effect the piezoelectric field has on the potential energy band diagram of an InGaN/GaN QW is illustrated in Figure 1.11. The piezoelectric field skews the QW, spatially separating the electron and hole wavefunctions and counteracting the built in p-i-n field. Therefore <F2|F1> cannot be assumed to be equal to unity in Equation 1.22 and needs to be included in the calculation of $|M_{fi}|^2$.

1.6 Doping

1.6.1 Doping n-type GaN

Traditionally Si, which substitutes a Ga atom and provides a loosely bound electron, has been used as the n-type dopant[60]. Despite being commonly used it has been shown that large doping densities of Si (greater than ~ 10^{19}cm^{-3}) can induce cracks into GaN films grown on sapphire substrates[61]. This is most likely the consequence of the small ionic radius of Si$^+$ as compared to Ga$^+$, resulting in compression in the c-axis direction.

Ge has also been used as an n-type dopant but is roughly an order of magnitude less efficient, as judged by the larger flow rates required to obtain similar electron concentration[60]. Nevertheless both Ge and Si have produced n-type GaN with doping densities as high as 10^{19}cm^{-3}.

1.6.2 Doping p-type GaN

The major breakthrough in the development of GaN for use as a suitable material system for producing visible and UV light emitters was the production of p-type GaN. The breakthrough came in 1989 when, while bombarding Mg-doped GaN using low-energy electron beam irradiation (LEEBI), Amano et al. [22] noticed the sample was glowing blue, later tests showed the previously insulating sample had been converted into p-type GaN. Later Nakamura et al. [24, 25] showed the same results could be attained via thermal annealing. Nakamura et al. [25] also showed that atomic hydrogen was related to the hole-compensating mechanism and proposed the formation of acceptor-hydrogen complexes to be the compensating mechanism. This was backed up by Gotz et al. [62, 63] who concluded that acceptor-hydrogen complex were responsible for the passivation of Mg-doped GaN. The role of hydrogen and the formation and dissociation of hydrogen complexes will be discussed below in section 1.6.3.

As well as Mg, a number of other group two elements such as, Zn, Cd, Be and Hg, have all been investigated as possible p-type dopants for GaN. However even after treatment with LEEBI or thermal annealing they all remain compensating, leaving Mg the only dopant suitable for producing p-type GaN.

The reason for the failure of other group II semiconductors to produce p-type material may be due to the fact that GaN differs considerably from other conventional group III-V semiconductors. For example, in GaAs the charge density maximum is near the bond centre (BC) due to its strong covalent character[60]. In GaN however, there is an increase in the charge density from the Ga atom towards the more electronegative N atom. This causes the charge density around the N anion to be high and nearly spherically symmetric[60]. Thus, GaN is more ionic than other group III-V semiconductors and its band structure resembles that of the II-VI semiconductors. Research into the II-VI semiconductors ZnS and ZnSe has shown that potential acceptors such as Cu, whose d electrons are resonant with the Lower Valence Band, are repelled by the d-hybridised upper valence band in an abnormally deep level, while impurities without resonance form shallow acceptors[64]. Like Cu, Zn, Cd and Hg all have d electrons and form deep levels in GaN. Mg on the other hand has no d electrons and forms sufficiently shallow acceptor levels for room temperature p-doping. While this comparison (taken from Morkoc 1999[60]) is not proof, it does suggest why the use of Mg as a dopant has succeeded in producing p-type material while the use of other group II elements has failed.

1.6.3 The Role of Hydrogen

During metal organic chemical vapour deposition (MOCVD) and hydride vapour phase epitaxy (HVPE) growth, large concentrations of hydrogen, both from the source gas (NH_3) and from the use of H_2 as a carrier gas, are unintentionally incorporated into the GaN. The result is the introduction of an impurity level within the bandgap of the semiconductor. The charge state of the hydrogen depends on the occupation of this level and thus the hydrogen can assume different charge states within the semiconductor[65].

The charge state, of which there are three (positive H^+, negative H^- and neutral H^0), determines the most favourable location of the hydrogen within the semiconductor lattice.

H^+ seeks out regions with a high electronic charge density. Calculations by Neugebauer and Van de Walle[66] have shown that essentially all positions in which the H-N bond length is about 1.02Å are approximately equal in energy and that, even though the charge density is more spherical around the N anion, the charge density still peaks in the bonds between the atoms. Thus H^+ should prefer the bond centre site, as is the case for more covalent semiconductors such as Si and GaAs. However the Ga-N bond length (1.94Å[56]) is too short to accommodate the H^+ at the BC and indeed the Ga-N bond would have to stretch by 40% to accommodate the H^+[65]. Such relaxation costs energy and is particularly costly in a hard material such as GaN. Therefore in GaN the antibonding site behind the nitrogen atom (AB_N) is the most stable site for H^+.

Similarly H^- seeks out regions with a low electronic charge density and all calculations show H^- to prefer the AB_{Ga} site.
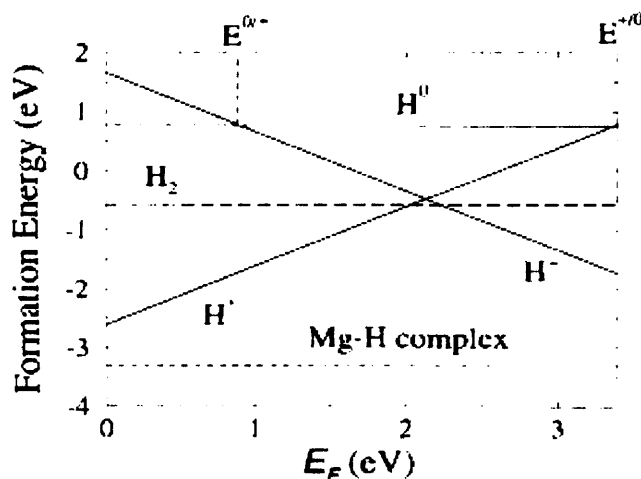
Figure 1.12 – Formation energy as a function of Fermi level for H^+, H^-, and H^0 (solid lines), for a H_2 molecule (dashed line) and for a Mg-H complex (short dashed line) in GaN. $E_F = 0$ corresponds to the top of the valence band. The formation energy is referenced to the energy of a free H atom (After Neugebauer and Van de Walle[66]).

Figure 1.12 shows a plot of the formation energy as a function of Fermi level for the various states hydrogen can assume within GaN, after Neugedauer and Van de Walle[66]. From Figure 1.12 we see that for Fermi levels below 2.1eV H^+ has a lower formation energy than H^-, and vice versa for values of E_F above 2.1eV. Low Fermi levels correspond to p-type material and high Fermi levels to n-type material. Therefore we see that H^+ is most favourable in p-type material, while H^- is most

favourable in n-type material. H° never has the lowest formation energy and this state of hydrogen is unstable in GaN.

The formation energy (E^f) also determines the concentration (c) of an impurity at a temperature (T) via the expression[65]:

$$c = N_{sites} \exp\left[-\frac{E^f}{k_B T} \right]$$

<div align="right">**Equation 1.34**</div>

where, N_{sites} is the number of sites on which the defect can be incorporated and k_B is Boltzmann's constant. From Equation 1.34 we see lower formation energies correspond to higher impurity concentrations. Therefore, high concentrations of H^+ (which has a low formation energy) will be incorporated into p-type GaN, whereas the higher formation energy of H^- means less hydrogen will be incorporated into n-type GaN.

As well as the concentration and the state of the hydrogen its mobility within the GaN lattice is also of importance. In general, hydrogen is a small and light impurity and is expected to move quite easily through a perfect lattice. While this is true for the positive charge state the migration barriers for negative charge states are usually somewhat higher. The ability of hydrogen to migrate through the crystal lattice of n-type and p-type material will be discussed below in sections 1.6.3.1 and 1.6.3.2 respectively.

1.6.3.1 The Role of Hydrogen in n-type GaN

As mentioned earlier, the charge density of the GaN crystal has a global minimum at the AB_{Ga} site, rendering it favourable for the incorporation of the H^- negatively charged impurity. Other sites within the GaN crystal are much higher in energy, consequently the energy barrier for H^- to move between equivalent sites in the lattice is quite high. The total energy surface, calculated by Neugedauer and Van de Walle[66], yields a migration barrier of 3.4eV, a value high enough to render H^- essentially immobile.

Any hydrogen present in n-type GaN could bind to the Si donors with essentially the same binding energy as that calculated for Mg-H complexes (see section 1.6.3.2) and the high migration barrier means it would not be possible to anneal the hydrogen out of the material. Fortunately the high formation energy of H^-

28

means the hydrogen concentration will be very small, and hence hydrogen has little effect on n-type doping.

1.6.3.2 The Role of Hydrogen in p-type GaN

Hydrogen is incorporated directly into the GaN crystal lattice during growth (as demonstrated by Figure 1.12) and not merely from the NH_3 ambient during cool down after growth. Although already present in p-type GaN during growth the hydrogen is not in the Mg-H complex form, as at the high temperatures used during growth the complexes are essentially dissociated.

Mg-H complexes are formed during cool down when the highly mobile hydrogen donates its electron to the Mg acceptor. As discussed earlier in this section the resultant H^+ favours the AB site of one of the N neighbours. The H^+ also likes to be close to the donated electron thus minimising electrostatic energy - the AB_N site also meets this condition. Thus, contrary to what one might expect, the Mg-H complex has a H-N bond as its main feature[66].

The formation of the Mg-H complex is said to passivate the Mg acceptor. Passivation is characterised by the presence of neutral complexes (which cause little scattering) as apposed to compensation which involves donor and acceptor atoms that are spatially separated (both of which contribute to ionised impurity scattering)[65].

In order to activate the Mg, the Mg-H complexes have to be dissociated and the hydrogen neutralised or removed from the p-type layer. Simply dissociating the Mg-H complex is not sufficient since when hydrogen leaves the acceptor it still behaves as a donor and compensates the material. A schematic illustration of the processes involved in activating the Mg acceptors is shown in Figure 1.13, after Neugebauer and Van de Walle[67], reproduced in[65].
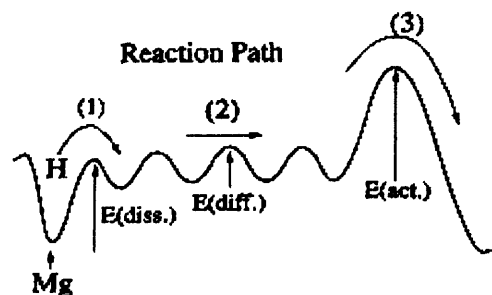

Figure 1.13 – Schematic illustration of the reaction path and energy barriers for the activation of Mg acceptors in GaN, discussed in the text. Reproduced by Van de Walle and Johnson[65], after Neugebauer and Van de Walle[67].

In order to activate the Mg acceptors the Mg-H complexes first need to be dissociated, step (1) in Figure 1.13. Neugebauer and Van de Walle estimate the dissociation energy (E(diss.)) to be 1.5eV[66] based on total energy surface calculations. The total energy surface for H^+[66] shows the barrier height H^+ needs to overcome to diffuse through the material, by moving between equivalent sites in the lattice, is only 0.7eV; step (2) in Figure 1.13. The final barrier, step (3), is the energy needed to remove the hydrogen from the material by for example, moving into the substrate or leaving through the surface. Thermal annealing provides the energy needed to carry out this process. Experimental results[62, 63, 68] show the anneal temperature needs to be 600°C or above to activate the Mg, also the higher the anneal temperature the greater the number of Mg acceptors activated.

Finally, despite passivating the Mg acceptors and thus introducing the need to anneal samples, hydrogen can be beneficial to the production of p-type GaN. Neugebauer and Van de Walle also calculate the formation energy for nitrogen vacancies with and without the presence of hydrogen[67]. In the absence of hydrogen nitrogen vacancies are the dominant defect and significant compensation of the acceptors can occur. However, the formation energy of hydrogen is lower than the nitrogen vacancies thus in a hydrogen rich environment the formation of nitrogen vacancies is suppressed and hydrogen becomes the dominant defect. A hydrogen rich environment for growth also has the added bonus of increasing the Mg concentration incorporated during growth. This occurs because the inclusion of hydrogen pushes the Fermi-level equilibrium position higher in the bandgap, resulting in a lower formation energy for Mg and hence, according to Equation 1.34, a higher Mg concentration.

1.7 Summary

In this chapter the importance of III- nitride research has been highlighted and a brief summary of the history of semiconductor light emitters and GaN development has been given. This was followed by a description of some of the concepts behind semiconductor light emitters, such as quantum wells and quantised energy levels, the idea of a density of states, electron transition mechanisms and the transition strength. In section 1.4 the properties of III – nitrides were described, detailing the wurtzite crystal structure, the III – nitride alloy system, the cause of strain, substrate choice and buffer layers and nitride parameter values. Piezoelectric fields are considerable

within InGaN/GaN QWs grown along the [0001] directions; their cause and the method for calculating the field was described in section 1.5. Finally issues arising during doping and the role of hydrogen were discussed in section 1.6.

1.8 References

1. M. Bertolotti, *Masers and Lasers: An Historical Approach*. 1987, Bristol: Adam Hilger.

2. T. Round, *Electrical World*. 1907: p. 309.

3. J.P. Gordon, H.J. Zeiger, and C.H. Townes, *Molecular Microwave Oscillator and New Hyperfine Structure in the Microwave Spectrum of NH3*. Physical Review, 1954. **95**(1): p. 282-284.

4. Y. Watanabe and J. Nishizawa, *Semiconductor Maser*, in *Japanese Patent no. 273127*. Applied on 22nd April 1957: issued 20th September 1960.

5. N.G. Basov, B.M. Vul, and Y. Popov, Zh. Eskp. Teor. Fiz., 1959. **37**: p. 587.

6. F.H. Nicoll, *Intense recombination radiation and room-temperature lasing in CdS excited by high-voltage rf current pulses*. Applied Physics Letters, 1973. **23**(8): p. 465.

7. N.G. Basov, O.N. Krokhim, and Y. Popov, JETP, 1961. **10**: p. 1879.

8. R.N. Hall, G.E. Fenner, J.O. Kingsley, T.J. Soltys, and R.O. Carlson, *Coherent Light Emission From GaAs Junctions*. Physical Review Letters, 1962. **9**: p. 366-368.

9. N. Holonyak jr and S.F. Benacqua, Applied Physics Letters, 1962: p. 82.

10. W.P. Nathan, W.P. Dumke, G. Burns, F.H. Dill jr, and G. Lasher, Applied Physics Letters, 1962. **1**: p. 62.

11. T.M. Quist, R.H. Rediker, R.J. Keyes, W.E. Krag, B. Lax, A.L. McWhorter, and H.J. Zieger, Applied Physics Letters, 1962. **1**: p. 91.

12. H. Kroemer. in *Proc IEEE*. 1963. **51** p.1782: IEEE.

13. I. Hayashi and B. Panish, *GaAsGa$_x$Al$_{1-x}$As Heterostructure Injection Lasers which Exhibit Low Thresholds at Room Temperature*. Journal of Applied Physics, 1970. **41**(1): p. 150-163.

14. H. Grimmeiss and Z. H-Koelmans, Naturfg, 1959. **14a**: p. 264.

15. W.C. Johnson, J.B. Parsons, and M.C. Crew, *Nitrogen Compounds of Gallium. III*. Journal of Physical Chemistry, 1932. **234**: p. 2651-54.

16. R. Juza and E. Hahn, Anorg. Allgem. Chem., 1938. **234**: p. 282.

17.   H.P. Maruska and J.J. Tietjen, Applied Physics Letters, 1969. **15**: p. 367.

18.   R. Dingle, K.L. Shaklee, R.F. Leheny, and R.B. Zetterstrojm, *Stimulated Emission and Laser Action in Gallium Nitride*. Applied Physics Letters, 1971. **19**(1): p. 5-7.

19.   J.I. Pankove, E.A. Miller, and J.E. Berkeyheiser, *GaN blue light-emitting diodes*. Journal of Luminescence, 1972. **5**(1): p. 84-86.

20.   H.P. Maruska, D.A. Stevenson, and J.I. Pankove, *Violet luminescence of Mg-doped GaN*. Applied Physics Letters, 1973. **22**(6): p. 303.

21.   H. Amano, I. Akasaki, T. Kozawa, K. Hiramatsu, N. Sawaki, K. Ikeda, and Y. Ishii, *Electron-Beam Effects on Blue Luminescence of Zinc-Doped GaN*. Journal of Luminescence, 1988. **40-1**: p. 121-122.

22.   H. Amano, M. Kito, K. Hiramatsu, and I. Akasaki, *P-Type Conduction in Mg-Doped GaN Treated with Low-Energy Electron-Beam Irradiation (LEEBI)*. Japanese Journal of Applied Physics Part 2-Letters, 1989. **28**(12): p. L2112-L2114.

23.   J.A. van Vechten, J.D. Zook, R.D. Horning, and B. Goldenberg, *Defeating Compensation in Wide Gap Semiconductors by Growing in H That Is Removed by Low-Temperature De-Ionizing Radiation*. Japanese Journal of Applied Physics Part 1-Regular Papers Short Notes & Review Papers, 1992. **31**(11): p. 3662-3663.

24.   S. Nakamura, T. Mukai, M. Senoh, and N. Iwasa, *Thermal Annealing Effects on P-Type Mg-Doped GaN Films*. Japanese Journal of Applied Physics Part 2-Letters, 1992. **31**(2B): p. L139-L142.

25.   S. Nakamura, N. Iwasa, M. Senoh, and T. Mukai, *Hole Compensation Mechanism of P-Type GaN Films*. Japanese Journal of Applied Physics Part 1-Regular Papers Short Notes & Review Papers, 1992. **31**(5A): p. 1258-1266.

26.   S. Nakamura, T. Mukai, and M. Senoh, *Candela-Class High-Brightness InGaN/AlGaN Double- Heterostructure Blue-Light-Emitting Diodes*. Applied Physics Letters, 1994. **64**(13): p. 1687-1689.

27.   S. Nakamura, *First laser diodes fabricated from III-V nitride based materials*. Materials Science and Engineering B-Solid State Materials for Advanced Technology, 1997. **43**(1-3): p. 258-264.

28.   S. Nakamura, *First III-V-nitride-based violet laser diodes*. Journal of Crystal Growth, 1997. **170**(1-4): p. 11-15.

29. L.A. Coldren and S.W. Corzine, *Diode Lasers and Photonic Integrated Circuits*. 1995, New York: John Wiley & Sons, Inc.

30. M. Krijn, *Heterojunction Band Offsets and Effective Masses in III-V Quaternary Alloys*. Semiconductor Science and Technology, 1991. **6**(1): p. 27-31.

31. F.C. Frank and J.H. van de Merwe. in *Proc. R. Soc. A*. 1949. **198** p. 216.

32. E.P. O'Reilly, *Valence Band Engineering in Strained-Layer Structures*. Semiconductor Science and Technology, 1989. **4**(3): p. 121-137.

33. S.M. Bedair, *Indium-based Nitride Compounds*, in *Gallium Nitride (GaN) I*, J.I. Pankove and T.D. Moustakas, Editors. 1998, Academic: New York.

34. H.K. Cho, J.Y. Lee, J.H. Song, P.W. Yu, G.M. Yang, and C.S. Kim, *Influence of strain-induced indium clustering on characteristics of InGaN/GaN multiple quantum wells with high indium composition*. Journal of Applied Physics, 2002. **91**(3): p. 1104-1107.

35. N. Duxbury, U. Bangert, P. Dawson, E.J. Thrush, W. Van der Stricht, K. Jacobs, and I. Moerman, *Indium segregation in InGaN quantum-well structures*. Applied Physics Letters, 2000. **76**(12): p. 1600-1602.

36. L.J. Brillson, T.M. Levin, G.H. Jessen, and F.A. Ponce, *Localized states at InGaN/GaN quantum well interfaces*. Applied Physics Letters, 1999. **75**(24): p. 3835-3837.

37. S. Chichibu, T. Azuhata, T. Sota, and S. Nakamura, *Luminescences from localized states in InGaN epilayers*. Applied Physics Letters, 1997. **70**(21): p. 2822-2824.

38. Y. Narukawa, Y. Kawakami, M. Funato, S. Fujita, and S. Nakamura, *Role of self-formed InGaN quantum dots for exciton localization in the purple laser diode emitting at 420 nm*. Applied Physics Letters, 1997. **70**(8): p. 981-983.

39. S.F. Chichibu, K. Wada, J. Mullhauser, O. Brandt, K.H. Ploog, T. Mizutani, A. Setoguchi, R. Nakai, M. Sugiyama, H. Nakanishi, K. Korii, T. Deguchi, T. Sota, and S. Nakamura, *Evidence of localization effects in InGaN single-quantum-well ultraviolet light-emitting diodes*. Applied Physics Letters, 2000. **76**(13): p. 1671-1673.

40. Y.C. Yeo, T.C. Chong, M.F. Li, and W.J. Fan, *Analysis of optical gain and threshold current density of wurtzite InGaN/GaN/AlGaN quantum well lasers*. Journal of Applied Physics, 1998. **84**(4): p. 1813-1819.

41.   H. Amano, N. Sawaki, I. Akasaki, and Y. Toyoda, *Metalorganic Vapor-Phase Epitaxial-Growth of a High-Quality GaN Film Using an AlN Buffer Layer.* Applied Physics Letters, 1986. **48**(5): p. 353-355.

42.   S. Nakamura, *GaN Growth Using GaN Buffer Layer.* Japanese Journal of Applied Physics Part 2-Letters, 1991. **30**(10A): p. L1705-L1707.

43.   J.H. Song, S.J. Chua, E.A. Fitzgerald, P. Chen, and S. Tripathy, *Strain relaxation in graded InGaN/GaN epilayers grown on sapphire.* Applied Physics Letters, 2003. **83**(8): p. 1545-1547.

44.   I. Vurgaftman, J.R. Meyer, and L.R. Ram-Mohan, *Band parameters for III-V compound semiconductors and their alloys.* Journal of Applied Physics, 2001. **89**(11): p. 5815-5875.

45.   W.G. Caddy, *Piezoelectricity.* International Series in Pure and Applied Physics, ed. G.P. Harnwell. 1946, York: McGraw-Hill.

46.   T. Matsuoka, H. Okamoto, M. Nakao, H. Harima, and E. Kurimoto, *Optical bandgap energy of wurtzite InN.* Applied Physics Letters, 2002. **81**(7): p. 1246-1248.

47.   P. Perlin, L. Mattos, N.A. Shapiro, J. Kruger, W.S. Wong, T. Sands, N.W. Cheung, and E.R. Weber, *Reduction of the energy gap pressure coefficient of GaN due to the constraining presence of the sapphire substrate.* Journal of Applied Physics, 1999. **85**(4): p. 2385-2389.

48.   M. Suzuki, T. Uenoyama, and A. Yanase, *First-principles calculations of effective-mass parameters of AlN and GaN.* Physical Review B, 1995. **52**(11): p. 8132-8139.

49.   P. Kiesel, F. Renner, M. Kneissel, N.M. Johnson, and G.H. Dohler, *Electroabsorption Spectroscopy - Direct Determination of the strong Piezoelectric Field in InGaN/GaN Heterostructure Diodes.* Physica Status Solidi a-Applied Research, 2001. **188**(1): p. 131-134.

50.   Y.D. Jho, J.S. Yahng, E. Oh, and D.S. Kim, *Measurement of piezoelectric field and tunneling times in strongly biased InGaN/GaN quantum wells.* Applied Physics Letters, 2001. **79**(8): p. 1130-1132.

51.   G. Vaschenko, D. Patel, C.S. Menoni, N.F. Gardner, J. Sun, W. Gotz, C.N. Tome, and B. Clausen, *Significant strain dependence of piezoelectric constants in In_xGa_{1-x}/GaN quantum wells.* Physical Review B, 2001. **64**(24): p. 241308(R).

52. G. Vaschenko, D. Patel, C.S. Menoni, S. Keller, U.K. Mishra, and S.P. DenBaars, *Dominant role of the piezoelectric field in the pressure behavior of InGaN/GaN quantum wells.* Applied Physics Letters, 2001. **78**(5): p. 640-642.

53. T. Takeuchi, C. Wetzel, S. Yamaguchi, H. Sakai, H. Amano, I. Akasaki, Y. Kaneko, S. Nakagawa, Y. Yamaoka, and N. Yamada, *Determination of piezoelectric fields in strained GaInN quantum wells using the quantum-confined Stark effect.* Applied Physics Letters, 1998. **73**(12): p. 1691-1693.

54. B.K. Laurich, K. Elcess, C.G. Fonstad, J.G. Beery, C. Mailhiot, and D.L. Smith, *Optical-Properties of (100) Oriented and (111) Oriented GaInAs/GaAs Strained-Layer Superlattices.* Physical Review Letters, 1989. **62**(6): p. 649-652.

55. C. Mailhiot and D.L. Smith, *Electronic-Structure of 001 -Growth-Axis and 111 -Growth-Axis Semiconductor Superlattices.* Physical Review B, 1987. **35**(3): p. 1242-1259.

56. W.A. Harrison, *Electronic Structure and the Properties of Solids.* 1980, San Francisco: W. H. Freeman.

57. A. Bykhovski, B. Gelmont, and M. Shur, *The Influence of the Strain-Induced Electric-Field on the Charge-Distribution in GaN-AlN-GaN Structure.* Journal of Applied Physics, 1993. **74**(11): p. 6734-6739.

58. T. Takeuchi, S. Sota, M. Katsuragawa, M. Komori, H. Takeuchi, H. Amano, and I. Akasaki, *Quantum-confined stark effect due to piezoelectric fields in GaInN strained quantum wells.* Japanese Journal of Applied Physics Part 2-Letters, 1997. **36**(4A): p. L382-L385.

59. I.L. Guy, S. Muensit, and E.M. Goldys, *Extensional piezoelectric coefficients of gallium nitride and aluminum nitride.* Applied Physics Letters, 1999. **75**(26): p. 4133-4135.

60. H. Morkoc, *Nitride Semiconductors and Devices.* 1999, Berlin: Springer.

61. W. Gotz and N.M. Johnson, *Characterization of Dopants and Deep Level Defects,* in *Gallium Nitride (GaN) II,* J.I. Pankove and T.D. Moustakas, Editors. 1998, Academic: New York.

62. W. Gotz, N.M. Johnson, J. Walker, D.P. Bour, H. Amano, and I. Akasaki, *Hydrogen Passivation of Mg Accepteos in GaN Grown by Metalorganic Chemical-Vapor-Deposition.* Applied Physics Letters, 1995. **67**(18): p. 2666-2668.

63.   W. Gotz, N.M. Johnson, J. Walker, D.P. Bour, and R.A. Street, *Activation of acceptors in Mg-doped GaN grown by metalorganic chemical vapor deposition.* Applied Physics Letters, 1996. **68**(5): p. 667-669.

64.   S.H. Wei and A. Zunger, *Role of Metal D-States in II-VI Semiconductors.* Physical Review B, 1988. **37**(15): p. 8958-8981.

65.   C.G. Van de Walle and N.M. Johnson, *Hydrogen in III-V Nitrides*, in *Gallium Nitride (GaN) II*, J.I. Pankove and T.D. Moustakas, Editors. 1998, Academic: New York.

66.   J. Neugebauer and C.G. van de Walle, *Hydrogen in GaN - Novel Aspects of a Common Impurity.* Physical Review Letters, 1995. **75**(24): p. 4452-4455.

67.   J. Neugebauer and C.G. van de Walle. in *Material Research Society Symposium.* 1996. Pittsburgh: Material Research Society.

68.   S. Nakamura, S. Pearton, and G. Fasol, *The Blue Laser Diode: the complete story.* 2nd ed. 2000, Berlin: Springer.

2 Photocurrent Absorption

2.1 Introduction

The internal piezoelectric field in GaN based QWs plays an important role in device performance, affecting the emission wavelength, recombination lifetime and transition strength, thus an accurate knowledge of the strength of the piezoelectric field is vital when trying to understand the properties of GaN based devices. Despite the importance of the piezoelectric field, a consensus over the piezoelectric constants has still to be reached and large differences are reported between theoretical calculations and experimental results[1]. Hence reverse bias photocurrent absorption will be used to determine the piezoelectric field within a set of InGaN QW devices and a comparison will be made with the calculated value, where the piezoelectric constants have been interpolated from the binary values of InN and GaN.

The wafers were grown at the Xerox, Palo Alto Research Centre in California and were fabricated into light emitting devices at Cardiff University by Mark Dineen[2]. They consist of a 4μm n-GaN buffer layer grown on (0001) plane sapphire, followed by a 50nm n-doped $In_{0.02}Ga_{0.98}N$ defect reduction layer. Either side of the active region, waveguiding is provided by 100nm GaN and 0.5μm $Al_{0.07}Ga_{0.93}N$, n and p-doped appropriately. The active region itself consists of five 3.5nm $In_{0.1}Ga_{0.9}N$ QWs embedded between 6.5nm $In_{0.01}Ga_{0.99}N$ barriers. Immediately after the active region, on the p-side of the device a 20nm $Al_{0.2}Ga_{0.8}N$ barrier was employed to help with electron confinement, and the device was capped with 100nm of p-GaN. The composition and thickness of the active region was determined by X-ray diffraction. The donor and acceptor concentrations in the n and p-type regions were $N_D = 2 - 5 \times 10^{18} cm^{-3}$ and $N_A = 10^{20} cm^{-3}$, respectively. A schematic representation of the fabricated device is given in Figure 2.1 below.

Cr/Au (20/300nm)

50 µm

300 µm

0.6 µm Silicon Dioxide

100nm p-type GaN

500nm p-type AlGaN

100nm p-type GaN

20nm p-type AlGaN

5x [35A InGaN QW (10%)
    65A InGaN Barrier (1%)]

100nm n-type GaN

500nm n-type AlGaN

50nm n-type InGaN (2%)

4 µm n-type GaN

Sapphire Substrate

2.6 µm
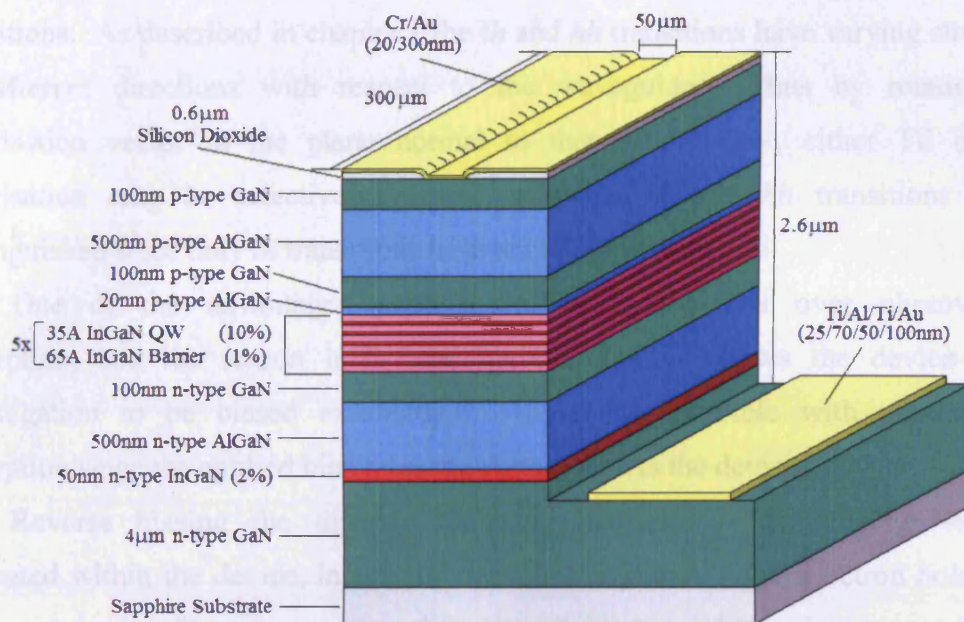
Ti/Al/Ti/Au (25/70/50/100nm)

Figure 2.1 – Schematic diagram of the device structure.

2.2   Experimental Techniques

In this section the principles behind photocurrent absorption along with the apparatus used in the experiments will be explained.

2.2.1   Experimental Principles

Photocurrent absorption is very similar in nature to photovoltage absorption and either may be performed using the experimental set up described in section 2.2.2. The principle behind both photocurrent and photovoltage absorption is as follows. Electron-hole pairs are generated within a material when the photon energy of incident light is greater than the bandgap of that material. These newly generated electron hole pairs are subsequently separated by the internal *p-i-n* field within the device. As their names suggest, photovoltage absorption is a measure of the voltage generated whereas photocurrent absorption is a measure of the generated current. By using a lamp and monochromator to vary the photon energy of the incident light a spectrum can be generated, where the changes in intensity correspond to the bandgap or energy levels of the constituent materials.

Unless specifically stated all absorption measurements will be preformed with the light incident on the edge of the device, as described by Smowton et al. [3]. This configuration has the advantage of allowing measurements to be performed on actual devices, as well as distinguishing both light and heavy hole (*lh* and *hh* respectively)

transitions. As described in chapter 1 the *lh* and *hh* transitions have varying strengths in different directions with respect to the waveguide. Thus by rotating the polarisation vector in the plane normal to that of the QW, either TE or TM polarisation may be selectively excited, allowing *lh* and *hh* transitions to be distinguished since only *lh* transitions have a TM component.

One of the advantages photocurrent absorption has over photovoltage absorption, and the reason it is used here, is that it allows the device under investigation to be biased externally. This is not possible with photovoltage absorption since the applied bias fixes the voltage across the device.

Reverse biasing the device effectively increases the internal *p-i-n* field generated within the device, increasing the efficiency with which electron hole pairs are swept away. Therefore one would expect the measured signal corresponding to the absorption intensity to increase with increasing reverse bias until a peak is reached when all the generated carriers are swept out. This situation is made slightly more complicated in InGaN/GaN QW structures due to the presence of large internal piezoelectric fields within the QWs, which oppose any externally applied reverse bias due to the quantum confined Stark effect. This is discussed in greater detail later on in section 2.3.
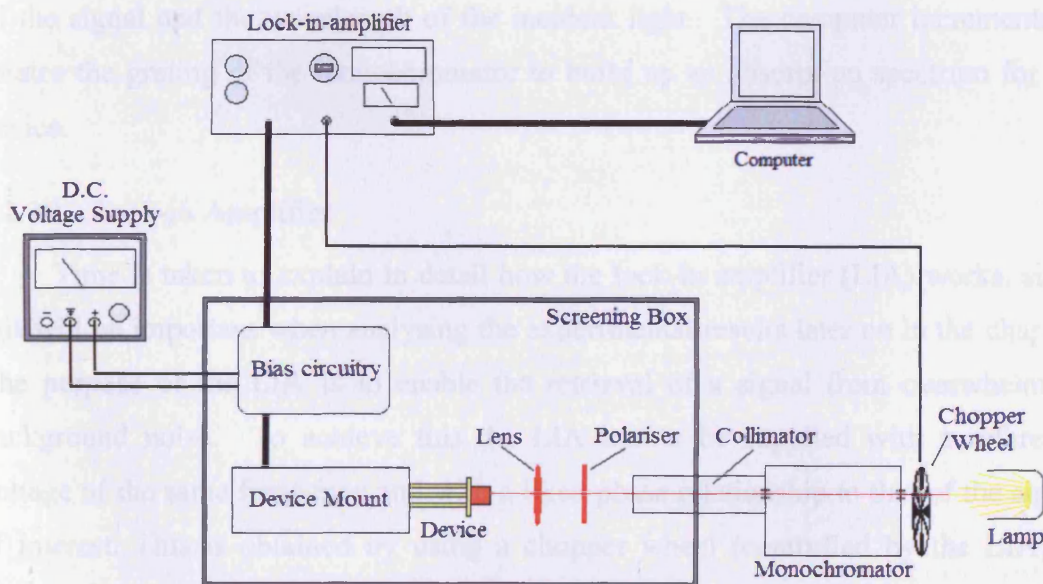
2.2.2 Experimental Set-up

Figure 2.2 – Schematic diagram of experimental set-up used in photocurrent experiments.

The experimental set-up used for the photocurrent absorption measurements is shown in Figure 2.2 and discussed below. The monochromatic light used in the experiment is generated by passing light from a white light source (a halogen bulb) through a monochromator. On leaving the monochromator, the monochromatic light passes through a collimator before being focused onto the end facet of the device. The device is mounted on a translation stage which allows movement along all three Cartesian coordinates as well as rotation about all three axes, thus allowing the waveguide of the device to be aligned directly with the incident light. To reduce noise the device is encased in a metal box, which shields the device from both electrical signals and background light.

The photo-induced signal from the device is sent to a lock-in amplifier (LIA) via the bias circuitry, which allows an external DC bias to be applied to the device. The LIA contains a built in current amplifier, which amplifies the current signal from the device and converts it to a voltage signal which can be read by LIA. It is the use of the current amplifier that enables photocurrent absorption measurements to be carried out, connecting the signal from the device directly to the LIA results in photovoltage absorption being measured (It is important to note that the device cannot be externally biased in photovoltage absorption experiments, for reasons discussed earlier.). The LIA is discussed in greater detail in section 2.2.2.1.

The signal from the LIA is then sent to a computer, which records the intensity of the signal and the wavelength of the incident light. The computer incrementally rotates the grating of the monochromator to build up an absorption spectrum for the device.

2.2.2.1 Lock-in Amplifier

Time is taken to explain in detail how the lock-in amplifier (LIA) works, since this will be important when analysing the experimental results later on in the chapter. The purpose of the LIA is to enable the retrieval of a signal from overwhelming background noise. To achieve this the LIA has to be supplied with a reference voltage of the same frequency and with a fixed phase relationship to that of the signal of interest. This is obtained by using a chopper wheel (controlled by the LIA) to modulate the light incident on the facet of the device at the same frequency as the LIA reference voltage, locking the input signal to the reference signal. Since there is no

frequency drift extremely small bandwidths can be defined, improving the signal to noise ratio.

At the heart of the LIA is a phase-sensitive detector (also known as a demodulator or mixer), which multiplies the input signal with the LIA reference signal, see Figure 2.3.

As an example, the case where the input to the LIA is a noise-free sine wave is considered. The LIA generates an internal sinusoidal reference signal which the demodulator multiplies with the input signal as shown in Figure 2.3. The output from the demodulator is a sinusoid with twice the frequency (2ω) of the reference signal. If there is no phase difference between the input and reference signals the mean or average value is positive as shown in Figure 2.3a, a low pass filter is used to remove 2ω component. However if the input signal lags the reference signal by $90°$ then the mean average value of the demodulator output will be zero as shown in Figure 2.3b. Thus by keeping the amplitude of the reference signal constant and adjusting its phase to match the input signal the amplitude of the input signal may be determined from the average value of the demodulator output.

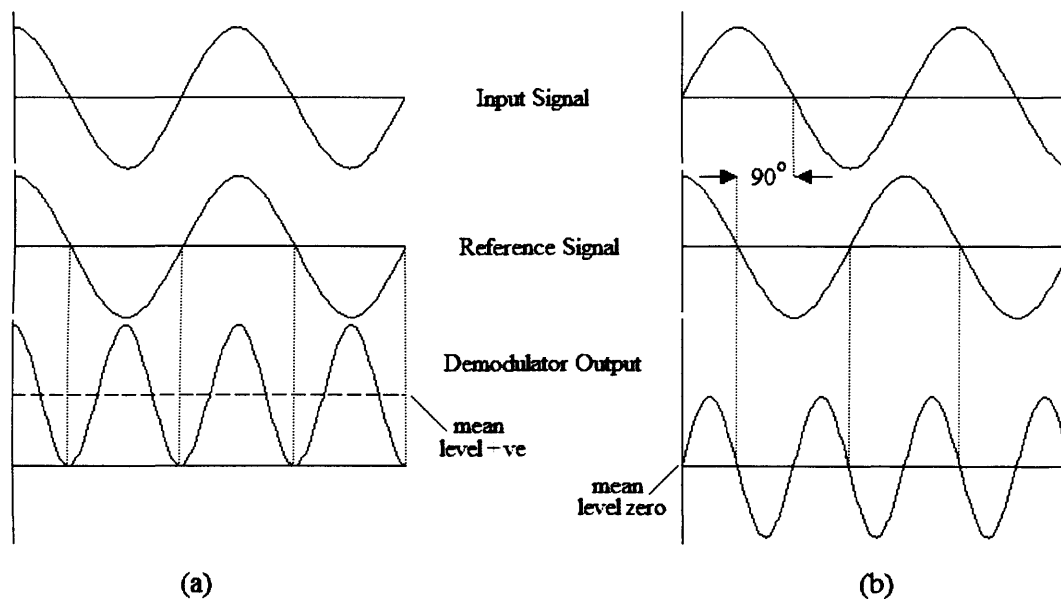(a)   (b)

Figure 2.3 – Example of the demodulator output a) when the input and output signals are in phase and b) when the input signal lags the reference signal by 90°.

This technique enables the retrieval of a signal from overwhelming background noise since, by definition, noise has no fixed frequency or phase relationship to the reference signal and thus does not contribute to the average DC level of the

demodulator output. Noise components at frequencies very close to that of the reference signal will result in demodulator outputs with very low frequencies, however these may be rejected using a high-pass filter with a sufficiently low cut-off.

2.3 Measuring the Piezoelectric Field

As discussed in chapter 1, due to the lattice mismatch between InN and GaN there are large internal piezoelectric fields present within InGaN/GaN QWs. In this section the internal piezoelectric fields will be determined using reverse bias techniques, the principles of which are discussed in section 2.3.1 and the experimental results are presented in section 2.3.2.

2.3.1 Experimental Principles

The internal piezoelectric field skews the QW, breaking its symmetry and causing spatial separation of the electron and hole wavefunctions and a decrease in the ground state transition energy, due to the quantum confined Stark effect, see Figure 2.4a.

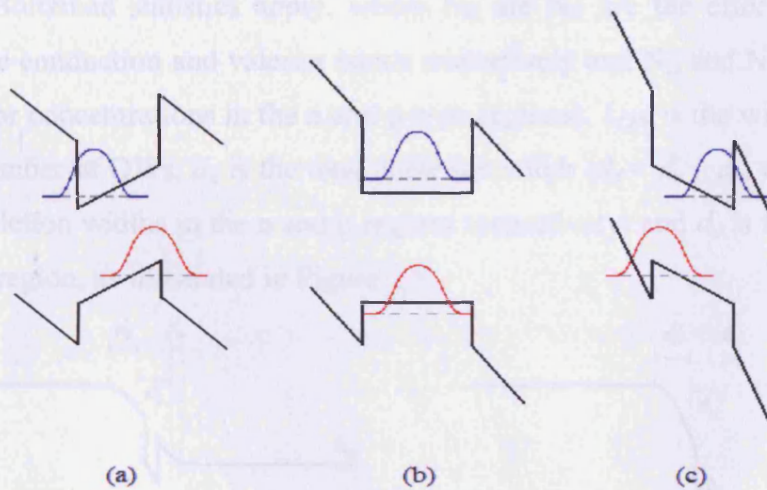(a)   (b)   (c)

Figure 2.4 – Schematic potential energy band diagram of an InGaN/GaN QW a) zero bias, b) when the applied reverse bias balances the piezoelectric field squaring the QW and c) under a large reverse bias skewing the QW in the opposite direction.

Applying a reverse bias to the device counteracts the piezoelectric field and, at a critical value, the reverse bias will equal the piezoelectric field. At this point the QW is square and the electron and hole wavefunction overlap and the ground state transition energy is maximised, as shown in Figure 2.4b. Further increases in reverse bias result in the QW being skewed in the opposite direction, once again reducing the overlap of the electron and hole wavefunctions and reducing the ground state

transition energy, as shown in Figure 2.4c. Therefore by observing the absorption spectrum as the reverse bias is increased one should see the absorption intensity increase, reach a maximum value then decrease. Similarly the wavelength corresponding to the peak absorption from the QW should decrease reach a minimum value and then increase again as the reverse bias is increased. Both techniques are used to determine the value of reverse bias need to square the QW.

Once the reverse bias needed to square up the QW has been determined the internal piezoelectric may be calculated using[4]:

$$E_{tot} = E_{pz} + \frac{\Delta\phi_0 - V - L_{QW} E_{pz} N}{d_u + \frac{1}{2} d_d}$$

<div align="right">**Equation 2.1**</div>

where E_{tot} is the total internal field in the QW ($E_{tot} = 0$ when the QW is square), E_{pz} is the internal piezoelectric field, V is the applied bias and is assumed to be negative for a reverse bias, $\Delta\phi_0$ is the built-in potential ($e\Delta\phi_0 = E_g + k_BT\ln(N_DN_A/N_CN_V)$ assuming Boltzman statistics apply, where N_C are N_V are the effective density of states in the conduction and valence bands respectively and N_D and N_A are the donor and acceptor concentrations in the n and p-type regions), L_{QW} is the width of the QW, N is the number of QWs, d_d is the total depletion width ($d_d = d_n + d_p$, where d_n and d_p are the depletion widths in the n and p regions respectively) and d_u is the width of the undoped i-region, as illustrated in Figure 2.5.
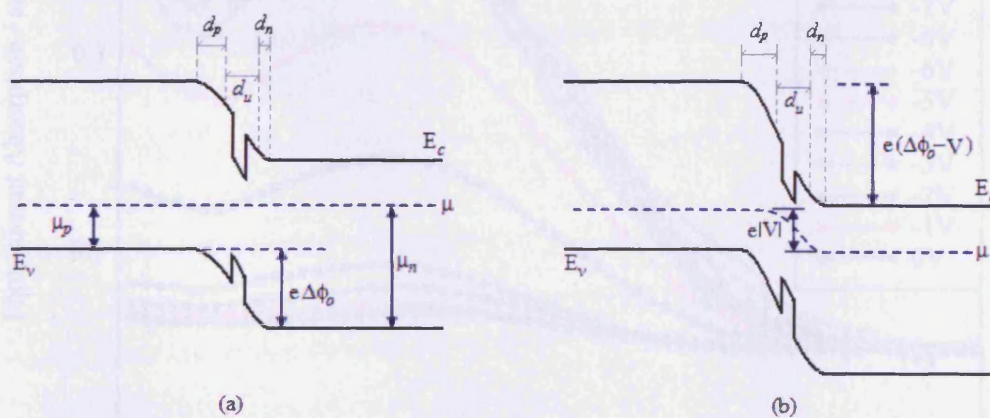

Figure 2.5 – Example of a p-i-n junction a) under zero bias and b) under reverse bias. μ is the Fermi level, μ_p is the hole quasi Fermi level, μ_n is the electron quasi Fermi level $\Delta\phi_o$ is the built in potential e is the electronic charge, d_n and d_p are the depletion widths of the n and p regions respectively, d_u is the width of the undoped region and V is the applied bias, V is assumed to be negative for a reverse bias. For simplicity the piezoelectric field has not been included.

2.3.2 Results

The experimental set-up described in section 2.2.2 was used to measure the photocurrent absorption spectra, of the devices described in the introduction, for a range of externally applied reverse bias. A polariser was used to allow the selection of either TE or TM polarisation light, the results are presented below in Figure 2.6 through to Figure 2.11.

2.3.2.1 TE Photocurrent Absorption

Using a polariser it is possible to excite only the TE transitions within the device. Both *hh* and *lh* transitions have TE components and the corresponding TE photocurrent absorption spectra are presented below.

Figure 2.6 shows the TE photocurrent absorption spectra over a range of external bias from 0 to −11V. Although the individual transition levels cannot be distinguished the movement of the general QW emission peak (around 380nm) can be tracked. As the reverse bias increases, the absorption intensity increases up to a value of around −8V at which point further increases in reverse bias result in a decrease in the absorption intensity. The change in intensity is accompanied by a shift in the peak wavelength.
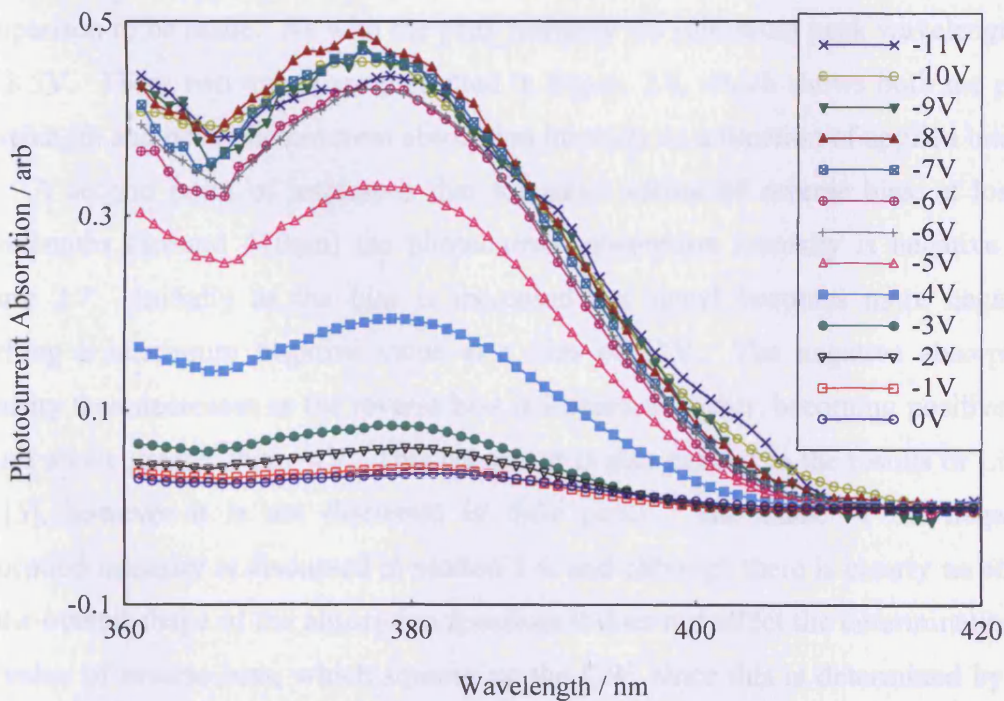

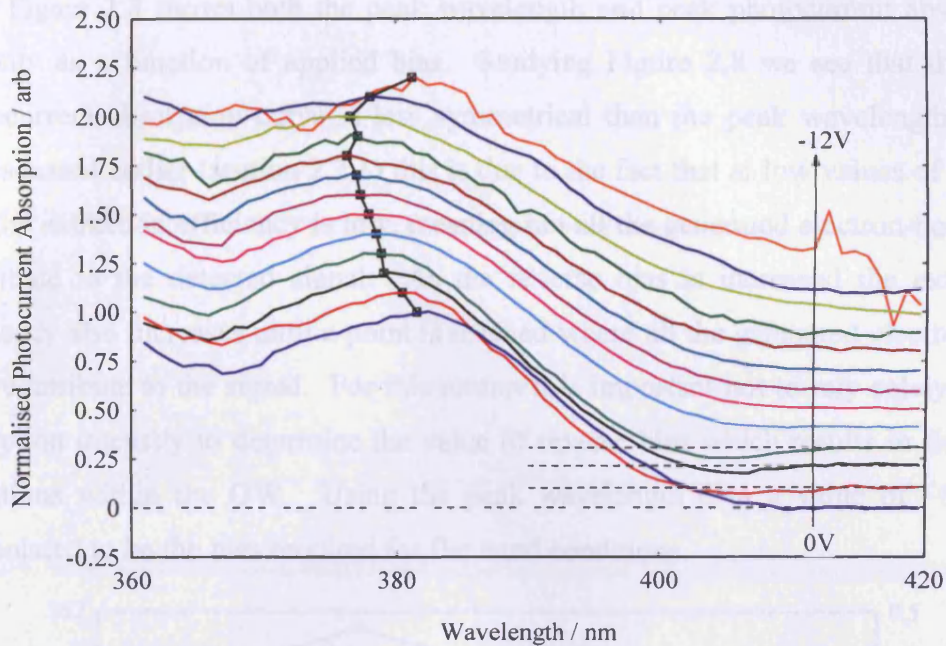**Figure 2.6 – TE photocurrent absorption spectra for a range of external biases ranging from 0 to −11V.**

Figure 2.7 – TE photocurrent absorption spectra for a range of external biases ranging from 0 to –11V. Each spectrum has been normalised at the wavelength of the peak absorption and then offset by 0.1 to allow the shift in peak wavelength to be seen more clearly. Dashed lines indicate zero level.

To see the wavelength shift the spectra have been normalised according to the intensity of the absorption peak and offset, along the *y*-axis, to afford a clearer comparison to be made. As with the peak intensity the minimum peak wavelength is at –8.5V. These two trends are presented in Figure 2.8, which shows both the peak wavelength and peak photocurrent absorption intensity as a function of applied bias.

A second point of interest is that for small values of reverse bias, at longer wavelengths (around 410nm) the photocurrent absorption intensity is negative see Figure 2.7. Initially as the bias is increased the signal becomes more negative reaching a maximum negative value at a bias of –3V. The negative absorption intensity then decreases as the reverse bias is increased further, becoming positive for values above greater than –4V. This behaviour is also evident in the results of Liu et al. [5], however it is not discussed in their paper. The cause of the negative absorption intensity is discussed in section 2.4, and although there is clearly an effect on the overall shape of the absorption spectrum it does not affect the determination of the value of reverse bias, which squares up the QW, since this is determined by the overall shift in the absorption spectra and not by its specific shape.

Figure 2.8 shows both the peak wavelength and peak photocurrent absorption intensity as a function of applied bias. Studying Figure 2.8 we see that the peak photocurrent absorption curve is less symmetrical than the peak wavelength curve. As discussed earlier (section 2.2.1) this is due to the fact that at low values of reverse bias the extraction efficiency is low, meaning not all the generated electron-hole pairs contribute to the detected signal. As the reverse bias is increased the extraction efficiency also increases until a point is reached where all the generated electron-hole pairs contribute to the signal. For this reason it is important not to rely solely on the absorption intensity to determine the value of reverse bias which results in flat band conditions within the QW. Using the peak wavelength data a value of –8.5V is interpolated to be the bias required for flat band conditions.

Figure 2.8 – Shift in the peak wavelength (blue circles) and peak photocurrent absorption intensity (black triangles) as a function of applied bias.

2.3.2.2   TM Photocurrent Absorption

Rotating the polariser used in section 2.3.2.1 by 90° allows the *lh* TM transition to be selectively excited. The experimental TM data is presented in the same manner as in section 2.3.2.1 in Figure 2.9 through to Figure 2.11 and the same analysis applies.
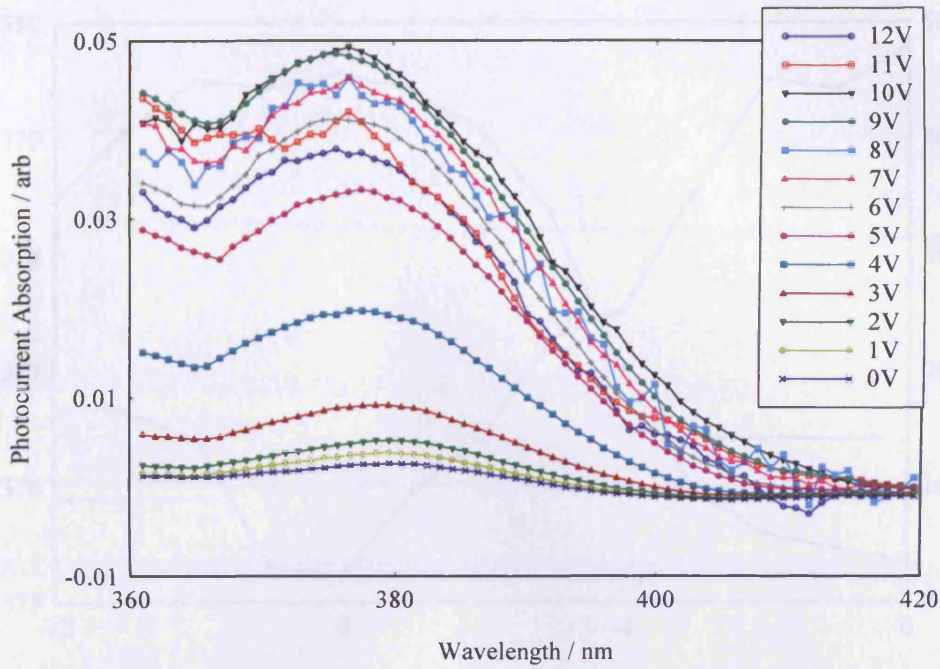
Figure 2.9 – TM photocurrent absorption spectra for a range of external biases ranging from 0 to –12V.

Figure 2.10 – TM photocurrent absorption spectra for a range of external biases ranging from 0 to –12V. Each spectrum has been normalised at the wavelength of the peak absorption and then offset by 0.1 to allow the shift in peak wavelength to be seen more clearly. Dashed lines indicate zero. The negative absorption follows the same trends as described earlier.
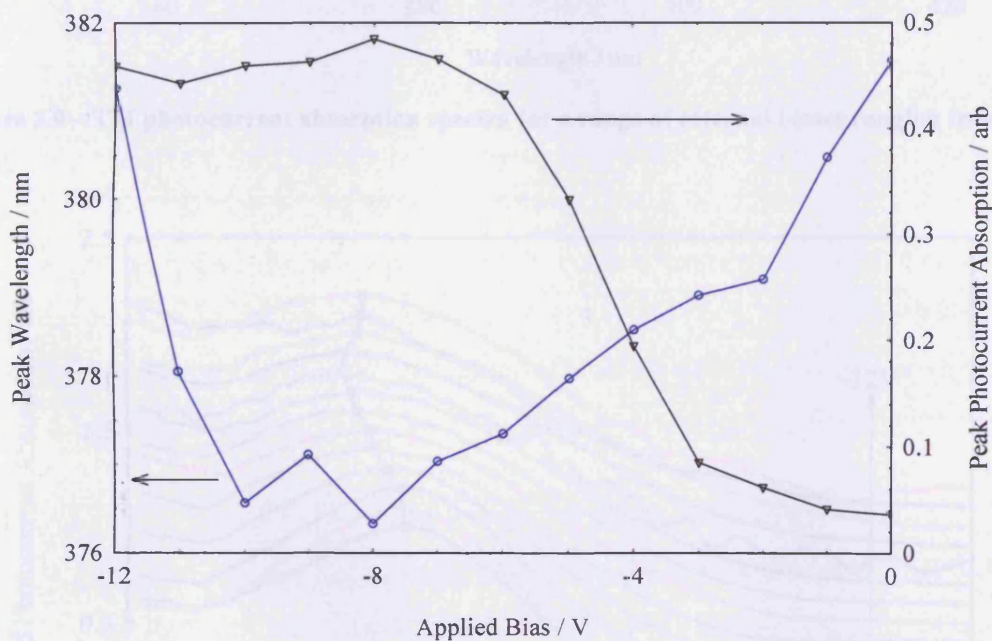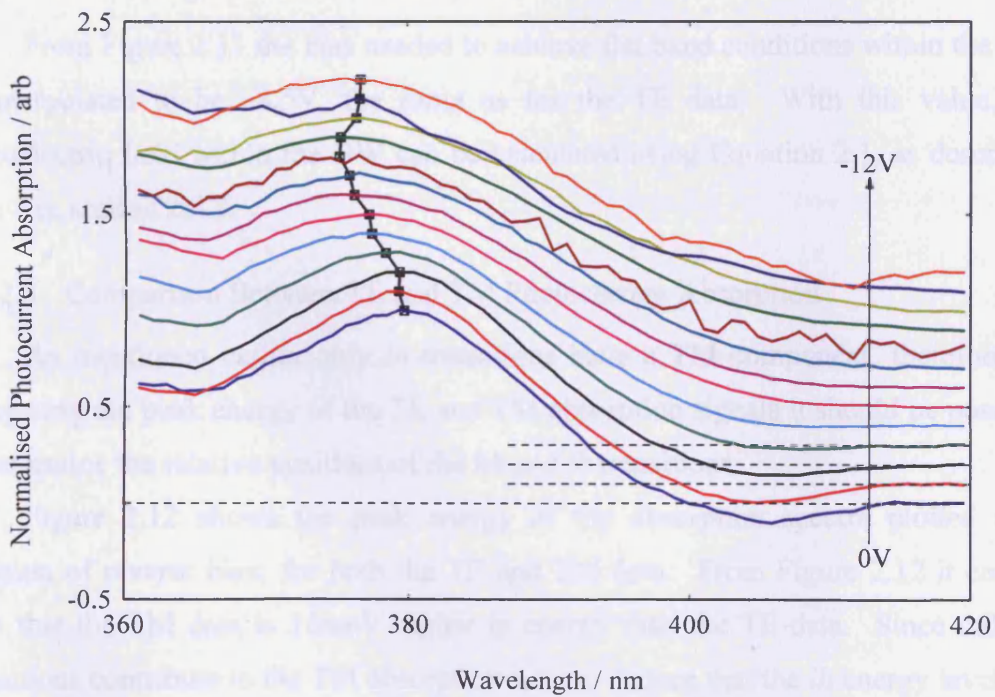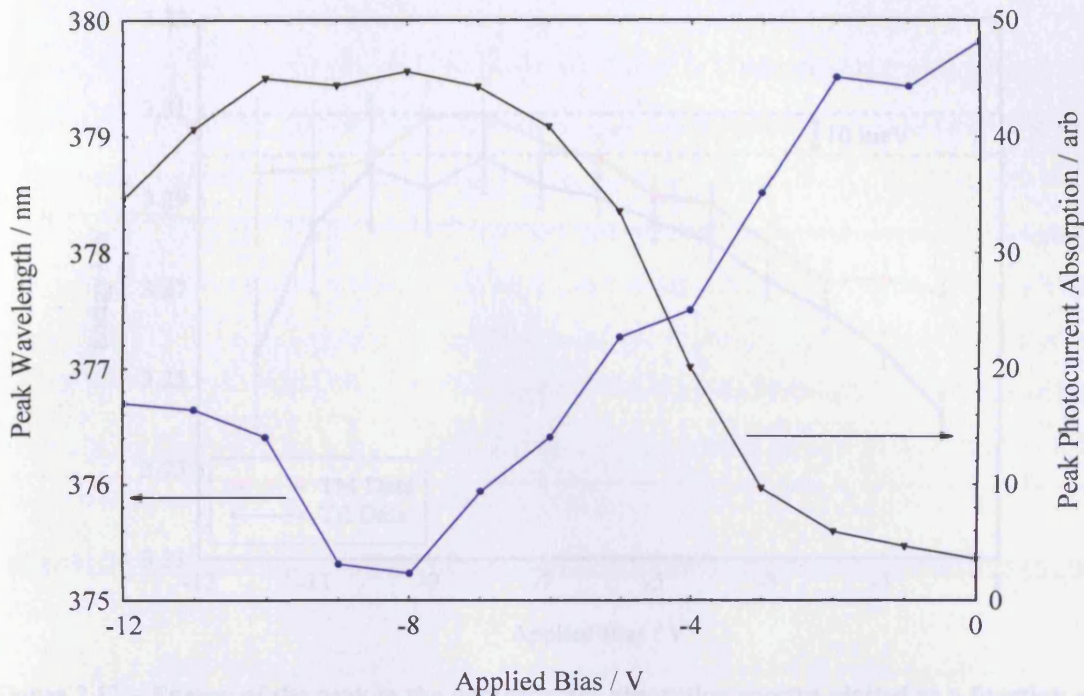
47

Figure 2.11 – Shift in the peak wavelength (blue circles) and peak photocurrent absorption intensity (black triangles) as a function of applied bias.

From Figure 2.11 the bias needed to achieve flat band conditions within the QW is interpolated to be –8.5V, the same as for the TE data. With this value, the piezoelectric field within the QW can be calculated using Equation 2.1, as described below in section 2.3.3.

2.3.2.3   Comparison Between TE and TM Photocurrent Absorption

As mentioned earlier only *lh* transitions have a TM component, therefore by comparing the peak energy of the TE and TM absorption signals it should be possible to determine the relative positions of the *hh* and *lh* transitions.

Figure 2.12 shows the peak energy of the absorption spectra plotted as a function of reverse bias, for both the TE and TM data. From Figure 2.12 it can be seen that the TM data is 10meV higher in energy than the TE data. Since only *lh* transitions contribute to the TM absorption we can deduce that the *lh* energy level sits approximately 10meV higher in the valence band than the *hh* energy level. This ties in well with the calculations of Yeo et al[6] who predicts the *hh* transition to be approximately 10meV below the *lh* transition for a 25Å $In_{0.1}Ga_{0.9}N$/GaN QW, see chapter 1, section **1.4.3**, and is generally what is expected for a compressively strained QW.
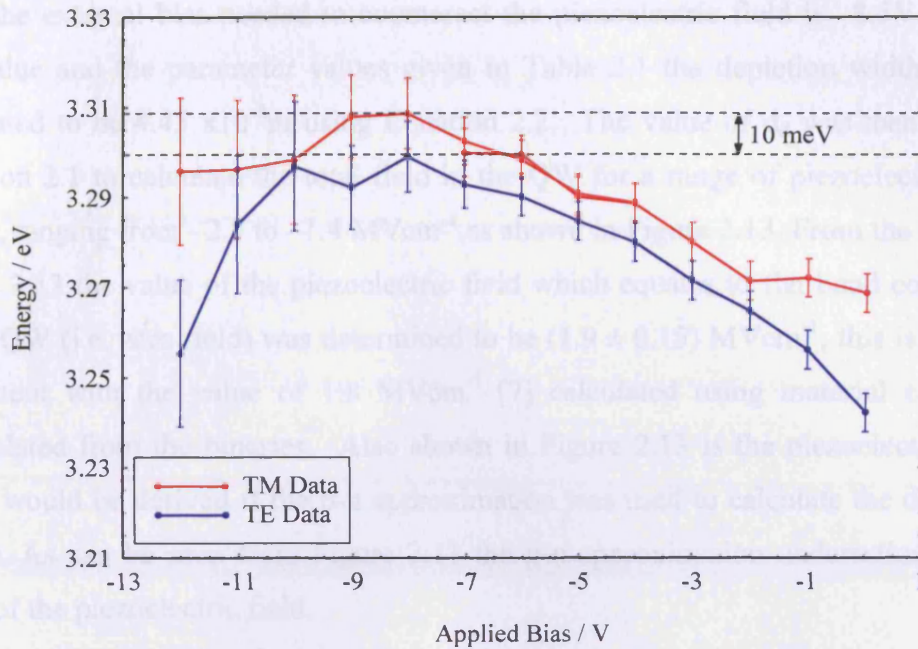
Figure 2.12 – Energy of the peak in the photocurrent absorption spectra plotted as a function of bias for the TE and TM data, blue and red curves respectively.

2.3.3   Calculating the Piezoelectric Field

Similar experiments in the literature typically report values for the piezoelectric field which are around a factor of two smaller than the value calculated using Equation 1.33 if the piezoelectric and elastic constants are interpolated from binary values[1]. We believe[7] that this inconsistency arises due to the use of the incorrect assumption that the depletion width (d_d in Equation 2.1) can be approximated using an abrupt *p-n* junction, which assumes there is no field across the intrinsic region. However there is a constant, non zero, field across this region which needs to be taken into account, and a suitable approximation for the depletion width which is valid for a p-*i*-n junction may be written as

$$d_d = -d_u + \sqrt{d_u^2 + 2\left(\frac{N_D + N_A}{N_A N_D}\right)\frac{(\Delta\phi_0 - V)\varepsilon\varepsilon_0}{e}}$$

Equation 2.2

where, N_D and N_A are the donor and acceptor doping densities respectively.

As mentioned earlier, applying a reverse bias to the device counteracts the piezoelectric field and, at a critical value, the reverse bias will equal the internal fields and the total field in the QW will be zero. From the experimental results of section

2.3.2 the external bias needed to counteract the piezoelectric field is –8.5V. Using this value and the parameter values given in Table 2.1 the depletion width d_d was calculated to be 4.45 x10⁻⁸m using Equation 2.2. The value of d_d was then used in Equation 2.1 to calculate the total field in the QW for a range of piezoelectric field values, ranging from –2.3 to –1.4 MVcm⁻¹ as shown in Figure 2.13. From the graph in Figure 2.13 the value of the piezoelectric field which equates to flat band conditions in the QW (i.e. zero field) was determined to be (1.9 ± 0.15) MVcm⁻¹, this is in good agreement with the value of 1.8 MVcm⁻¹ [7] calculated using material constants interpolated from the binaries. Also shown in Figure 2.13 is the piezoelectric field which would be derived if the p-n approximation was used to calculate the depletion width. As can be seen from Figure 2.13 the p-n approximation underestimates the value of the piezoelectric field.
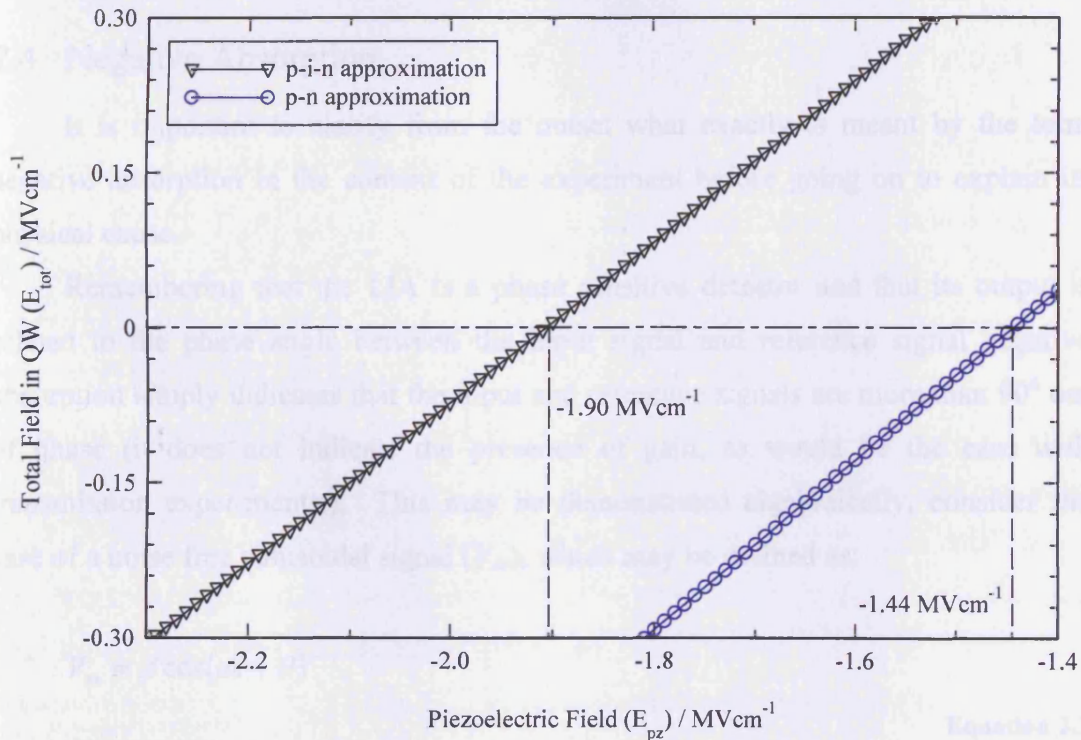

Figure 2.13 – Calculated field in QW (Etot) as a function of piezoelectric field (Epz) using the p-I-n approximation (black triangles) and p-n approximation (blue circles).

Parameter	Symbol	Value	Units
QW width	LQW	3.5x10-9	m
Barrier width	LB	6.5x10-9	m
Number of QWs	N	5	
Donor density (n-type)	ND	2x1024	m-3
Acceptor density (p-type)	NA	1x1026	m-3
Dielectric constant (Semiconductor)	ε	10.7	
Dielectric constant	εo	8.85x10-12	Fm-1
Electronic charge	ε	1.602x10-19	C
Built in potential	$\Delta\phi 0$	3.2	V
Width of i-region	d_u	5.79x10-8	m

Table 2.1 – Parameter values used to determine the piezoelectric field. The donor and acceptor densities are the measured values.

2.4 Negative Absorption

It is important to clarify from the outset what exactly is meant by the term negative absorption in the context of the experiment before going on to explain its physical cause.

Remembering that the LIA is a phase sensitive detector and that its output is related to the phase angle between the input signal and reference signal negative absorption simply indicates that the input and reference signals are more than 90° out of phase (it does not indicate the presence of gain, as would be the case with transmission experiments.). This may be demonstrated algebraically, consider the case of a noise free sinusoidal signal (V_{in}), which may be defined as:

$$V_{in} = A\cos(\omega t + \theta)$$

Equation 2.3

where, ω is the angular frequency ($\omega = 2\pi F$ where F is frequency), A is the amplitude and θ is the phase difference between the input and reference signal. The reference signal (V_{ref}) is generated internally with the same frequency F as the input signal and is defined as:

$$V_{ref} = B\cos(\omega t)$$

Equation 2.4

The phase sensitive detector multiplies these two signals together returning a voltage given by

$$V_{psd} = A\cos(\omega t + \theta) \cdot B\cos(\omega t)$$

Equation 2.5

Using appropriate trigonometric relations this may be written as

$$V_{psd} = \tfrac{1}{2} AB\cos\theta + \tfrac{1}{2} AB\cos(2\omega t + \theta)$$

Equation 2.6

In order to convert the output of the LIA to a DC signal V_{psd} then passes through a low-pass filter, which removes the $2\omega t$ component. With this in mind it can be seen, from Equation 2.6, that if the input and reference signal are in phase ($\theta = 0$) the DC output from the phase sensitive detector will be positive. However, if θ is greater than 90° the DC output will be negative.

When photocurrent absorption spectra were recorded the phase difference between the input and reference signal was adjusted to zero at a wavelength of 360nm, which corresponds to absorption by the GaN layers. The two signals were said to be in-phase when the absorption signal was maximised. Phase alignment was carried out at this wavelength since it is assumed the GaN layers are unstrained and thus do not contain piezoelectric fields. Therefore the absorption efficiency should not change with external bias, as would be the case for absorption in the QW. The negative absorption signal, at ~410nm in Figure 2.7 and Figure 2.10, thus implies that the absorption signal from the QW is out of phase with the absorption signal from the GaN layers (and hence the reference signal) by more than 90°. This phase shift can clearly be seen in Figure 2.14, which shows the measured phase difference between the input photocurrent absorption signal and the LIA reference signal with zero external bias.
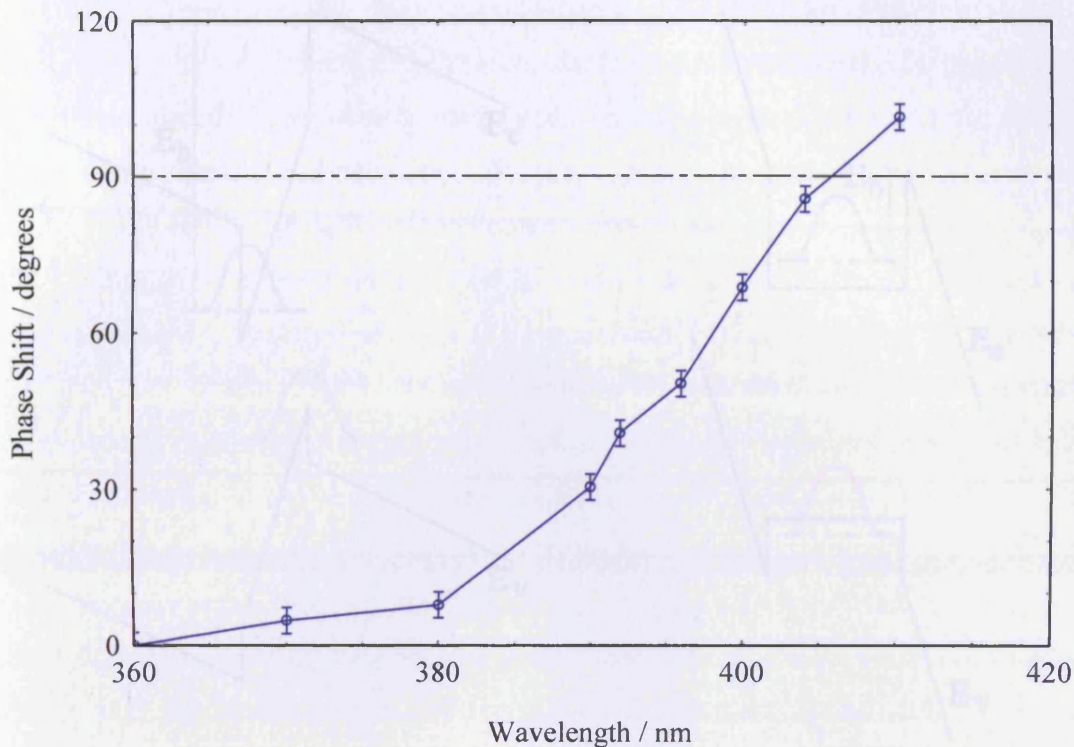
Figure 2.14 – Measured phase difference between the input photocurrent absorption signal and the internal reference signal of the LIA at zero bias.

The cause of the phase shift is believed to be due to the quantum confined Stark effect as a result of the large piezoelectric field. Under zero bias (i.e. thermal equilibrium) the electron and hole wavefunctions drop into triangular potential wells. These are formed on opposite sides of the QW and thus result in a reduced electron hole wavefunction overlap. Also due to the large piezoelectric field the barrier the electrons have to overcome in order to be extracted from the device is very large (see Figure 2.15a). Consequently the electron hole pairs cannot be extracted as soon as they are generated resulting is a time delay while sufficient charge builds up to allow the electrons to be extracted.

As increasing reverse bias is applied to the device the apparent barrier height and thickness is reduced (see Figure 2.15b). The reverse bias also strengthens the field responsible for extracting the electrons. Consequently less charge needs to build up before the electrons can be extracted resulting in a reduction in the phase shift.
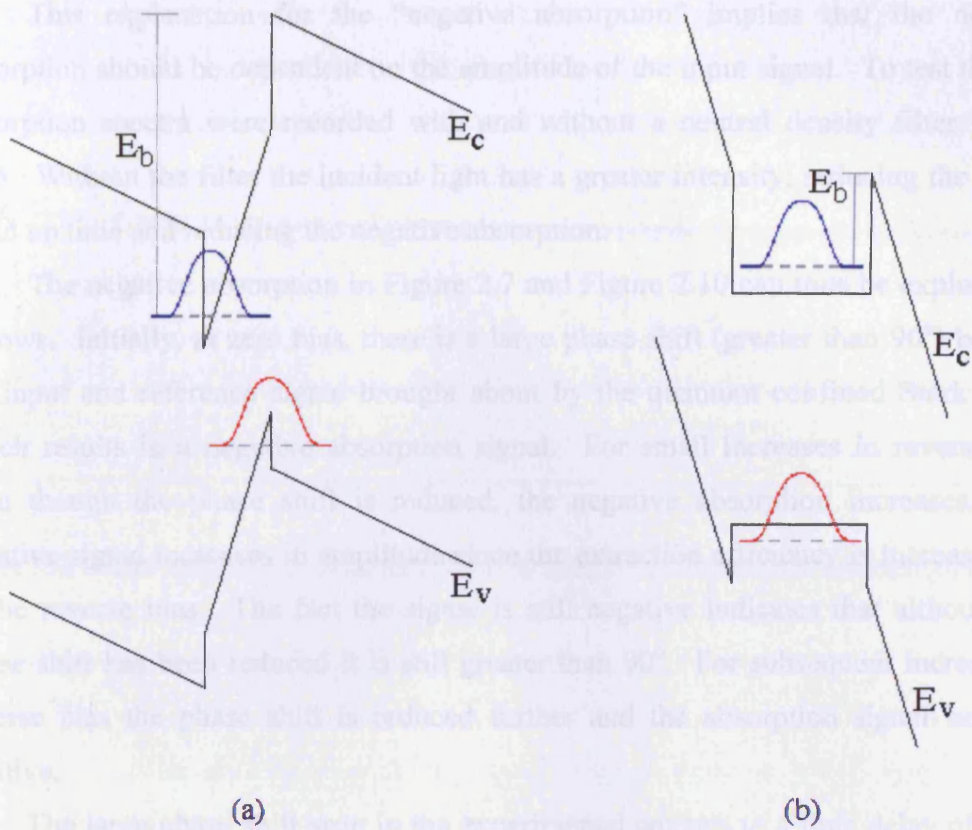
(a)   (b)

Figure 2.15 – Schematic band diagram of a QW under a) zero bias and b) reverse bias.
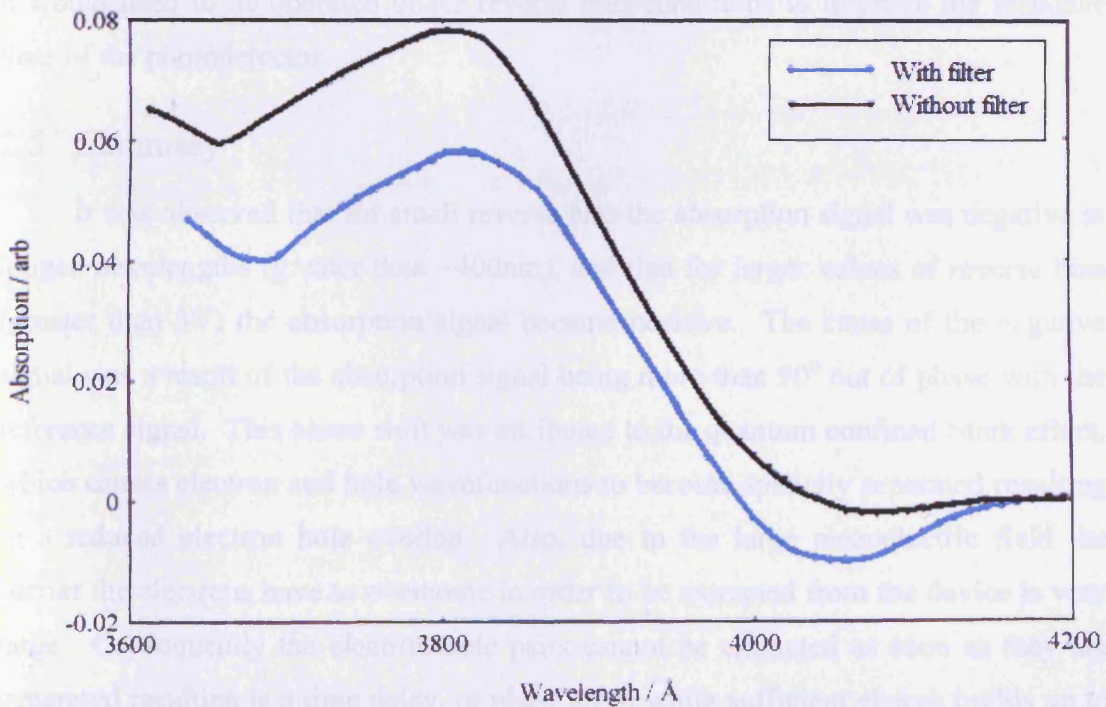

Figure 2.16 – Photocurrent absorption with and without a neutral density filter.

This explanation for the "negative absorption" implies that the negative absorption should be dependent on the amplitude of the input signal. To test this, the absorption spectra were recorded with and without a neutral density filter, Figure 2.16. Without the filter the incident light has a greater intensity, reducing the charge build up time and reducing the negative absorption.

The negative absorption in Figure 2.7 and Figure 2.10 can thus be explained as follows. Initially, at zero bias, there is a large phase shift (greater than 90°) between the input and reference signal brought about by the quantum confined Stark effect, which results in a negative absorption signal. For small increases in reverse bias, even though the phase shift is reduced, the negative absorption increases. The negative signal increases in amplitude since the extraction efficiency is increased due to the reverse bias. The fact the signal is still negative indicates that although the phase shift has been reduced it is still greater than 90°. For subsequent increases in reverse bias the phase shift is reduced further and the absorption signal becomes positive.

The large phase shift seen in the experimental equates to a time delay of a few milliseconds between the absorption signal detected by the GaN nitride layers and that detected by the InGaN QW. Therefore if InGaN is to be used as a p-i-n photodetector it would need to be operated under reverse bias conditions to improve the response time of the photodetector.

2.5 Summary

It was observed that for small reverse bias the absorption signal was negative at longer wavelengths (greater than ~400nm), and that for larger values of reverse bias (greater than 3V) the absorption signal became positive. The cause of the negative signal was a result of the absorption signal being more than 90° out of phase with the reference signal. This phase shift was attributed to the quantum confined Stark effect, which causes electron and hole wavefunctions to become spatially separated resulting in a reduced electron hole overlap. Also, due to the large piezoelectric field the barrier the electrons have to overcome in order to be extracted from the device is very large. Consequently the electron hole pairs cannot be extracted as soon as they are generated resulting is a time delay, or phase shift, while sufficient charge builds up to allow the electrons to be extracted. As the reverse bias is increased the apparent

barrier the electrons have to overcome is reduced, reducing the phase shift. When the phase shift is less than 90° the absorption signal becomes positive.

A comparison was made between the energy of the TE and TM peak absorption. Based on the knowledge that only *lh* transitions have a TM component it was concluded that the ground state *hh* transition lies closest to the valence band edge, and the *lh* energy level is approximately 10meV about the *hh* energy level. This agrees with the calculations of Yeo et al. [6] who also show the *hh* transition to be closest to the valence band in biaxial compressed InGaN QWs.

Large differences are reported in the literature between experimentally determined and theoretically calculated piezoelectric fields[1]. We believe this inconsistency arises due to the use of the assumption that the depletion width can be approximated using an abrupt p-n junction. Reverse bias photocurrent absorption was used to determine the strength of the piezoelectric field within a set of InGaN QW devices, the value needed to obtain a square QW was determined to be 8.5V. Using an approximation for the depletion width appropriate to a p-*i*-n structure, the piezoelectric field within the QW was determined to be (1.9 ± 0.15) MVcm^{-1}. This is in good agreement with the value of 1.8 MVcm^{-1}[7] calculated theoretically using values for the piezoelectric coefficients interpolation from the binary values of InN and GaN, supporting our belief that the discrepancies in the literature between theoretically calculated and experimentally determined values of the piezoelectric field may be due to the assumption that the depletion width can be modelled using an abrupt p-n junction approximation.

2.6 References

1.   T. Takeuchi, C. Wetzel, S. Yamaguchi, H. Sakai, H. Amano, I. Akasaki, Y. Kaneko, S. Nakagawa, Y. Yamaoka, and N. Yamada, *Determination of piezoelectric fields in strained GaInN quantum wells using the quantum-confined Stark effect*. Applied Physics Letters, 1998. **73**(12): p. 1691-1693.

2.   H.D. Summers, P.M. Smowton, P. Blood, M. Dineen, R.M. Perks, D.P. Bour, and M. Kneissel, *Spatially and spectrally resolved measurement of optical loss in InGaN laser structures*. Journal of Crystal Growth, 2001. **230**(3-4): p. 517-521.

3.   P.M. Smowton, P. Blood, P.C. Mogensen, and D.P. Bour, *Role of sublinear gain-current relationship in compressive and tensile strained 630 nm GaInP lasers*. International Journal of Optoelectronics, 1995. **10**(5): p. 383-391.

4.   Y.D. Jho, J.S. Yahng, E. Oh, and D.S. Kim, *Measurement of piezoelectric field and tunneling times in strongly biased InGaN/GaN quantum wells*. Applied Physics Letters, 2001. **79**(8): p. 1130-1132.

5.   W. Liu, K.L. Teo, M.F. Li, S.J. Chua, K. Uchida, H. Tokunaga, N. Akutsu, and K. Matsumoto, *The study of piezoelectric effect in wurtzite GaN/InGaN/AlGaN multilayer structures*. Journal of Crystal Growth, 1998. **190**: p. 648-651.

6.   Y.C. Yeo, T.C. Chong, M.F. Li, and W.J. Fan, *Analysis of optical gain and threshold current density of wurtzite InGaN/GaN/AlGaN quantum well lasers*. Journal of Applied Physics, 1998. **84**(4): p. 1813-1819.

7.   I.H. Brown, I.A. Pope, P.M. Smowton, P. Blood, J.D. Thomson, W.W. Chow, D.P. Bour, and M. Kneissel, *Internal Field Effects in InGaN Quantum Wells*. Submitted to Applied Physics Letters.

3 LED Characterisation

3.1 Introduction

In this chapter the light-current-voltage (IVL) and emission spectra characteristics of InGaN/GaN quantum well LEDs will be investigated. The LEDs were grown at the Department of Materials Science and Metallurgy, University of Cambridge by Dr Menno Kappers, using low-pressure metalorganic vapour phase epitaxy on (0001) orientated sapphire and nominally consist of 0.9μm undoped GaN and 1.35μm Si-doped n-GaN. The active region consists of five 2.6nm $In_{0.16}Ga_{0.84}N$ QWs embedded between 18nm undoped GaN barriers. The top of the device is capped with 0.2μm of Mg-doped p-GaN. X-ray diffraction was used to determine the layer thickness and indium composition. The devices were fabricated into LEDs by etching down to the n-GaN layer to form the n-contact, with the p-contact deposited directly onto the p-GaN. The devices were provided in fabricated form by Cambridge; a schematic representation of the device is shown in Figure 3.1.
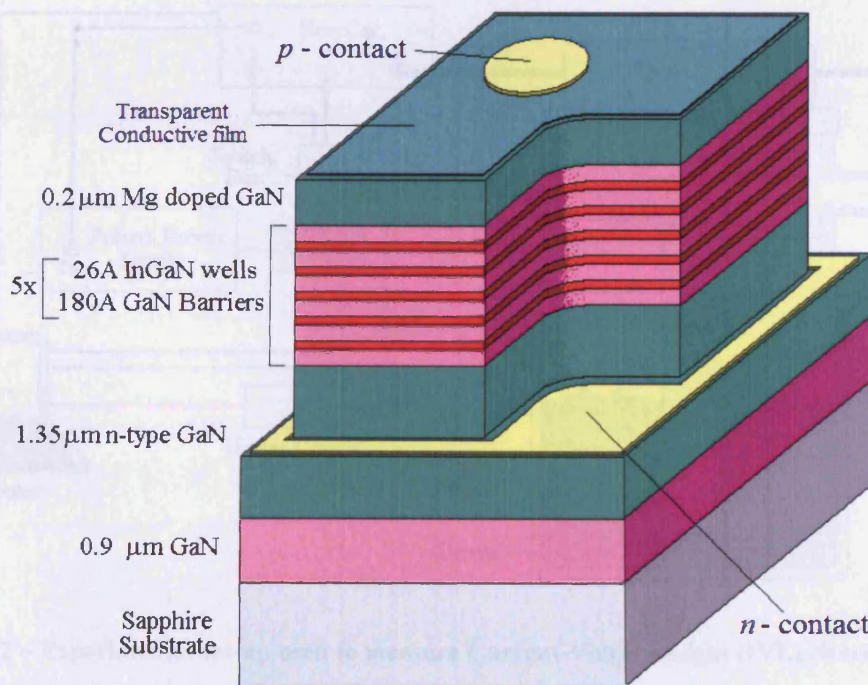

Figure 3.1 – Schematic diagram of the Cambridge $In_{0.16}Ga_{0.84}N$/GaN QW-LED.

3.2 Experimental Techniques

In this section the experimental set up and techniques used to measure the current-voltage (IV) & light-current (LI) characteristics (IVL Measurements), along with emission spectra measurements will be outlined.

3.2.1 IVL Measurements

The IVL measurements were taken using equipment already set up in the laboratory. To control the temperature of the LED it was placed on a cold finger inside a cryostat (Figure 3.2). The external part of the cold finger was placed in a dewar of liquid nitrogen allowing the LED to be cooled. Due to the thermal gradient across the cold finger the minimum temperature that could be reached was 100K. When taking measurements the LED was cooled to 10K below the desired start temperature, the cold finger was then removed from the liquid nitrogen and left to slowly warm up. The temperature of the LED is monitored by the computer via a diode located at the top of the cold finger (see Figure 3.2). When the LED reaches the desired start temperature the computer records the IVL characteristics. There is no feedback mechanism to maintain the desired temperature, however the rapid speed at which the computer records the IVL data ensures there is minimal ($^1/_2$°C) temperature drift over each set of measurements.
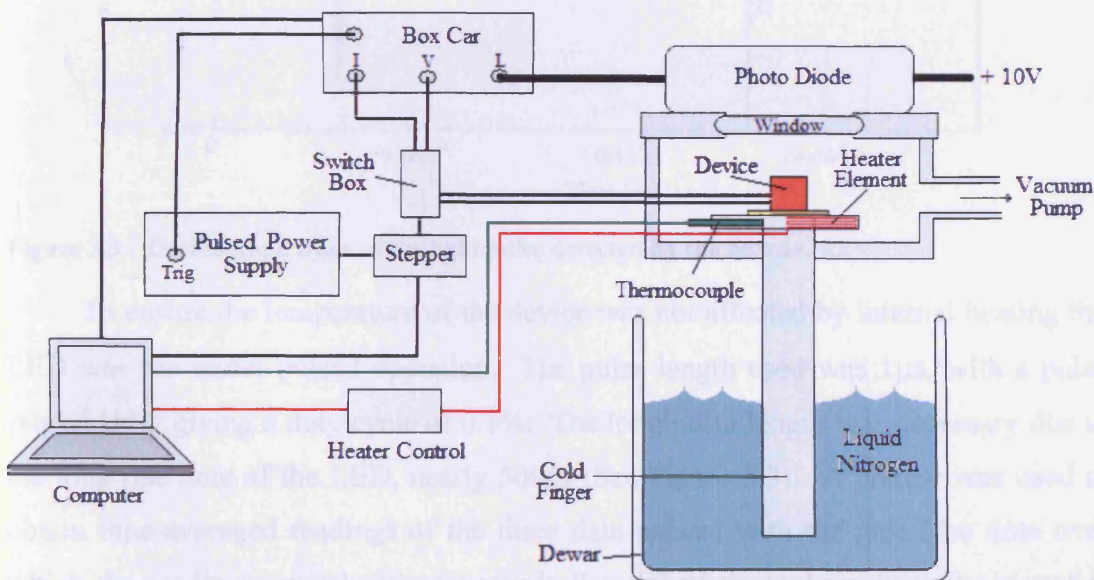

Figure 3.2 – Experimental set-up used to measure Current-Voltage-Light (IVL) characteristics.

The computer controls the current supplied to the device via the stepper motor, which incrementally increases/decreases the current between zero and the maximum value set on the pulsed power supply. When the device reaches 290K the computer switches the heater on, this allows the temperature of the device to be raised to 400K. A silicon photo-diode is used to measure the light emitted from the device, which is collected through a window in the top of the cryostat. It is possible to place two devices in the cryostat at the same time; the IVL characteristics of the separate devices are then recorded at 5K intervals (e.g. the first set of measurements on device 1 are recoded at 110K, while the first set of measurements of device 2 are recorded at 115K), the computer switches between the two devices using a relay inside the switch box indicated in Figure 3.2.
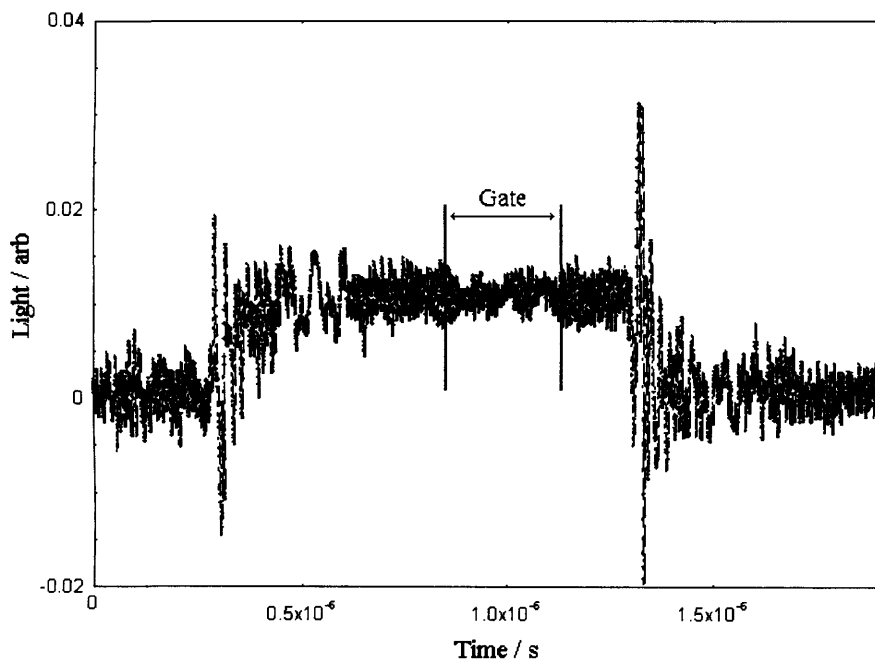
Figure 3.3 – Oscilloscope trace of the light pulse detected by the boxcar.

To ensure the temperature of the device was not affected by internal heating the LED was run under pulsed operation. The pulse length used was $1\mu s$, with a pulse rate of 1kHz giving a duty cycle of 0.1%. The long pulse length was necessary due to the long rise time of the LED, nearly 500ns (See Figure 3.3). A boxcar was used to obtain time-averaged readings of the three data pulses, with the gate (the time over which the readings are taken) set towards the end of the pulse where the signal is constant. The fact that the pulse remains flat, within the background noise, after the initial rise time indicates the device is not experiencing any internal heating. If the devices were heating up during the duration of the pulse one would expect the

intensity of the light signal to decrease. Attention also needs to be paid to average heating. This is where there is a negligible amount of heat generated during a single pulse, however over many pulses the heat builds up until it is no longer negligible. To check for average heating the light pulse was recorded, the device was left running for 10 minutes and then the light pulse recorded for a second time. Any drop in intensity between the first and second recoding would be an indication of the presence of average heating. No such drop in intensity was observed.

3.2.2 Emission Spectra Measurements

The experimental set up, used to measure the emission spectra, is shown in Figure 3.4.
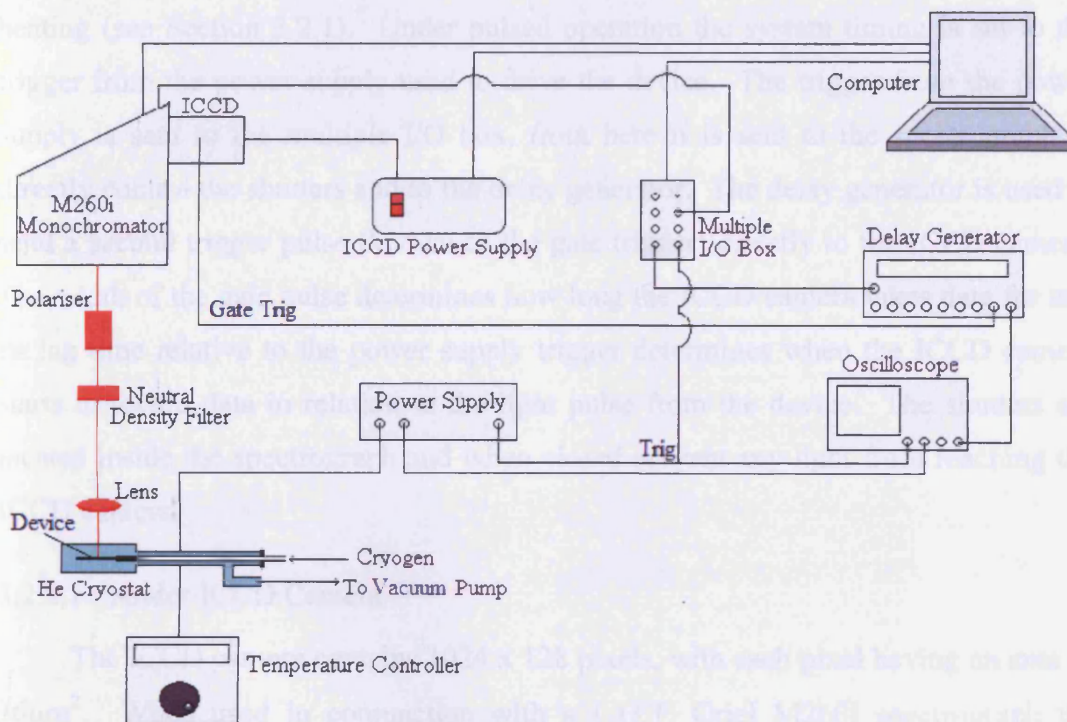
Figure 3.4 – Integrated Charged Coupled Device (ICCD) camera system used to measure LED emission spectra.

The LED was placed on the cold finger of an Oxford Instruments Microstat[He] continuous flow cryostat; this allows the LED to be cooled to a minimum temperature of 70K if using liquid nitrogen or 10K if using liquid helium. The cryostat is mounted on a translation stage, allowing adjustment in the three Cartesian directions and there are two rotational stages to allow the device to be rotated in the horizontal and vertical planes. Previous experiments on a similar system showed that the torque resulting from the weight of the cryostat causes creep in the alignment of the system. To

counteract this problem the cryostat has been fitted with a counterbalance system allowing the cryostat to be perfectly balanced, thus eliminating any torque. To reduce any vibrational effects the table on which the system is mounted is placed on rubber pads.

Light from the device was focused onto the slits of an L.O.T. Oriel M260i spectrograph using a x20 Mitutoyo NUV microscope objective. The spectrograph contains three different lined gratings, 300, 600 & 1200 respectively, which are computer controlled. After passing through the spectrograph the light is detected using an Andor Integrated Charged Coupled Device (ICCD) Camera. The ICCD camera is explained in greater detail below in part 3.2.2.1.

Measurements on the device are taken under pulsed operation to avoid internal heating (see Section 3.2.1). Under pulsed operation the system timing is set to the trigger from the power supply used to drive the device. The trigger from the power supply is sent to the multiple I/O box, from here it is sent to the spectrograph to directly control the shutters and to the delay generator. The delay generator is used to send a second trigger pulse (known as the gate trigger) directly to the ICCD camera. The width of the gate pulse determines how long the ICCD camera takes data for and its lag time relative to the power supply trigger determines when the ICCD camera starts to record data in relation to the light pulse from the device. The shutters are located inside the spectrograph and when closed prevent any light from reaching the ICCD camera.

3.2.2.1 Andor ICCD Camera

The ICCD camera contains 1024 x 128 pixels, with each pixel having an area of $26\mu m^2$. When used in conjunction with a L.O.T. Oriel M260i spectrograph the camera provides spectral information along the horizontal or x-axis and spatial information along the vertical or z-axis. There are a number of different acquisition modes to which the camera may be set, however, only those relevant to this experiment will be mentioned here.

For all the data collected in this section the acquisition mode was set to Full Vertical Binning. In this mode the charge from each column of pixels is combined or "binned" to give a single value per column. This allows the CCD-chip to be used as a linear image sensor. It is also possible to add together, in the computer memory, the

data from a number of different scans to create an accumulated scan. This helps to pick out the signal from any noise.

3.2.2.2   Temperature Control System

The temperature of the device is controlled using the system shown in Figure 3.5. Liquid nitrogen is pumped from the dewar, along the transfer tube to the cryostat. Here the nitrogen is brought into contact with the heat exchanger. The heat exchanger transfers heat between the cold finger (on which the device is placed) and the nitrogen thus cooling the device. The heated nitrogen is then pumped back along the transfer tube, through the flow meter and flow pump and is then vented as an exhaust gas. The rate at which nitrogen is pumped through the system can be controlled using the flow meter. The faster the nitrogen is pumped through the system the colder the device gets. To control the temperature more precisely a heater element is wound around the heat exchanger, which is controlled via the ITC 601 temperature controller. Feedback to the temperature controller is provided via a thermocouple embedded within the heat exchanger. This allows the temperature of the device to be maintained to within $^+/. 0.1$K over the temperature range 70 - 400 K.

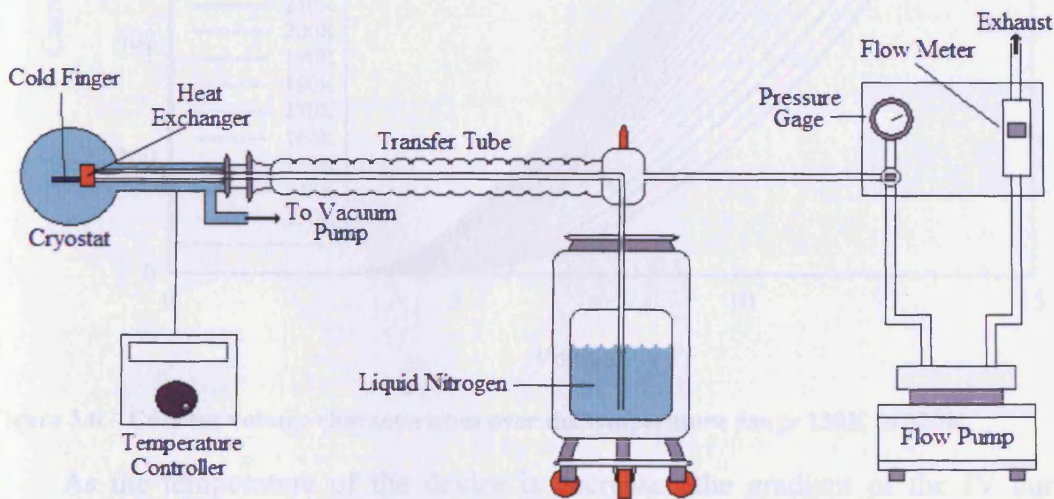**Figure 3.5 – Temperature control system.**

3.3 Results and Discussion

3.3.1 Current Voltage Characteristics

The current voltage (IV) characteristics of the Cambridge LED, over the temperature range 130K to 320K, are shown in Figure 3.6. Using Ohm's law it is possible to work out the resistance of the device by taking the gradient of the IV curve. The resistance should be the value tended to at high currents, i.e. in the linear regime of the graph, since the diode characteristic influences the value at low currents. An example of calculating the resistance is given in Figure 3.6, for the 300K curve, where the resistance is calculated to be 6.6Ω.
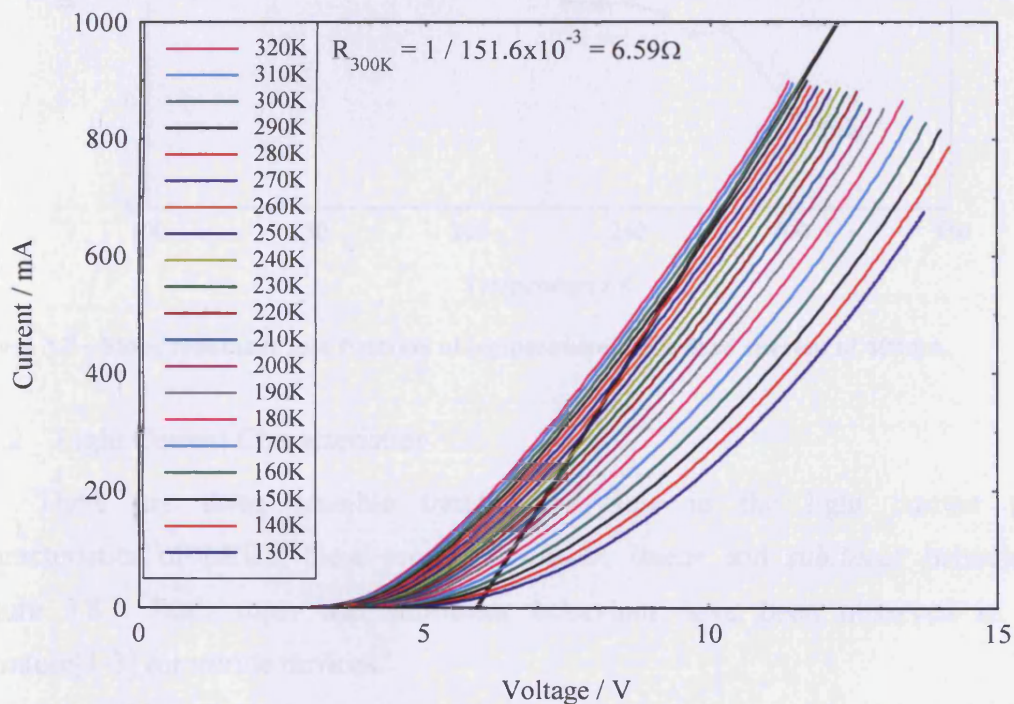
Figure 3.6 – Current voltage characteristics over the temperature range 130K to 320K.

As the temperature of the device is decreased the gradient of the IV curves decreases and thus the device resistance increases, Figure 3.7. This is due to the fact that in order for a semiconductor to conduct a current there must be electrons present in the conduction band, assuming semiconductor is n-type. As the semiconductor is cooled k_BT decreases and more free carriers are confined to the donor atoms, reducing the number of free carreiers present in the conduction band. Eventually as you approach 0K all the carriers are confined to the donor atoms and the semiconductors resistance goes to infinity. The resistance or conductivity also depends on the

mobility of the doped layers, which is also temperature dependent. Over the temperature range investigated it is expected that the resistance will increase as the temperature is decreased. The temperature dependence of the free carrier density and the mobility are examined in chapters 4 and 5.
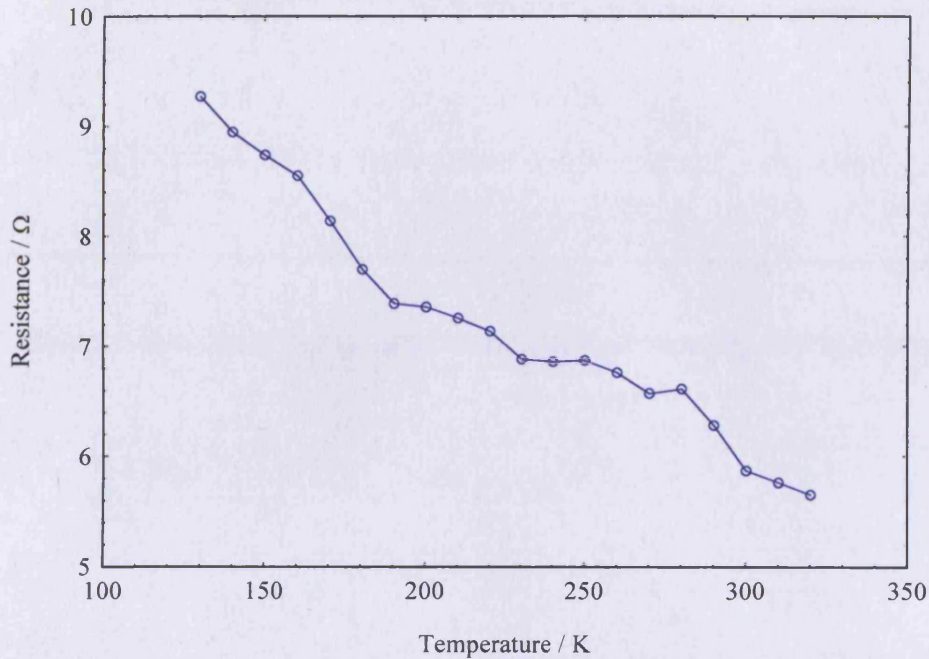

Figure 3.7 – Slope resistance as a function of temperature, for a fixed current of 600mA.

3.3.2   Light Current Characteristics

There are three possible trends observable in the light current (LI) characteristics of LEDs; these are, *super-linear*, *linear* and *sublinear* behaviour, Figure 3.8.   Both super and sub-linear behaviour have been observed in the literature[1-3] for nitride devices.

Super-linear behaviour occurs when non-radiative recombination (which is proportional to the number of carriers, n) is the dominant loss mechanism and has a weaker dependancy than the radiative recombination rate. As the current is increased radiative recombination, which is proportional to the square of the density of carriers, begins to dominate and the LI curve bends upwards resulting in super-linear behaviour, which eventually becomes linear.

Sublinear behaviour is the result of a non-radiative process which increases at a rate greater than n^2, in narrow band gap materials this is usually attributed to Auger recombination which has an n^3 dependency, assuming the device does not suffer from internal heating, which may also produce sub-linear behaviour.
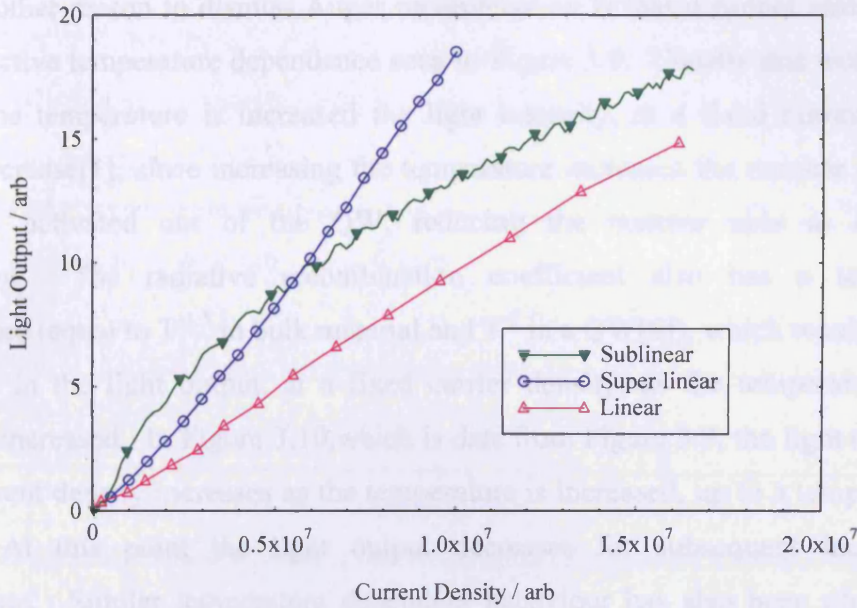
Figure 3.8 – 300K experimental light current curves showing super linear (blue circles), linear (pink triangles) and sublinear (green triangles) behaviour. The individual curves have been scaled to allow them to be shown on the same plot. Structural details of the linear LED are given in Table 5.1, super linear LED data provided by John Thomson.

The LEDs investigated exhibited sublinear behaviour over the whole temperature range investigated, Figure 3.9. Since it has already been shown (Section 3.2.1) that the devices do not suffer from internal heating, it may seem reasonable to conclude that the sublinear behaviour is due to Auger recombination. However this is considered unlikely to dominate in wide bandgap materials and Auger coefficients as low as $C=10^{-34}$cm^{6}s^{-1} [4] have been estimated, a difference of almost 8 orders of magnitude as compared to $C=9\times10^{-27}$cm^{6}s^{-1} [5] for InGaAs.

Figure 3.9 – Light current characteristics for temperatures ranging from a) 130K - 250K and b) 250K - 330K. Both graphs are for the same device and results are typical of all devices tested.

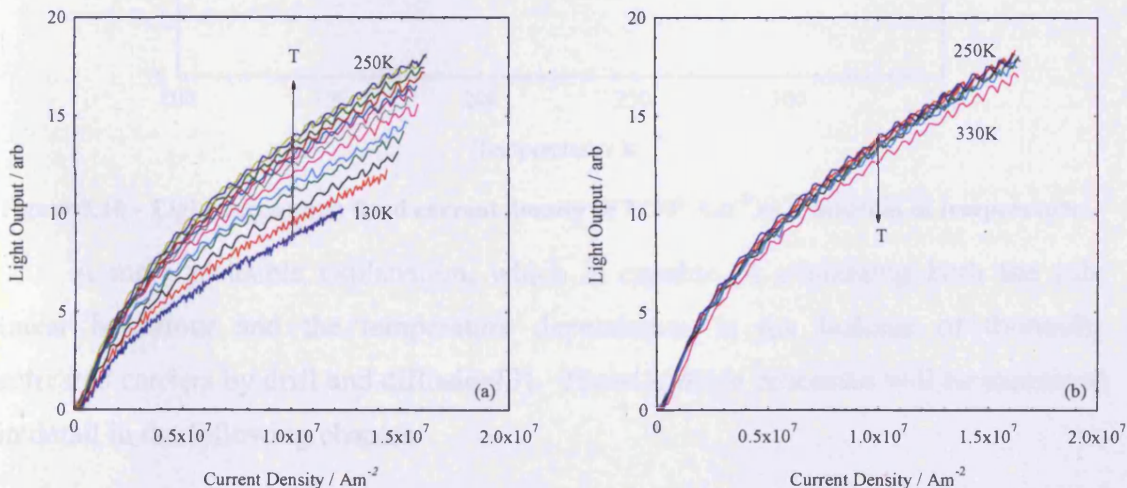Another reason to dismiss Auger recombination is that it cannot easily explain the distinctive temperature dependence seen in Figure 3.9. Usually one would expect that as the temperature is increased the light intensity, at a fixed current density, would decrease[1], since increasing the temperature increases the number of carriers thermally activated out of the QW, reducing the number able to recombine radiatively. The radiative recombination coefficient also has a temperature dependence (equal to $T^{-1.5}$ in bulk material and T^{-1} in a QW[6]), which would lead to a reduction in the light output, at a fixed carrier density, as the temperature of the device is increased. In Figure 3.10, which is data from Figure 3.9, the light output at a fixed current density increases as the temperature is increased, up to a temperature of 250K. At this point the light output decreases for subsequent increases in temperature. Similar temperature dependent behaviour has also been observed by others in the literature[7], however the temperature at which the light output starts to decrease occurs at a lower temperature, 193K[7].

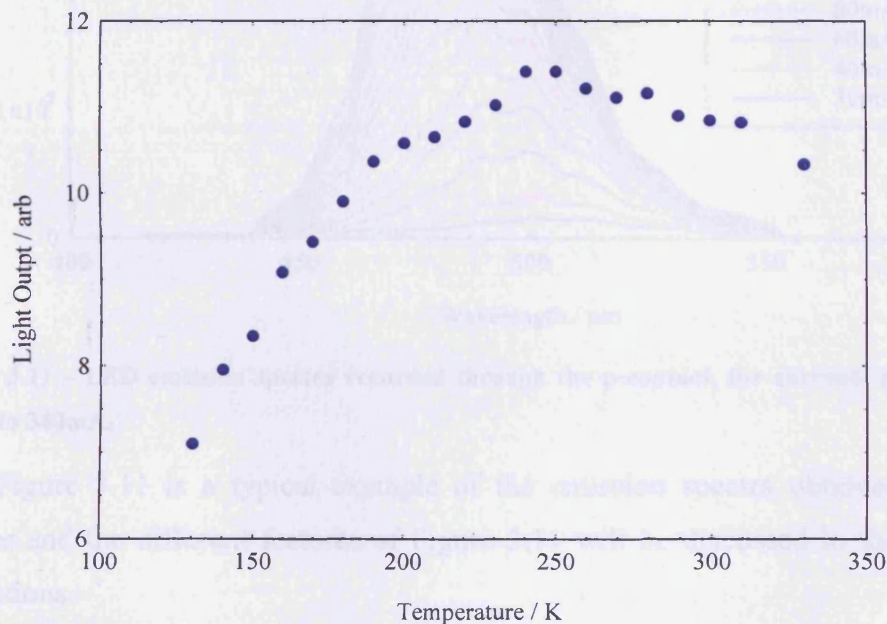**Figure 3.10 – Light output at a fixed current density of 7×10^6 Am^{-2} as a function of temperature.**

A more plausible explanation, which is capable of explaining both the sub-linear behaviour and the temperature dependence, is the leakage of thermally activated carriers by drift and diffusion[3]. These leakage processes will be examined in detail in the following chapter.

3.3.3   Emission Spectra

For the following measurements the pulse length was set to 1μs, with a pulse rate of 1kHz, giving a duty cycle of 0.01%. These settings were used to avoid internal heating, as explained in section 3.2.1. The number of accumulations per scan was set to 200 and the spectral resolution was 0.5nm.
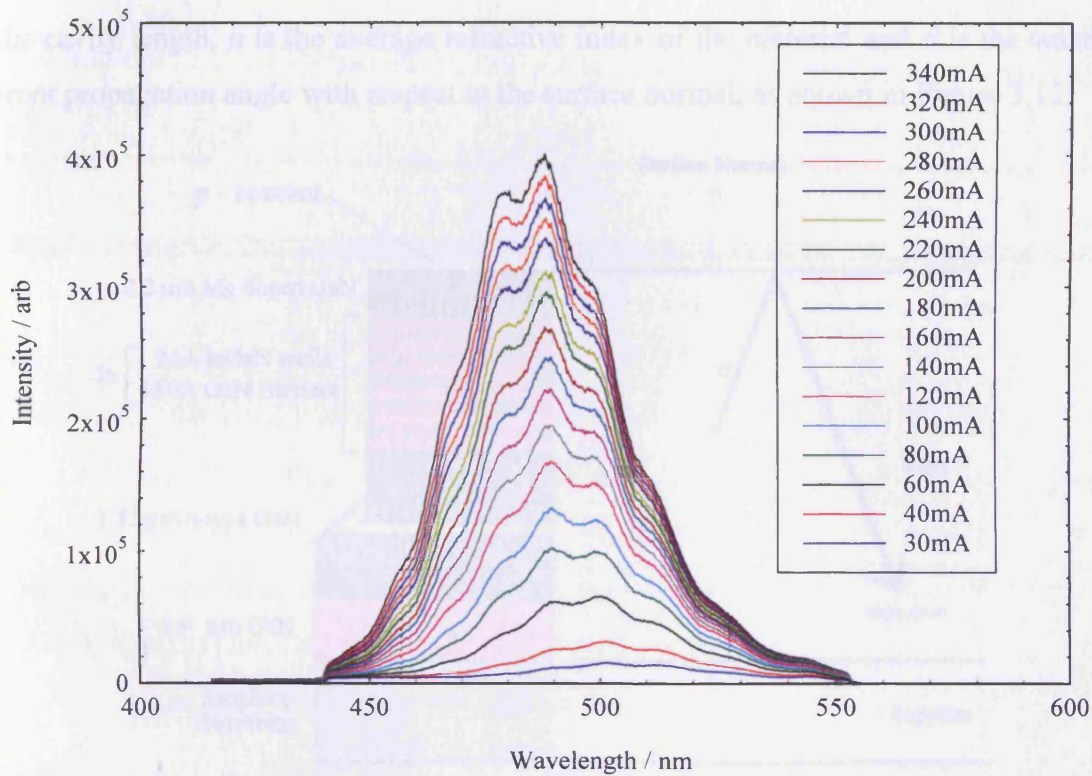
Figure 3.11 – LED emission spectra recorded through the p-contact, for currents ranging from 30mA to 340mA.

Figure 3.11 is a typical example of the emission spectra obtained for these devices and the different features of Figure 3.11 will be discussed in the following subsections.

3.3.3.1   Fringes

Examining the emission spectra in Figure 3.11 we see that as well as the main peak there are a number of additional fringes superimposed on the spectra. Similar features have also been observed by others[8-10] in GaN based devices and have been attributed to Fabry-Perot interference fringes. Similar structure observed in the photoluminescence spectra of porous silicon are also well documented[11-13] and

again have been attributed to Fabry-Perot interference fringes. The condition for constructive interference is given by[13, 14]

$$m\lambda_o = 2dn\cos\theta$$

where, m is the interference order, λ_o is the wavelength of the propagating light, d is the cavity length, n is the average refractive index of the material and θ is the wave-front propagation angle with respect to the surface normal, as shown in Figure 3.12.
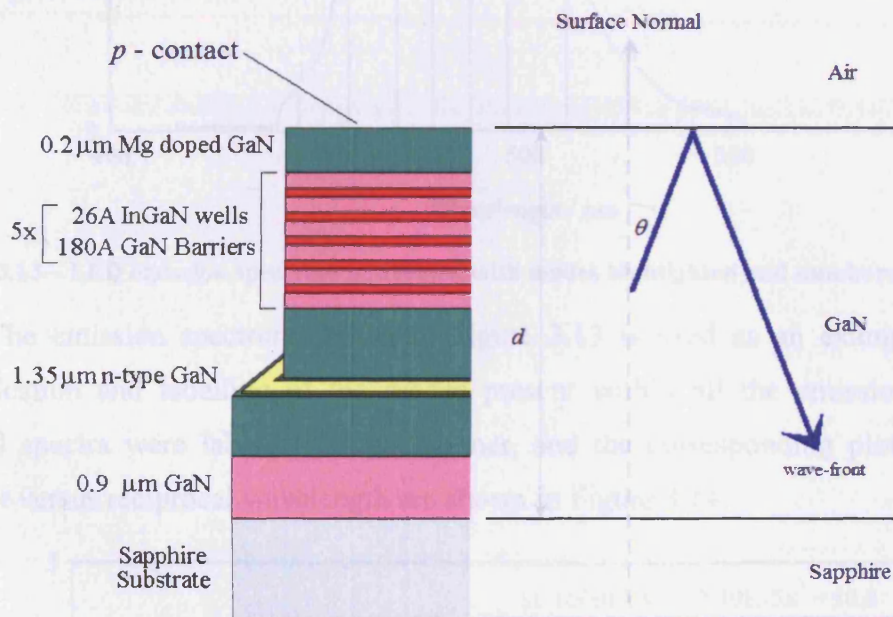
Figure 3.12 – Schematic diagram illustrating the Air/GaN/Sapphire Fabry-Perot cavity within the device.

Since the light is extracted through the p-contact we can assume the collected light rays are normal to the device (i.e. $\theta = 0°$) and Equation 3.1 simplifies to become Equation 3.2.

$$m = \frac{2dn}{\lambda_0}$$

A graph of peak number plotted against reciprocal wavelength will then have a gradient equal to $2dn$ from which the thickness of the cavity needed to produce the interference fringes can be calculated. n is taken to be 2.5[8, 15].
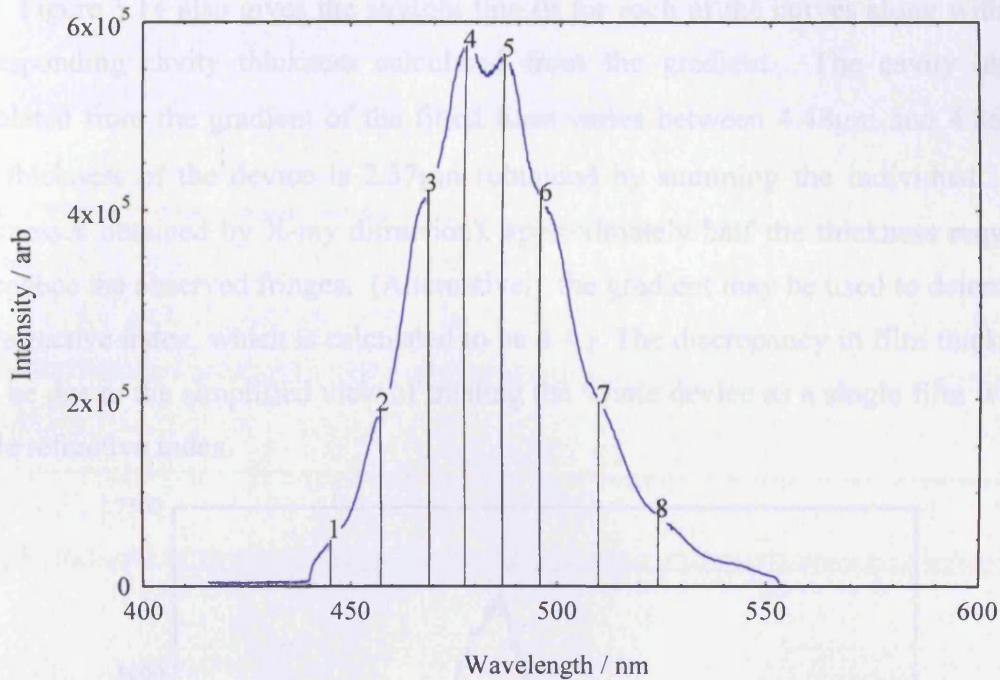
Figure 3.13 – LED emission spectrum at 620mA, with modes highlighted and numbered.

The emission spectrum shown in Figure 3.13 is used as an example of the identification and labelling of the modes present within all the emission spectra. Several spectra were labelled in this manner, and the corresponding plots of peak number versus reciprocal wavelength are shown in Figure 3.14.

@ 160mA $y = -2.39\text{E-}5x^1 + 50.9$

@ 120mA $y = -2.43\text{E-}5x^1 + 51.8$

@ 80 mA $y = -2.38\text{E-}5x^1 + 50.6$

@ 40mA $y = -2.24\text{E-}5x^1 + 47.7$

160mA ≡ 4.78μm
120mA ≡ 4.86μm
80mA ≡ 4.76μm
40mA ≡ 4.48μm

Figure 3.14 – Graph showing peak/mode number plotted as a function of reciprocal wavelength.

Figure 3.14 also gives the straight line fit for each of the curves along with the corresponding cavity thickness calculated from the gradient. The cavity length calculated from the gradient of the fitted lines varies between 4.48μm and 4.86μm. The thickness of the device is 2.57μm (obtained by summing the individual layer thicknesses obtained by X-ray difraction), approximately half the thickness required to produce the observed fringes. (Alternatively the gradient may be used to determine the refractive index, which is calculated to be 4.4.) The discrepancy in film thickness may be due to the simplified view of treating the whole device as a single film with a single refractive index.
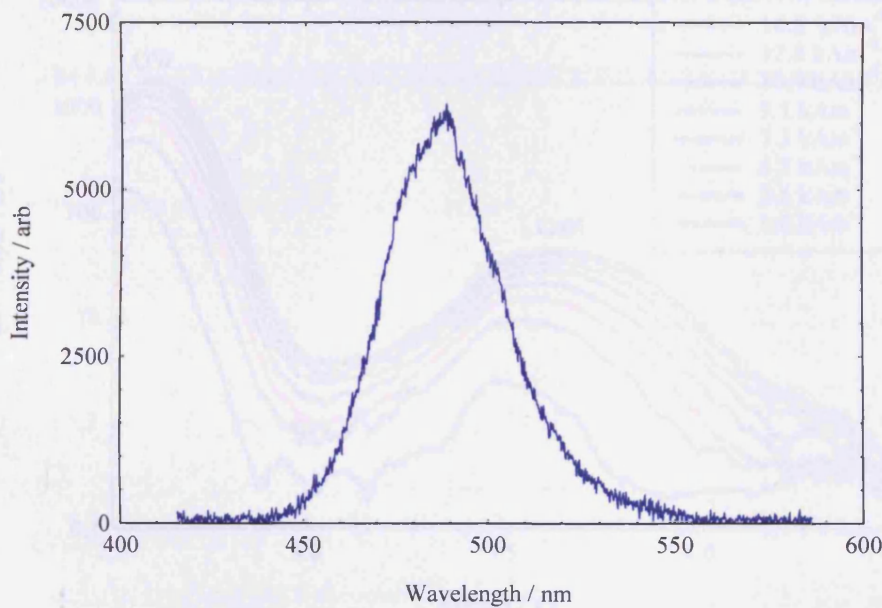
Figure 3.15 – LED emission spectrum taken from the side of the device. There are no interference fringes since $\theta_t = 0°$.

If the features seen in the emission spectra are due to interference fringes their wavelength and amplitude should change with the observation angle according to Equation 3.1. However if the 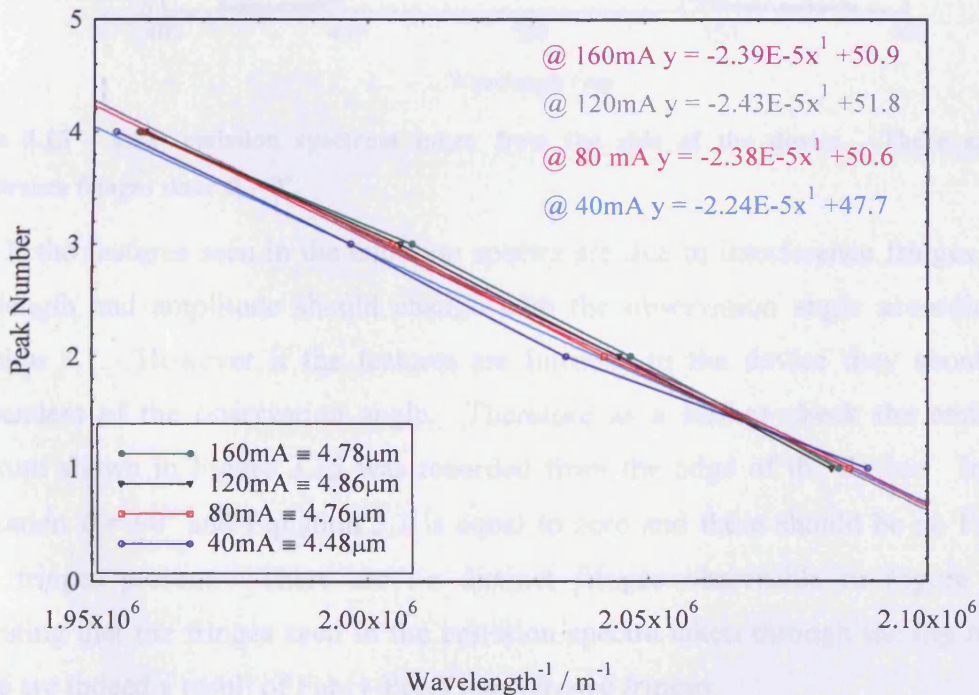features are intrinsic to the device they should be independent of the observation angle. Therefore as a further check the emission spectrum shown in Figure 3.15 was recorded from the edge of the device. In this orientation $\theta = 90°$ and Equation 3.1 is equal to zero and there should be no Fabry-Perot fringes present. There are no distinct fringes observable in Figure 3.15 suggesting that the fringes seen in the emission spectra taken through the top of the device are indeed a result of Fabry-Perot interference fringes.

3.3.3.2 Emission From GaN Layers

Figure 3.16 shows the measured spontaneous emission spectra centred at GaN wavelengths, ~360nm. There are two discernable peaks, with the low energy peak corresponding to emission from the active region and the higher energy peak corresponding to emission from the GaN layers. The emission shown in Figure 3.16 are from the same device as Figure 3.11, however emission from the GaN layers cannot be seen in Figure 3.11 due to the intensity scale used and the wavelength range the data was taken over.
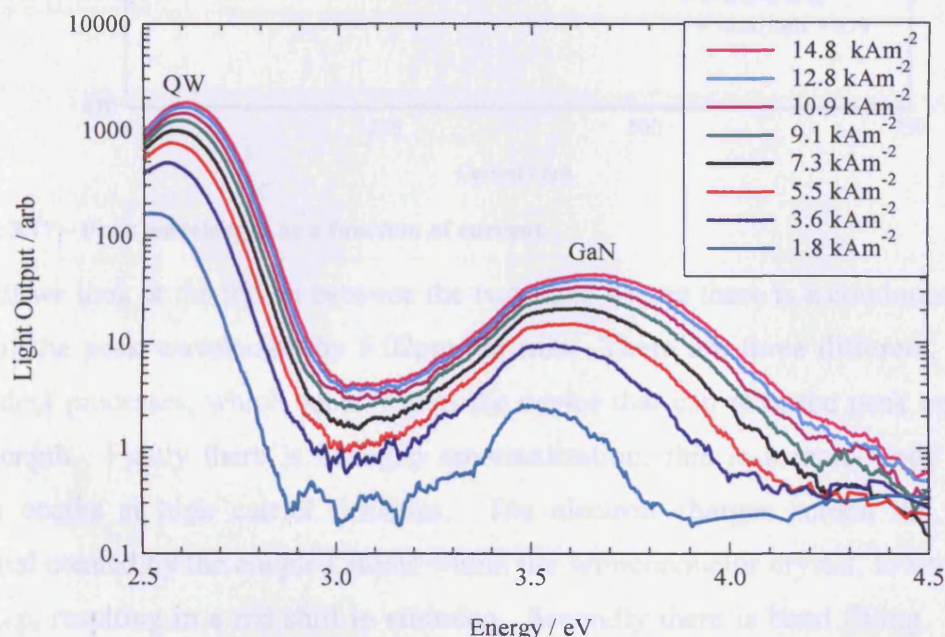
Figure 3.16 – Spontaneous emission spectra showing emission from both the QW and the GaN layers.

Although the emission from the GaN layer is two orders of magnitude less than the emission from the QW it shows that not all the carriers are confined to the QW (since some are able to recombine radiatively in the GaN layers) and suggests that leakage currents may be significant within these devices.

3.3.3.3 Peak Wavelength as a Function of Current

The QW peak wavelength as a function of current is shown in Figure 3.17. We can see two distinct steps or breaks where the peak suddenly jumps to shorter wavelengths, these steps occur at approximately 70mA and 520mA and are consistent with the peak switching between the Fabry-Perot modes indicated in Figure 3.13.
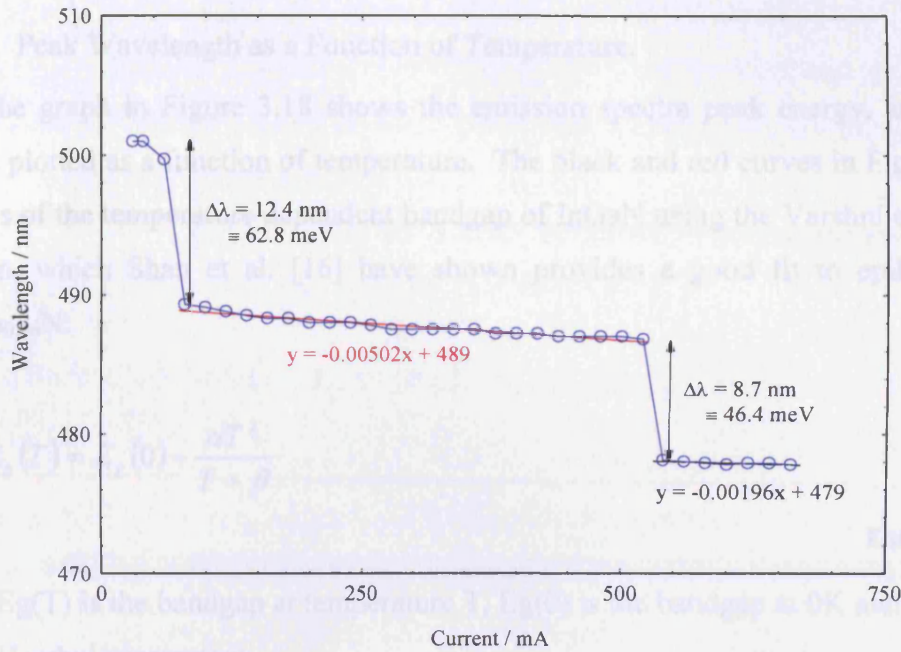
Figure 3.17 – Peak wavelength as a function of current.

If we look at the region between the two steps we see there is a continuous blue shift of the peak wavelength by 5.02pm per mA. There are three different, carrier dependent processes, which occur within the device that can alter the peak emission wavelength. Firstly there is bandgap renormalization; this is a many-body effect, which occurs at high carrier densities. The electron charges screen the energy potential created by the coupled atoms within the semiconductor crystal, lowering the bandgap, resulting in a red shift in emission. Secondly there is band filling. As the current is increased the energy levels are filled and the peak moves to shorter wavelengths. Finally there is the screening of the piezoelectric effect. The piezoelectric field spatially separates the electron and hole charges, this leads to an electric field, which in turn screens the piezoelectric field. As the carrier density is increased, the screening of the piezoelectric field increases resulting in an increase in the overlap integral and an increase in the energy gap, leading to a blue shift in the emission wavelength. The presence of Fabry-Perot fringes will also have an influence on the peak position, through constraining the peak wavelength to the fringes. The shift in peak wavelength seen Figure 3.17, is a combination of all these processes and is dominated by those that produce a blue shift.

3.3.3.4 Peak Wavelength as a Function of Temperature.

The graph in Figure 3.18 shows the emission spectra peak energy, at a fixed current, plotted as a function of temperature. The black and red curves in Figure 3.18 are plots of the temperature dependent bandgap of InGaN using the Varshni empirical equation, which Shan et al. [16] have shown provides a good fit to epilayers of $In_{0.14}Ga_{0.86}N$:

$$E_g(T) = E_g(0) - \frac{\alpha T^2}{T + \beta}$$

<div align="right">**Equation 3.3**</div>

where, Eg(T) is the bandgap at temperature T, Eg(0) is the bandgap at 0K and α and β are the Varshni parameters.

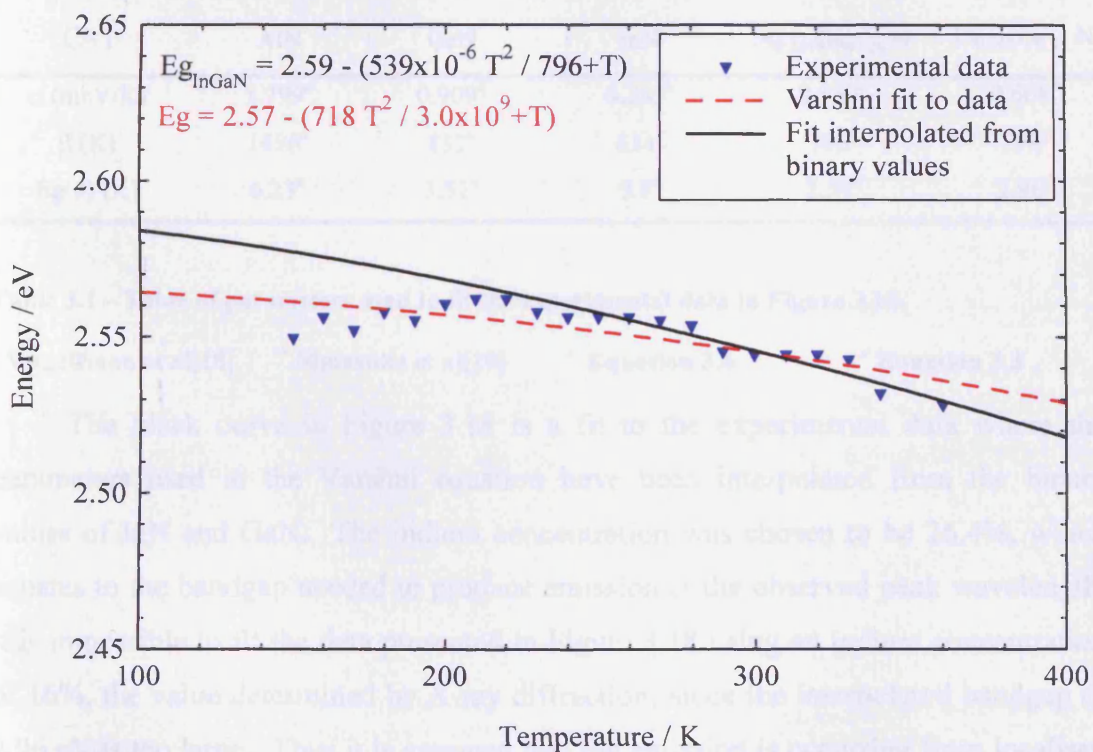**Figure 3.18 – Emission spectra peak energy, at constant current, plotted as a function of temperature (blue triangles). The red curve is a best line fit to the data using the Varshni empirical equation. Black line shows the temperature dependence of the bandgap of InGaN calculated using the Varshni empirical equation where the values used in the equation were interpolated from the binary values using an In concentration of 26.4%.**

The red dashed curve in Figure 3.18 is a best line fit to the data using the Varshni equation and yields values of $E_g(0)$=2.57 eV, α=718 eVK^{-1} and β=3x10^9 K, however these values are so different to those interpolated from the binary values (Table 3.1) they do not seem sensible.

The Varshni parameters may be directly obtained by interpolating from the binary values of GaN and InN using the equation below[17]

$$Z = Ax + B(1 - x) - C(1 - x)x$$

Equation 3.4

where, x is the indium concentration, Z is the parameter value to be calculated (α or β), C is a bowing parameter to help improve the fit and A and B are the relevant values for InN and GaN respectively. These values are given in Table 3.1.

C=1	AlN	GaN	InN	$In_{0.264}Ga_{0.736}$ N	$In_{0.16}Ga_{0.84}$ N
α (meV/K)	1.799^a	0.909^a	0.245^a	0.539^c	0.668^c
β (K)	1496^a	832^a	624^a	796^c	798^c
Eg(0) (K)	6.23^a	3.51^a	0.9^b	2.59^d	2.96^d

Table 3.1 – Table of parameters used to fit the experimental data in Figure 3.18.

[a] **Vugaftman et al[18]**   [b] **Matasuka et al[19]**   [c] **Equation 3.4**   [d] **Equation 3.3**

The black curve in Figure 3.18 is a fit to the experimental data where the parameters used in the Varshni equation have been interpolated from the binary values of InN and GaN. The indium concentration was chosen to be 26.4%, which equates to the bandgap needed to produce emission at the observed peak wavelength. It is impossible to fit the data presented in Figure 3.18 using an indium concentration of 16%, the value determined by X-ray diffraction, since the interpolated bandgap of 2.96 eV is too large. Thus it is assumed that the emission is occurring from localised regions due to the clustering of indium during growth. Such features have been referred to in the literature as quantum disks[20, 21] since their size is usually larger than that of typical or true quantum dots.

Below 210K the measured peak emission energy does not follow the calculated bandgap of InGaN, appearing to red shift as the temperature is reduced. This is believed to be the middle part of the familiar S-shaped behaviour seen in the emission

spectra of InGaN devices[22], which has been shown by Cho et al. [20] only to be present in InGaN QWs where indium clustering is present. Thus further suggesting that the emission is occurring from localised regions with a high indium percentage.

3.3.3.5   Full Width at Half Maximum as a Function of Temperature.

The Full Width at Half Maximum (FWHM), as a function of temperature, for a fixed current is shown in shown in Figure 3.19. There appears to be two distinct regions of behaviour. Over the temperature range 100 to 250K the FWHM only increases slowly (increasing by 1.8 meV between 100 and 250K), after 250K there is a change in the behaviour and the FWHM begins to more rapidly (increasing by 3.8 meV between 250 and 310K).
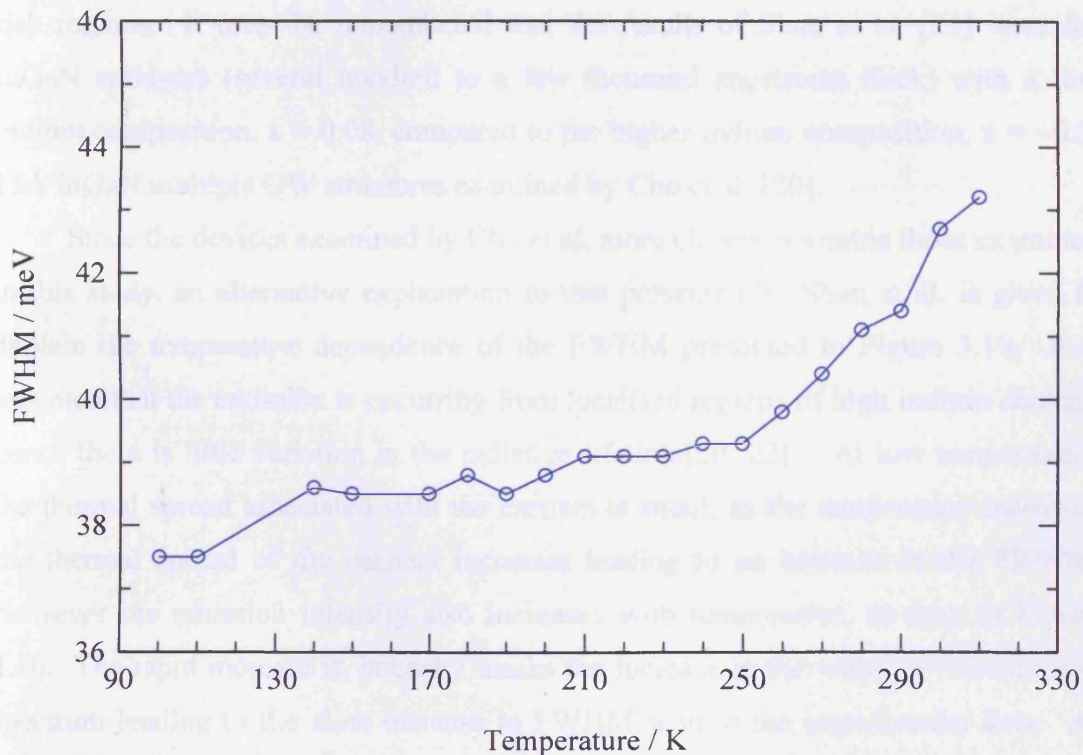
Figure 3.19 – Full Width at Half Maximum (FWHM), at constant current, plotted as a function of temperature.

The temperature-dependent photoluminescence (PL) FWHM has been measured by Shan et al. [23] for epilayers of InGaN. Over the temperature range 10 to 50K there was vary little change in the FWHM, however over the temperature range 50 to 300K there was a twofold increase in the FWHM. It is important to note that the behaviour of the FWHM mirrored the behaviour of the PL intensity, which remained approximately constant over the temperature range 10 to 50K and decreased by three

orders of magnitude over the temperature range 50 to 300K. To explain this behaviour Shan et al. [23] assumed there were large fluctuations in the indium and that emission was band-to-band rather than excitonic. At low temperatures the photoexcited carriers relax down to the lowest available energy state where they recombine with holes in the valence band. As the temperature is increased the PL lifetime decreases rapidly and the diffusion length of the photoexcited carriers reduces, resulting in the recombination of more carriers before they have had time to relax to the local minimum, leading to a broadening of the PL spectrum. However this description is in conflict with the results of Cho et al. [20] which show little change in the PL lifetime with temperature for devices with indium clustering and Chichibu et al. [24] who claim emission occurs from localised excitons within indium rich regions. It must be remembered that the results of Shan et al. [23] were for InGaN epilayers (several hundred to a few thousand angstroms thick) with a low indium composition, x = 0.08, compared to the higher indium composition, x = ~0.3, 15Å InGaN multiple QW structures examined by Cho et al. [20].

Since the devices examined by Cho et al. more closely resemble those examined in this study, an alternative explanation to that presented by Shan et al. is given to explain the temperature dependence of the FWHM presented in Figure 3.19. It is assumed that the emission is occurring from localised regions of high indium content, hence there is little variation in the radiative lifetime[20, 22]. At low temperatures the thermal spread associated with the carriers is small, as the temperature increases the thermal spread of the carriers increases leading to an increase in the FWHM. However the emission intensity also increases with temperature, as seen in Figure 3.10. The rapid increase in intensity masks the increase in the width of the emission spectrum leading to the slow increase in FWHM seen in the experimental data. At approximately 250K the emission intensity stops increasing with temperature and begins to decrease, at this point the increase in the emission intensity no longer masks the increase in the width of the emission spectrum and the FWHM increases at a faster rate.

3.3.4 Photocurrent Absorption Spectra

The room temperature photocurrent absorption spectrum was measured using the experimental technique outlined in chapter 2, section 2.2, and a plot of which is shown in Figure 3.20. Examining Figure 3.20 we see there is no well-defined

absorption edge to the QW, rather there exists an absorption tail which extends to low energies.
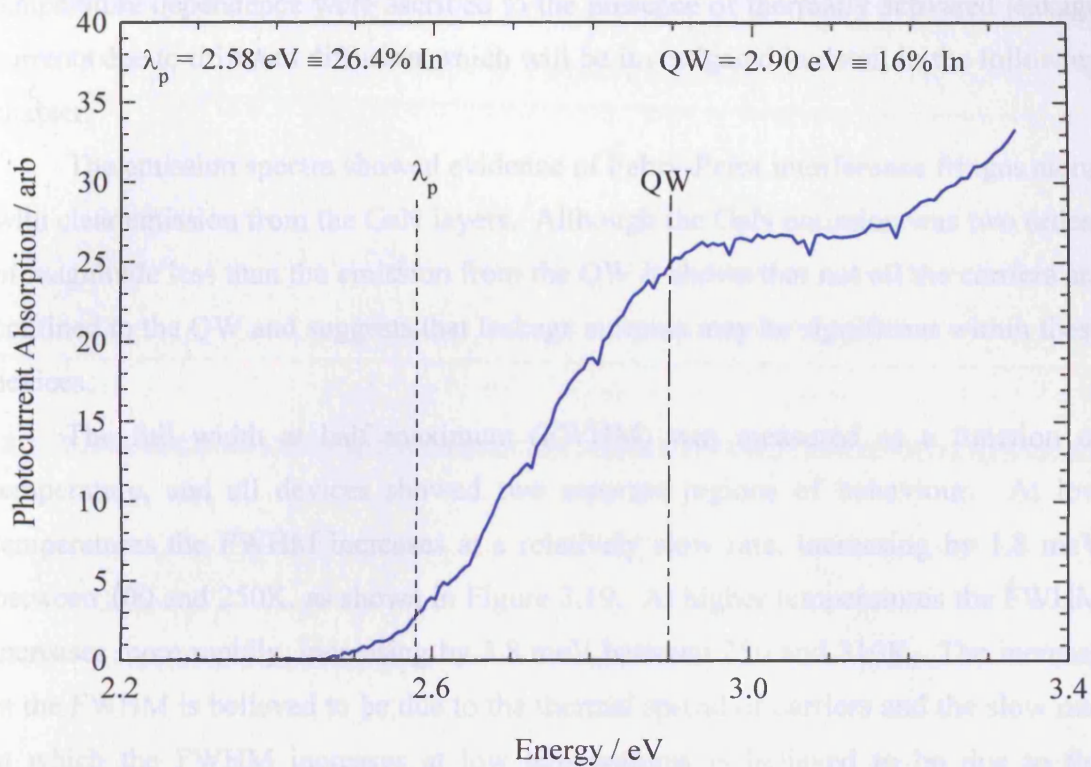
Figure 3.20 – Photocurrent absorption spectrum. The small dashed line, labelled λ_p, corresponds to the wavelength of the peak in the emission spectrum, the second dashed line (large and small dashes), labelled QW, corresponds to the position of a quantum well with 16% In (the value determined by X-ray diffraction).

Marked on Figure 3.20 is the position of the peak in the emission spectrum (small dashed lines, labelled λ_p) and the position of a $In_{0.16}Ga_{0.84}N$ QW (large and small dashed lines, labelled QW), the corresponding In compositions and bandgap energies were determined by interpolating from the binary values of In and GaN using Equation 3.4 and Equation 3.3 respectively. The presence of the absorption tail suggests that the QW is inhomogeneous, due for example to composition fluctuations or well width non-uniformity[25].

3.4 Summary

In this chapter I have investigated light-current-voltage characteristics along with the emission spectra, both as a function of current and temperature. The light current characteristics showed sub-linear behaviour at all temperatures and distinctive temperature dependence; the light output at a fixed current density initially increases

with increasing temperature, reaches a maximum value at 250K and then decreases for subsequent increases in temperature. Both the sub-linear behaviour and the temperature dependence were ascribed to the presence of thermally activated leakage currents due to drift and diffusion which will be investigated in detail in the following chapter.

The emission spectra showed evidence of Fabry-Perot interference fringes along with clear emission from the GaN layers. Although the GaN emission was two orders of magnitude less than the emission from the QW it shows that not all the carriers are confined to the QW and suggests that leakage currents may be significant within these devices.

The full width at half maximum (FWHM) was measured as a function of temperature, and all devices showed two separate regions of behaviour. At low temperatures the FWHM increases at a relatively slow rate, increasing by 1.8 meV between 100 and 250K, as shown in Figure 3.19. At higher temperatures the FWHM increases more rapidly, increasing by 3.8 meV between 250 and 310K. The increase in the FWHM is believed to be due to the thermal spread of carriers and the slow rate at which the FWHM increases at low temperatures is believed to be due to the compensating affect of the rapid increase in emission intensity seen in the experimental data.

The peak wavelength as a function of temperature was measured and fitted using the Varshni equation. It was found that a best line fit using the Varshni equation returned unrealistic parameter values as compared to the binary values of In and GaN. Using parameter values interpolated from the binaries it is impossible to obtain a fit to the experimental data using the Varshni equation if an In concentration of 16% (the value obtained by X-ray diffraction) is used, since the bandgap energy is too large. The calculated bandgap (2.96 eV) is also larger than the observed peak in the spontaneous emission, which occurs at 2.58 eV and corresponds to an indium concentration 26.4% (as interpolated from the binaries). Using an indium concentration of 26.4% a good fit to the experimental data can be achieved, suggesting the presence of localised regions in the QW due to the clustering of indium during growth.

Finally, the photocurrent absorption was measured. Above 2.90 eV, the calculated bandgap energy for an $In_{0.16}Ga_{0.84}N$ QW, the absorption spectrum flattens out, before increasing again as you move towards the bandgap of GaN. However

there is no well-defined absorption edge to the QW, rather there was an absorption tail which extended to low energies and which corresponds the peak emission, suggesting that the QW is inhomogeneous, due for example to composition fluctuations or well width non-uniformity[25] and that the radiative emission is occurring from these regions.

3.5 References

1. G.B. Ren, H.D. Summers, P. Blood, R. Perks, and D.P. Bour, *Nonradiative recombination and efficiency of InGaN quantum well light-emitting diodes.* Proc. SPIE Vol. 4283, p. 78-84, Physics and Simulation of Optoelectronic Devices IX, Yasuhiko Arakawa; Peter Blood; Marek Osinski; Eds., 2001. **Vol. 4283**.

2. K.G. Zolina, V.E. Kudryashov, A.N. Turkin, A.E. Yunovich, and S. Nakamura, *Luminescence spectra of superbright blue and green InGaN/AlGaN/GaN light-emitting diodes.* MRS Internet Journal of Nitride Semiconductor Research, 1996. **1**(1-46): p. art. no.-11.

3. I.A. Pope, P.M. Smowton, P. Blood, J.D. Thomson, M.J. Kappers, and C.J. Humphreys, *Carrier leakage in InGaN quantum well light-emitting diodes emitting at 480 nm.* Applied Physics Letters, 2003. **82**(17): p. 2755-2757.

4. J. Piprek and S. Nakamura, *Physics of high-power InGaN/GaN lasers.* IEE Proceedings-Optoelectronics, 2002. **149**(4): p. 145-151.

5. S. Hausser, G. Fuchs, A. Hangleiter, K. Streubel, and W.T. Tsang, *Auger Recombination in Bulk and Quantum-Well InGaAs.* Applied Physics Letters, 1990. **56**(10): p. 913-915.

6. G.W. 't Hooft, M.R. Leys, and H.J. Talen-v.d. Mheen, *Temperature Dependence of the Radiative Recombination Coefficient in GaAs - (Al,Ga)As Quantum Wells.* Superlattices and Microstructures, 1985. **1**(4): p. 307 - 310.

7. D. Lancefield, A. Crawford, B. Beaumont, P. Gibart, M. Heuken, and M. Di Forte-Poisson, *Temperature dependent electroluminescence in GaN and InGaN/GaN LEDs.* Materials Science and Engineering B-Solid State Materials for Advanced Technology, 2001. **82**(1-3): p. 241-244.

8. T.Y. Lin, *Converse piezoelectric effect and photoelastic effect in InGaN/GaN multiple quantum wells.* Applied Physics Letters, 2003. **82**(6): p. 880-882.

9. S. Chichibu, T. Azuhata, T. Sota, and S. Nakamura, *Spontaneous emission of localized excitons in InGaN single and multiquantum well structures.* Applied Physics Letters, 1996. **69**(27): p. 4188-4190.

10. I. Akasaki and H. Amano, *Widegap Column-III Nitride Semiconductors for UV/Blue Light- Emitting Devices.* Journal of the Electrochemical Society, 1994. **141**(8): p. 2266-2271.

11. Y. Fujiwara, H. Nishitani, H. Nakata, and T. Ohyama, *Structured Photoluminescence Spectrum in Laterally Anodized Porous Silicon.* Japanese Journal of Applied Physics Part 2-Letters, 1992. **31**(12B): p. L1763-L1766.

12. C.L. Curtis, V.V. Doan, G.M. Credo, and M.J. Sailor, *Observation of Optical Cavity Modes in Photoluminescent Porous Silicon Films.* Journal of the Electrochemical Society, 1993. **140**(12): p. 3492-3494.

13. D.C. Marra, E.S. Aydil, S.J. Joo, E. Yoon, and V.I. Srdanov, *Angle-dependent photoluminescence spectra of hydrogenated amorphous silicon thin films.* Applied Physics Letters, 2000. **77**(21): p. 3346-3348.

14. E. Hecht, *Optics.* 3rd ed. 1998, New York: Addison Wesley.

15. M.E. Lin, B.N. Sverdlov, S. Strite, H. Morkoc, and A.E. Drakin, *Refractive-Indexes of Wurtzite and Zincblende GaN.* Electronics Letters, 1993. **29**(20): p. 1759-1761.

16. W. Shan, B.D. Little, J.J. Song, Z.C. Feng, M. Schuman, and R.A. Stall, *Optical transitions in $In_xGa_{1-x}N$ alloys grown by metalorganic chemical vapor deposition.* Applied Physics Letters, 1996. **69**(22): p. 3315-3317.

17. M. Krijn, *Heterojunction Band Offsets and Effective Masses in III-V Quaternary Alloys.* Semiconductor Science and Technology, 1991. **6**(1): p. 27-31.

18. I. Vurgaftman, J.R. Meyer, and L.R. Ram-Mohan, *Band parameters for III-V compound semiconductors and their alloys.* Journal of Applied Physics, 2001. **89**(11): p. 5815-5875.

19. T. Matsuoka, H. Okamoto, M. Nakao, H. Harima, and E. Kurimoto, *Optical bandgap energy of wurtzite InN.* Applied Physics Letters, 2002. **81**(7): p. 1246-1248.

20. H.K. Cho, J.Y. Lee, J.H. Song, P.W. Yu, G.M. Yang, and C.S. Kim, *Influence of strain-induced indium clustering on characteristics of InGaN/GaN multiple*

quantum wells with high indium composition. Journal of Applied Physics, 2002. **91**(3): p. 1104-1107.

21.   Y. Narukawa, Y. Kawakami, M. Funato, S. Fujita, and S. Nakamura, *Role of self-formed InGaN quantum dots for exciton localization in the purple laser diode emitting at 420 nm.* Applied Physics Letters, 1997. **70**(8): p. 981-983.

22.   Y.H. Cho, G.H. Gainer, A.J. Fischer, J.J. Song, S. Keller, U.K. Mishra, and S.P. DenBaars, *"S-shaped" temperature-dependent emission shift and carrier dynamics in InGaN/GaN multiple quantum wells.* Applied Physics Letters, 1998. **73**(10): p. 1370-1372.

23.   W. Shan, W. Walukiewicz, E.E. Haller, B.D. Little, J.J. Song, M.D. McCluskey, N.M. Johnson, Z.C. Feng, M. Schurman, and R.A. Stall, *Optical properties of $In_xGa_{1-x}N$ alloys grown by metalorganic chemical vapor deposition.* Journal of Applied Physics, 1998. **84**(8): p. 4452-4458.

24.   S. Chichibu, T. Azuhata, T. Sota, and S. Nakamura, *Luminescences from localized states in InGaN epilayers.* Applied Physics Letters, 1997. **70**(21): p. 2822-2824.

25.   J.A. Davidson, P. Dawson, T. Wang, T. Sugahara, J.W. Orton, and S. Sakai, *Photoluminescence studies of InGaN/GaN multi-quantum wells.* Semicond. Sci. Technol., 2000. **15**(6): p. 497-505.

4 Simulation of LI Characteristics

4.1 Introduction

In chapter 3 the light current (LI) characteristics of an InGaN/GaN LED, emitting at 480nm, were presented and were found to exhibit sublinear behaviour over the entire temperature range investigated. Also a distinctive temperature dependence was noted; initially as the temperature is increased the light output at a fixed current density also increases, reaching a maximum value around 250K, then for subsequent increases in temperature the light output decreases.

It is postulated that the sublinear LI curves and their distinctive temperature dependence may be explained via thermally activated leakage currents through the p-doped layers. To test the validity of the postulate the LI characteristics will be simulated using a drift/diffusion model.

The first part of the chapter details the theory on which the model is based. This is followed by details of the parameter values and assumptions made setting up the model. Finally the simulated LI characteristics are presented and compared with the experimental results of chapter 3.

4.2 Theory Behind Model

To accurately reproduce the LI characteristics, all the current pathways illustrated in Figure 4.1 are included in the model. Electrons are injected into the device in the n-type region, from where they travel along the conduction band towards the QW. When the electrons reach the QW some fall into the well where they recombine across the bandgap, while others are thermally excited back out of the well before they have a chance to recombine. These electrons may then continue through the device to the p-contact as drift or diffusive leakage currents or they may also recombine in the GaN barrier layers.
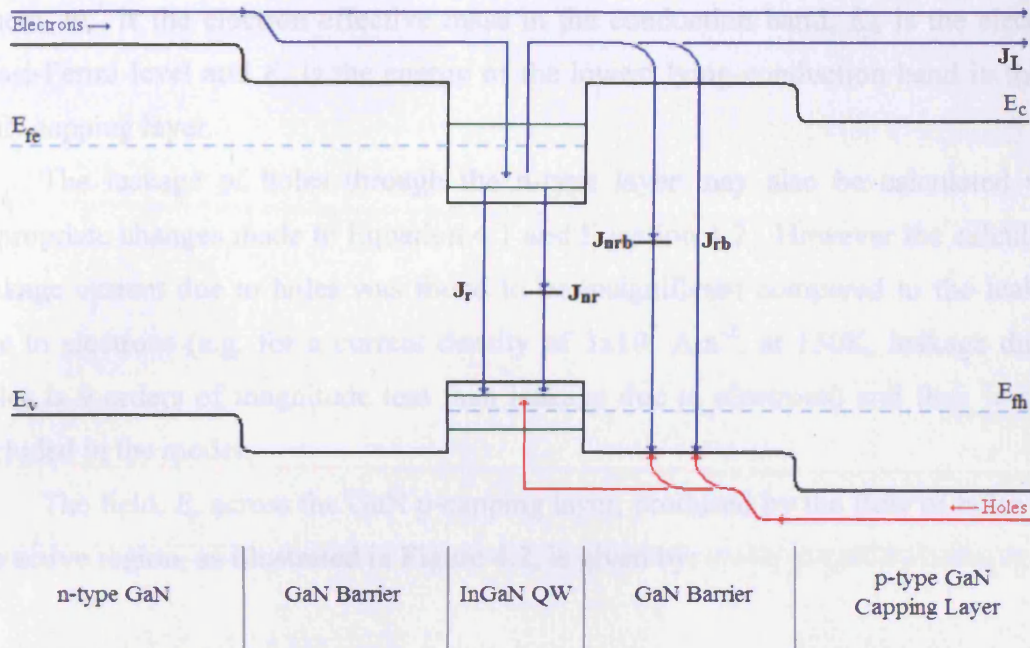
Figure 4.1 – Schematic band diagram demonstrating the current pathways included in the drift-diffusion model.

Recombination across the bandgap, which can be both radiative and non-radiative, is calculated using Equation 1.14 and Equation 1.15. The leakage current through the p-type layer, including both drift and diffusion, is calculated using Equation 4.1 below[1, 2].

$$J_L = eD_n n_c \left[\left(\frac{1}{L_n^2} + \frac{1}{4z^2} \right)^{1/2} \coth \left(\left(\frac{1}{L_n^2} + \frac{1}{4z^2} \right)^{1/2} w_c \right) + \frac{1}{2z} \right]$$

Equation 4.1

where, D_n is the diffusion coefficient ($D_n = k_B T \mu_e/e$, μ_e is the minority carrier mobility in p-type capping layer), L_n is the diffusion length ($L_n = [D_n \tau_{nrc}]^{1/2}$, τ_{nrc} is the non-radiative lifetime in the p-GaN capping layer), z is the drift coefficient ($z = k_B T/eE$, E is the field across the p-type capping layer), w_c is the width of the p-GaN capping layer and n_c is the number of electrons, per unit volume, at the edge of the p-GaN capping layer. Assuming a Boltzman distribution this is given by

$$n_c = 2 \left(\frac{m_e^* k_B T}{2\pi \eta^2} \right)^{3/2} \exp \left(\frac{E_{fe} - E_c}{k_B T} \right)$$

Equation 4.2

where, m_e^* is the electron effective mass in the conduction band, E_{fe} is the electron quasi-Fermi level and E_c is the energy of the lowest lying conduction band in the p-GaN capping layer.

The leakage of holes through the n-type layer may also be calculated with appropriate changes made to Equation 4.1 and Equation 4.2. However the calculated leakage current due to holes was found to be insignificant compared to the leakage due to electrons (e.g. for a current density of 3×10^7 Am^{-2}, at 150K, leakage due to holes is 9 orders of magnitude less than leakage due to electrons) and thus was not included in the model.

The field, E, across the GaN p-capping layer, produced by the flow of holes into the active region, as illustrated in Figure 4.2, is given by:

$$E = \frac{J_{nr} + J_r + J_{nrb} + J_{rb}}{\sigma(T)}$$

Equation 4.3

where, $\sigma(T)$ is the conductivity, J_{nr} and J_r are the non-radiative and radiative recombination current densities in the quantum well (QW) and J_{nrb} and J_{rb} are the non-radiative and radiative recombination current densities in the barrier.
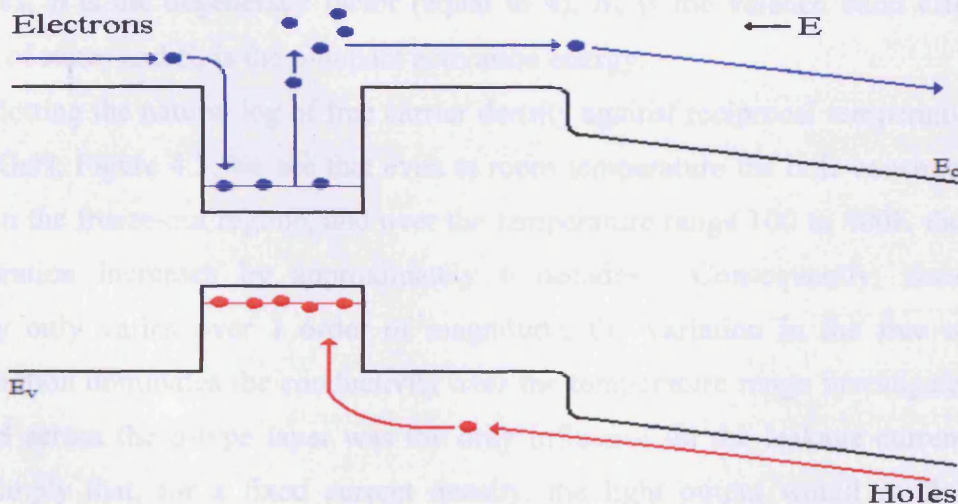

Figure 4.2 – Schematic potential energy band diagram

For a fixed current density the field across the p-type capping layer is controlled by the conductivity and from Equation 4.3, an increase in the conductivity will lead to a decrease in this field. Such a decrease in the field responsible for pulling the electrons away from the QW results in a decrease in the leakage current,

consequently, at a fixed current density, there will be a greater number of electrons in the region of the QW which are able to recombine radiatively and the light output intensity will increase. Similarly a decrease in the conductivity, for a fixed current density, will lead to a decrease in the light output intensity. The temperature dependent conductivity $\sigma(T)$, of the p-type capping layer, is given by

$$\sigma(T) = p(T)\mu_p(T)e$$

Equation 4.4

where, $\mu_p(T)$ is the majority carrier mobility and $p(T)$ is the free carrier concentration which may be expressed as[3]

$$p^2 + p(N_d + N_v') - (N_a - N_d)N_v' = 0$$

Equation 4.5

$$N_v' = \beta N_v \exp\left(-\frac{E_a}{k_B T}\right)$$

Equation 4.6

where, p is the free carrier density, N_d is the number of donors, N_a is the number of acceptors, β is the degeneracy factor (equal to 4), N_v is the valence band effective density of states and E_a is the p-dopant activation energy.

Plotting the natural log of free carrier density against reciprocal temperature for p-type GaN, Figure 4.3, we see that even at room temperature the hole concentration is still in the freeze-out regime, and over the temperature range 100 to 400K the hole concentration increases by approximately 6 decades. Consequently, since the mobility only varies over 1 order of magnitude, the variation in the free carrier concentration dominates the conductivity over the temperature range investigated. If the field across the p-type layer was the only influence on the leakage current this would imply that, for a fixed current density, the light output would continue to increase until it reached a constant value, either when the leakage current had fallen to zero or the hole concentration had reached its exhaustion value.
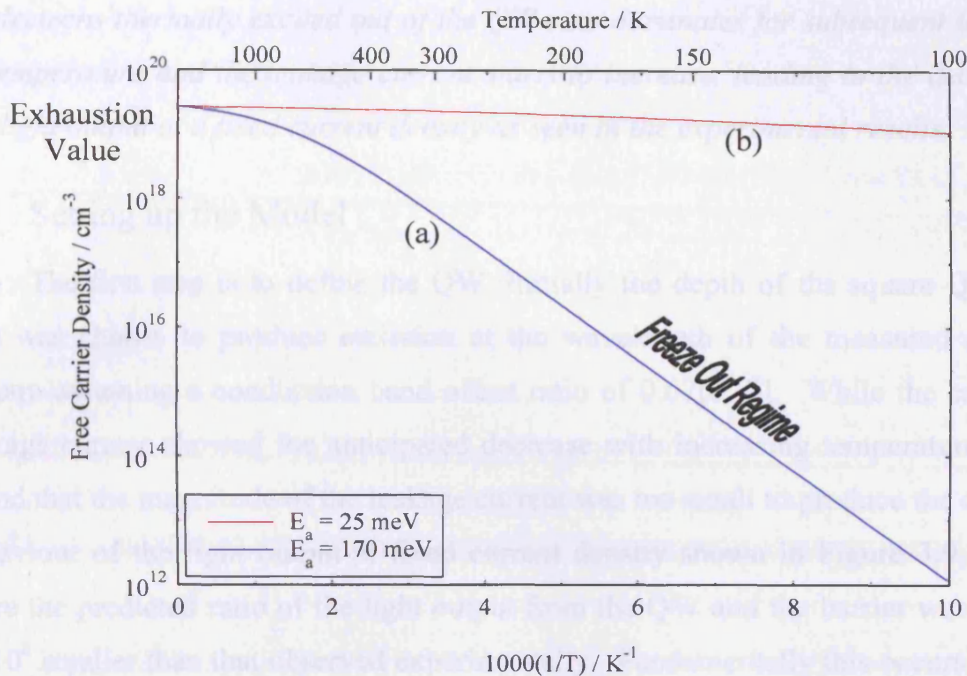
Figure 4.3 – Semilogarithmic plots of free carrier density against reciprocal temperature for Mg doped GaN with an a) activation energy (E_a) of 170meV[4] [reported value], and b) activation energy of 25meV [equivalent to Zn in GaInP[5]].

The fact that the experimental light output at a fixed current density reaches a maximum value at 250K and the decreases for subsequent increases in temperature indicates that there is a second process at work which tries to counteract the reduction of the leakage current due to the decrease in the field across the p-type layer. This process is the thermal activation of electrons out of the QW, which increases exponentially with temperature, since an increase in the number of electrons able to leak across the p-type layer will lead to an increase in the leakage current.

The postulate describing the distinctive temperature dependent behaviour may thus be explained as follows; *at low temperatures there is a large leakage current due to the low conductivity. As the temperature of the LED is increased the conductivity increases and the number of electrons thermally excited out of the QW also increases. Initially the conductivity increases at a rate greater than the number of electrons thermally excited out of the QW and the leakage current decreases, leading to an increase in the light output at a fixed current density. At some critical temperature, Tc, the decreases in the leakage current due to the increase in the conductivity is balanced by the increase in the leakage current due the thermal excitation of electrons out of the QW, this corresponds to the temperature at which the maximum light output for a fixed current density is obtained. The rate of increase in the number*

of electrons thermally excited out of the QW now dominates for subsequent increases in temperature and the leakage current starts to increase, leading to the decrease in the light output at a fixed current density as seen in the experimental results.

4.3 Setting up the Model

The first step is to define the QW. Initially the depth of the square QW (0.57 eV) was chosen to produce emission at the wavelength of the measured emission spectra assuming a conduction band offset ratio of 0.67[6, 7]. While the calculated leakage current showed the anticipated decrease with increasing temperature, it was found that the magnitude of the leakage current was too small to produce the observed behaviour of the light output at fixed current density shown in Figure 3.9, furthermore the predicted ratio of the light output from the QW and the barrier was a factor of 10^6 smaller than that observed experimentally. Fundamentally this occurs because the electron quasi-Fermi level is too far below the conduction band of the p-GaN capping layer. Simply increasing the quasi-Fermi energy by increasing the sub-band separation of the QW will produce emission at too high a photon energy. From this it was concluded that, using reasonable parameter values, the computer simulation could not reproduce the behaviour of the LI curves and the emission spectra using a step density of states function, characteristic of a uniform quantum well.

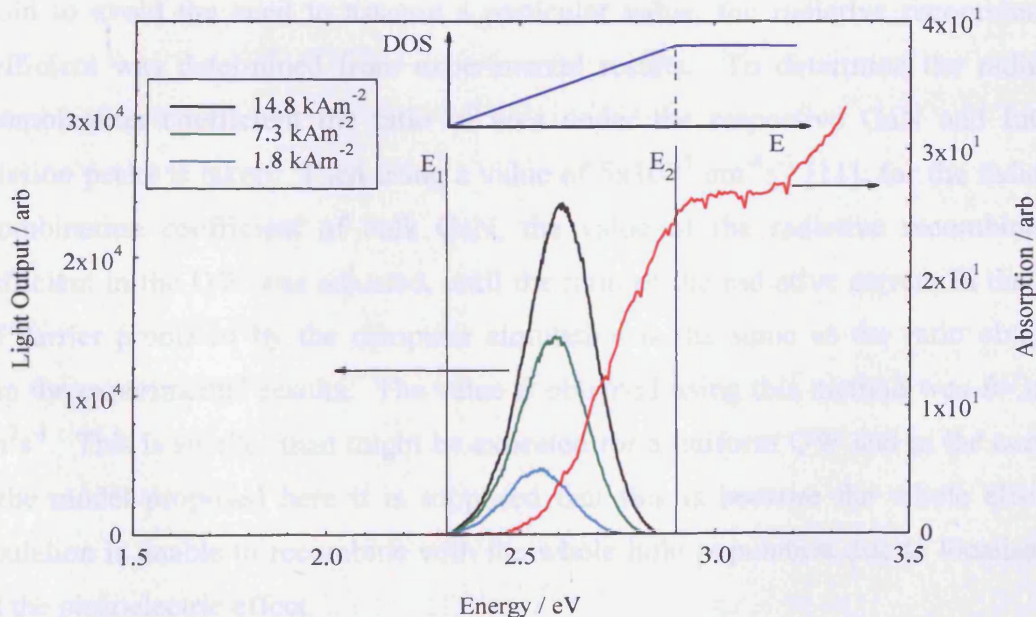
Figure 4.4 – Top emission spectra at 1.8, 7.3 and 14.8 kAm-2 (left axis) and edge absorption spectrum (right axis), both at room temperature. Inset shows a schematic diagram of the triangular density of states used in the computer simulation.

Figure 4.4 combines Figure 3.11 and Figure 3.20 and shows the LED photocurrent absorption spectrum along with several emission spectra. The absorption spectrum shows no well-defined absorption edge and comparison with the emission spectra shows, that at all currents, the LED emission occurs at the low energy edge in the absorption tail. As discussed in chapter 3 this suggests that the quantum wells are inhomogeneous, due for example to composition fluctuations, or well width non-uniformity[8] and that the emission occurs from localised regions where the sub-band separation is smallest[9, 10].

To take account of this, the density of states was modelled using a triangular function, as shown by the inset in Figure 4.4, which extends from the lowest photon emission energy (E_1 in Figure 4.4) and which becomes constant at the value for a single sub-band where the absorption spectrum flattens out (E_2 in Figure 4.4). The result is a reduction in the density of states (DOS) at the band-edge, as compared with a uniform well, hence the quasi-Fermi energy for a corresponding carrier density is increased. By using the experimental absorption and emission spectra to define the DOS function the need to assume a particular mechanism for the localisation, which leads to the tail states, is avoided.

The use of a triangular DOS and the presence of piezoelectric fields raise questions over the appropriate value for the radiative recombination coefficient (B). Again to avoid the need to assume a particular value, the radiative recombination coefficient was determined from experimental results. To determine the radiative recombination coefficient the ratio of area under the respective GaN and InGaN emission peaks is taken. Then using a value of 5×10^{-11} cm^{-3}s^{-1} [11], for the radiative recombination coefficient of bulk GaN, the value of the radiative recombination coefficient in the QW was adjusted, until the ratio of the radiative current in the QW and barrier produced by the computer simulation is the same as the ratio obtained from the experimental results. The value B obtained using this method was $B=3 \times 10^{-8}$cm^{2}s^{-1}. This is smaller than might be expected for a uniform QW and in the context of the model proposed here it is supposed that this is because the whole electron population is unable to recombine with the whole hole population due to localisation and the piezoelectric effect.

Before the individual current components were calculated the number of electrons and holes in the different regions of the structure were determined. This

was done assuming the electrons and holes, across both the QWs and barriers, are individually in quasi-equilibrium and specified by quasi-Fermi levels. Charge neutrality, across the QWs and barriers, was also assumed and was used to determine the positions of the electron and hole quasi-Fermi levels for a given Fermi level separation.

An initial guess of the electron quasi-Fermi level was made and number of electrons in the QW and barrier were calculated using the equations below and the appropriate layer dimensions.

$$n_{QW} = \sum_i \frac{m_e^* k_B T}{\pi \eta^2} \log\left[1 + \exp\left(\frac{E_{fe} - E_i}{k_B T}\right)\right] \quad (m^{-2})$$

Equation 4.7

$$n_{Barrier} = n_c \exp\left(\frac{E_{fe} - E_B}{k_B T}\right) \quad (m^{-3})$$

Equation 4.8

where, E_i is the energy of a ith sub-band energy level in the QW and E_B is the energy of the conduction band in the barrier. Similar equations were used to determine the number of holes for the corresponding hole quasi-Fermi level. The number of electron and holes were then compared and the value of the electron quasi-Fermi level was decreased/increased and calculation repeated. This iterative process was repeated until the total number of electrons equals the number of total number holes, across the QWs and the barriers, at which point charge neutrality is enforced.

After the energies of the electron and hole quasi-Fermi levels (and correspondingly the electron and hole concentrations in the QWs and the barriers) have been determined the individual current components, illustrated in Figure 4.1, were calculated. The radiative (J_r) and non-radiative current densities in the QWs (J_{nr}) and barriers (J_{nrb}) were calculated using the equations Equation 4.9 and Equation 4.10 below and the leakage current density was calculated using Equation 4.4.

$$J_r = \frac{eR_r}{A} \qquad J_{nr} = \frac{n_{QW} e}{\tau_{nr}}$$

Equation 4.9

$$J_{nrb} = \frac{n_{Barrier}\, e w_b}{\tau_{nrb}}$$

where, e is the electronic charge, R_r is the radiative recombination rate calculated using Equation 1.14, A is the area of the device, n_{QW} is the total number of carriers in the QW per meter squared, τ_{nr} is the non-radiative lifetime, $n_{Barrier}$ is the number of carriers in the barrier per meter cubed, w_b is the barrier width and τ_{nrb} is the non radiative lifetime in the barrier.

The individual current density components were then summed to give the total current density (J_T), which was plotted against R_r. This gives the total current density and light output for a given Fermi level separation, to obtain a complete LI curve to process was repeated for incremental increases in the Fermi level separation. The iterative process followed in the simulation is summarised in the flow diagram of Figure 4.5.
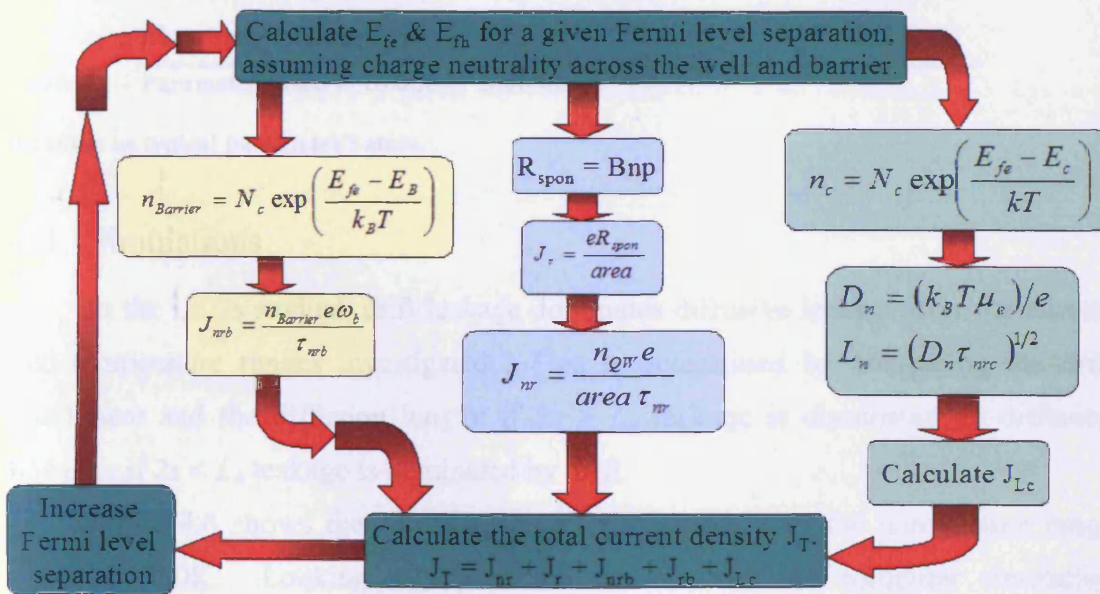

Figure 4.5 – Flow diagram illustrating the iterative procedure of the computer simulation.

Table 4.1 lists the parameters used in the computer simulation, the majority carrier mobility, $\mu_p(T)$, was taken from the experimental results of Gotz et al. [12] with the room temperature value equal to 6.1 cm^2/Vs.

Parameter	Symbol	Value	Reference
Electron mass	m_e	$0.2\,m_o$	[13]
Heavy hole mass	m_{hh}	$1.76\,m_o$	[14]
Light hole mass	m_{lh}	$1.76\,m_o$	[14]
Split off mass	m_{so}	$0.17\,m_o$	[15]
Non-radiative liftime			
in QW	τ_{nr}	30 ns	Fitting parameter
in Barrier	τ_{nrb}	0.5 ns	a
in p-GaN	τ_{nrc}	0.5 ns	a
GaN bandgap	Eg	3.42 eV	a
Valence band offset ratio		0.67	[6, 7]
Minority electron mobility	μ_e	$900\ cm^2/Vs$	a
Number of donors	N_D	$3 \times 10^{18}\ cm^{-3}$	a
Number of acceptors	N_A	$6 \times 10^{18}\ cm^{-3}$	a
Mg activation energy	E_a	170 meV	[4]

Table 4.1 – Parameters used in computer simulation.

a **chosen as typical parameter values.**

4.4 Simulations

In the LEDs studied, drift leakage dominates diffusive leakage over the current and temperature ranges investigated. This is determined by comparing the drift coefficient and the diffusion length; if $2z > L_n$ leakage is dominated by diffusion however if $2z < L_n$ leakage is dominated by drift.

Figure 4.6 shows the simulated LI characteristics over the temperature range 150K to 350K. Looking at Figure 4.6 we can see the computer simulation successfully reproduces the experimental sub-linear behaviour over the whole temperature range. The only variable used as a fitting parameter is the non-radiative lifetime in the QW. The value of 30ns used in the simulation was chosen to provide a better fit to the experimental results at low current densities.
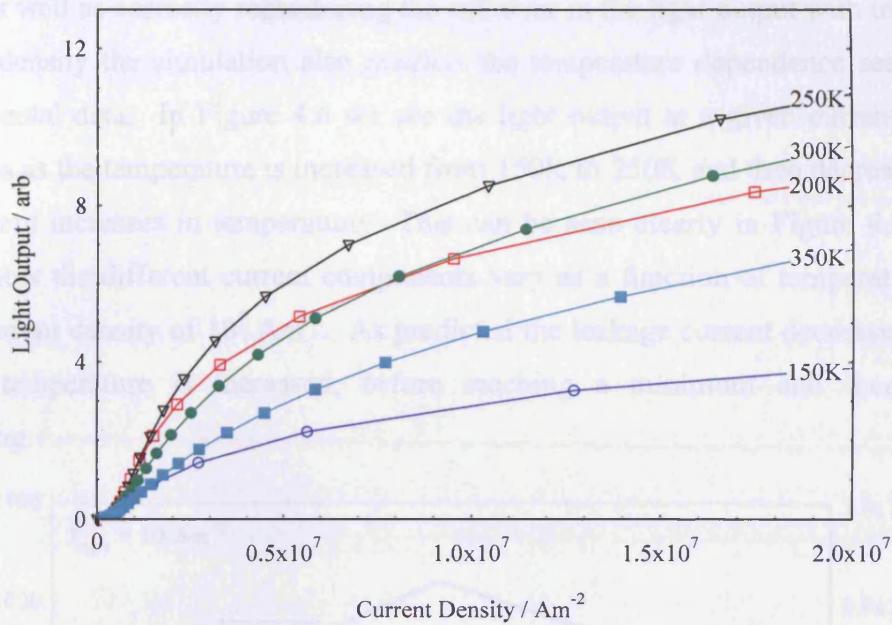
Figure 4.6 – Simulated LI characteristics over the temperature range 150K to 350K.

Direct comparison between the simulated and experimental results yields good agreement, as seen in Figure 4.7. Since the light output is in arbitrary units the curves have all been normalised to one at $1 \times 10^7 \text{Am}^{-2}$ to allow easer comparison. The two graphs shown in Figure 4.7 show good agreement between simulated and experimental results, where the same simulation parameters are used for each curve.

Figure 4.7 – Direct comparison between the experimental (blue) and simulated (red) LI characteristics at a) 250K and b) 300K.

As well as correctly reproducing the roll over in the light output with increasing current density the simulation also predicts the temperature dependence seen in the experimental data. In Figure 4.6 we see the light output at a given current density increases as the temperature is increased from 150K to 250K and then decreases from subsequent increases in temperature. This can be seen clearly in Figure 4.8, which shows how 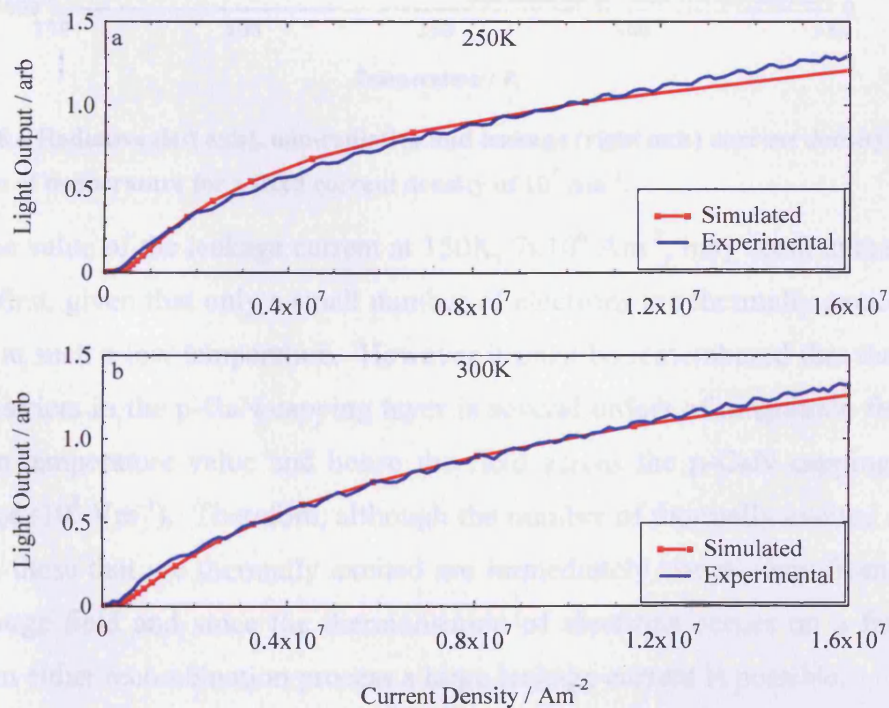the different current components vary as a function of temperature for a fixed current density of 10^7 Am^{-2}. As predicted the leakage current decreases rapidly as the temperature is increased, before reaching a minimum and then slowly increasing.
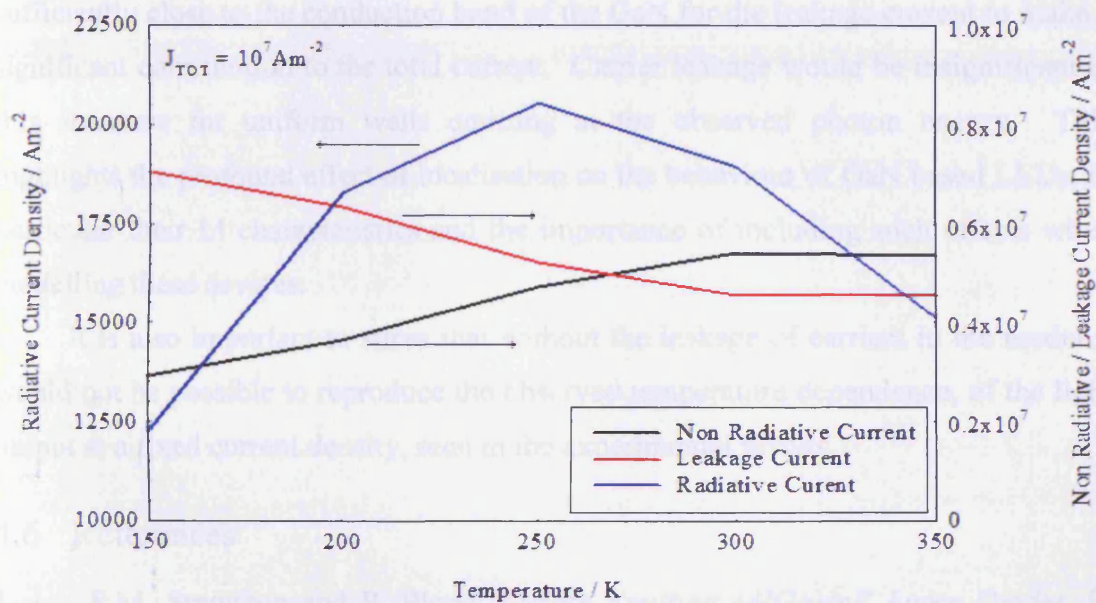
Figure 4.8 – Radiative (left axis), non-radiative and leakage (right axis) current density plotted as a function of temperature for a fixed current density of 10^7 Am^{-2}.

The value of the leakage current at 150K, 7×10^6 Am^{-2}, may seem unrealistically large at first, given that only a small number of electrons are thermally excited out of the QW at such a low temperature. However it must be remembered that the number of free carriers in the p-GaN capping layer is several orders of magnitude fewer than the room temperature value and hence the field across the p-GaN capping layer is very large (10^8 Vm^{-1}). Therefore, although the number of thermally excited electrons is small, those that are thermally excited are immediately swept away from the QW by the large field and since the thermalisation of electrons occurs on a faster time scale than either recombination process a large leakage current is possible.

4.5 Summary

In conclusion, the sub-linear LI characteristics and the temperature dependence of the light output at a fixed current density can be explained by the influence of the large acceptor ionisation energy on electron leakage by drift through the p-GaN cap layer. However, it is only possible to achieve detailed agreement with experimental LI data and emission spectra by using a non-square density of states function, characteristic of an inhomogeneous quantum well. This has the effect of giving emission at the observed wavelength while placing the quasi-Fermi energy sufficiently close to the conduction band of the GaN for the leakage current to make a significant contribution to the total current. Carrier leakage would be insignificant in this structure for uniform wells emitting at the observed photon energy. This highlights the profound effect of localisation on the behaviour of GaN based LEDs, in particular their LI characteristics and the importance of including such effects when modelling these devices.

It is also important to stress that without the leakage of carriers in the model it would not be possible to reproduce the observed temperature dependence, of the light output at a fixed current density, seen in the experimental results.

4.6 References

1. P.M. Smowton and P. Blood, *Visible Emitting (AlGa)InP Laser Diodes*, in *Strained Quantum Wells and Their Applications*, M.O. Manesreh, Editor. 1997, Gordon and Breach: New York.

2. D.P. Bour, D.W. Treat, R.L. Thornton, R.S. Geels, and D.F. Welch, *Drift Leakage Current in AlGaInP Quantum-Well Lasers*. IEEE Journal of Quantum Electronics, 1993. **29**(5): p. 1337-1343.

3. P. Blood and J.W. Orton, *The electrical Characterisation of Semiconductors: Majority carriers and electron states*. 1992, London: Academic Press.

4. W. Gotz, N.M. Johnson, J. Walker, D.P. Bour, and R.A. Street, *Activation of acceptors in Mg-doped GaN grown by metalorganic chemical vapor deposition*. Applied Physics Letters, 1996. **68**(5): p. 667-669.

5. M. Honda, M. Ikeda, Y. Mori, K. Kaneko, and N. Watanabe, *The Energy-Levels of Zn and Se in $(Al_xGa_{1-x})_{0.52}In_{0.48}P$*. Japanese Journal of Applied Physics Part 2-Letters, 1985. **24**(3): p. L187-L189.

6. W.W. Chow, A.F. Wright, and J.S. Nelson, *Theoretical study of room temperature optical gain in GaN strained quantum wells.* Applied Physics Letters, 1996. **68**(3): p. 296-298.

7. S.H. Wei and A. Zunger, *Valence band splittings and band offsets of AlN, GaN, and InN.* Applied Physics Letters, 1996. **69**(18): p. 2719-2721.

8. J.A. Davidson, P. Dawson, T. Wang, T. Sugahara, J.W. Orton, and S. Sakai, *Photoluminescence studies of InGaN/GaN multi-quantum wells.* Semicond. Sci. Technol., 2000. **15**(6): p. 497-505.

9. H.K. Cho, J.Y. Lee, J.H. Song, P.W. Yu, G.M. Yang, and C.S. Kim, *Influence of strain-induced indium clustering on characteristics of InGaN/GaN multiple quantum wells with high indium composition.* Journal of Applied Physics, 2002. **91**(3): p. 1104-1107.

10. Y. Narukawa, Y. Kawakami, M. Funato, S. Fujita, and S. Nakamura, *Role of self-formed InGaN quantum dots for exciton localization in the purple laser diode emitting at 420 nm.* Applied Physics Letters, 1997. **70**(8): p. 981-983.

11. G.B. Ren, H.D. Summers, P. Blood, R. Perks, and D.P. Bour, *Nonradiative recombination and efficiency of InGaN quantum well light-emitting diodes.* Proc. SPIE Vol. 4283, p. 78-84, Physics and Simulation of Optoelectronic Devices IX, Yasuhiko Arakawa; Peter Blood; Marek Osinski; Eds., 2001. **Vol. 4283**.

12. W. Gotz and N.M. Johnson, *Characterization of Dopants and Deep Level Defects*, in *Gallium Nitride (GaN) II*, J.I. Pankove and T.D. Moustakas, Editors. 1998, Academic: New York.

13. I. Vurgaftman, J.R. Meyer, and L.R. Ram-Mohan, *Band parameters for III-V compound semiconductors and their alloys.* Journal of Applied Physics, 2001. **89**(11): p. 5815-5875.

14. M. Suzuki, T. Uenoyama, and A. Yanase, *First-principles calculations of effective-mass parameters of AlN and GaN.* Physical Review B, 1995. **52**(11): p. 8132-8139.

15. C. Wetzel, S. Kamiyama, H. Amano, and I. Akasaki, *Optical absorption in polarized $Ga_{1-x}In_xN$/GaN quantum wells.* Japanese Journal of Applied Physics Part 1-Regular Papers Short Notes & Review Papers, 2002. **41**(1): p. 11-14.

5 Influence of Anneal Temperature

5.1 Introduction

In the previous chapter (chapter 4) it was shown that the sub-linear LI curves could be caused by thermally activated leakage currents, as could the temperature dependence of the light output at a fixed current density, seen in the experimental results of chapter 3. It was also shown that it is both the E-field in the p-capping layer and the number of electrons thermally excited out of the QW which determines the leakage current and hence Tc (the temperature at which there is a maximum in the light output for a fixed current density). Similar temperature dependent behaviour has also been observed in the literature[1], however they report different values for Tc (Tc = 193K[1]). In this chapter I will investigate the possible causes of the variation of the values of Tc.

At the beginning of the chapter, experimental results for four sets of LEDs (all fabricated from the same wafer) with different post growth anneal temperatures used to activate the p-type dopants, are presented. As discussed in chapter 1, the different anneal temperatures (700, 750, 850 and 900°C) mean the concentration of activated Mg acceptors will be different for each set of LEDs, thus allowing an investigation into the effect anneal temperature and Mg concentration has on internal leakage currents and light output. Understanding the key parameters affecting the internal leakage current is important since it enables the design of more efficient LEDs.

The second part of the chapter is devoted to modelling the experimental results in the same manner as outlined in chapter 4, that is the use of a drift-diffusion model to reproduce the shape of the LI characteristics and the trend seen in the light output at a fixed current density. To simulate the effect of the different anneal temperatures the simulations were run with different acceptor densities and p-type mobility based on the experimental results of Gotz et al, [2].

5.2 Experimental Results

Experiments were performed on InGaN/GaN LEDs grown and fabricated at Sheffield University; structure details are given in Table 5.1. The wafer, from which all the devices were fabricated, were cleaved into four pieces and different anneal temperatures used to activate the p-layers of the corresponding pieces. The anneal temperatures used were 700, 750, 850 and 900°C and were achieved using a rapid thermal anneallar (RTA). Each piece of wafer was placed in the RTA for 20 minutes at the specified temperature.

Repeats	Thickness / A	Material	(x)
1	3000	Mg++ GaN	
125	25	Mg GaN	
125	25	Mg AlGaN	0.17
1	1500	Mg GaN	
1	200	Mg AlGaN	0.3
10	75	GaN	
10	25	InGaN	0.1
1	1500	Si GaN	
125	26	Si GaN	
125	26	Si AlGaN	0.17
1	20000	Si++ GaN	
10	40000	si GaN	
10	20000	GaN	
1	300	Nucleation	

640250 A = total thickness

Table 5.1 – Table showing the structure of the devices. Highlighted cells indicate layers modelled in section 5.3.1.

Absorption and emission spectra were recorded as described in sections 2 and 3.2.2 respectively. However the short emission wavelength (420nm) of the devices meant the IVL characteristics could not be measured using the apparatus described in section 3.2.1 since this is beyond the range of the silicon detector.

To obtain the IVL characteristics, the emission spectra were recorded (as described in section 3.2.2, using the ICCD camera as the detector) at 1V intervals from 0 to 20V. The area underneath the emission spectra was then integrated to obtain the total light output at a given voltage; the current at this voltage was also recorded. This allows the IVL characteristics at a given temperature to be plotted. The process was then repeated for different temperatures.
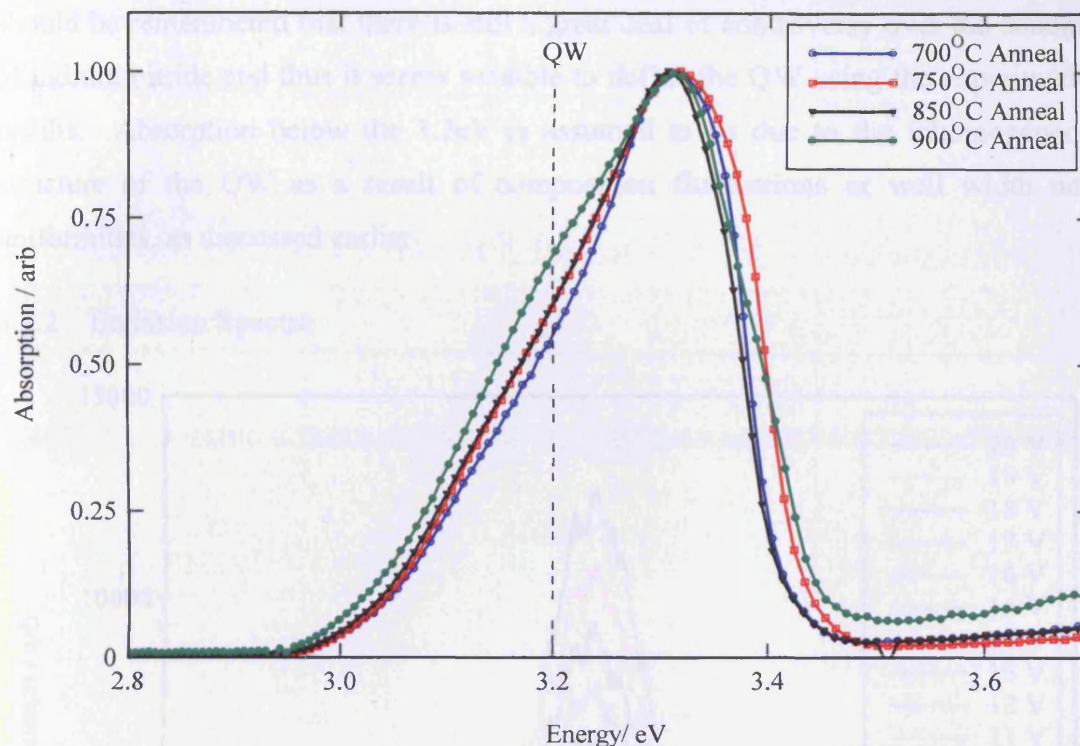
5.2.1 Absorption Spectra

Figure 5.1 – Photocurrent absorption spectra for samples annealed at 700, 750,850 and 900°C, typical of all absorption spectra. The dashed line indicates the position of the QW calculated using the measured indium concentration.

The absorption spectra of the four samples annealed at different temperatures are illustrated in Figure 5.1 and are typical of all the absorption spectra recorded. The fact that all the absorption spectra for the different anneal temperatures are similar indicates that the post growth annealing has not affected the band structure of the devices in any way.

Examining Figure 5.1 we see there is no well-defined absorption edge nor is there a clear fluctuation in the absorption spectra to show the location of the QW, unlike the case for the Cambridge LEDs where the QW could clearly be seen. Rather, the absorption tail from the GaN layers appear to merge into the absorption tail of the QW. This might be expected since the In composition is lower than in the Cambridge devices (0.1 as opposed to 0.16), thus the QW will be closer in energy to the GaN layers and so may not be distinguishable. There is however, a small bump on the low energy side of the absorption spectrum at 3.2eV (Labelled QW in Figure 5.1). This bump is taken to be evidence of the QW and it is assumed to be the energy of a single

sub-band within the QW. This is slightly different to the value calculated by interpolating from the binary values and equates to an In concentration of 6%. It should be remembered that there is still a great deal of controversy over the bandgap of indium nitride and thus it seems sensible to define the QW using the experimental results. Absorption below the 3.2eV is assumed to be due to the inhomogeneous structure of the QW as a result of composition fluctuations or well width non-uniformities, as discussed earlier.

5.2.2 Emission Spectra
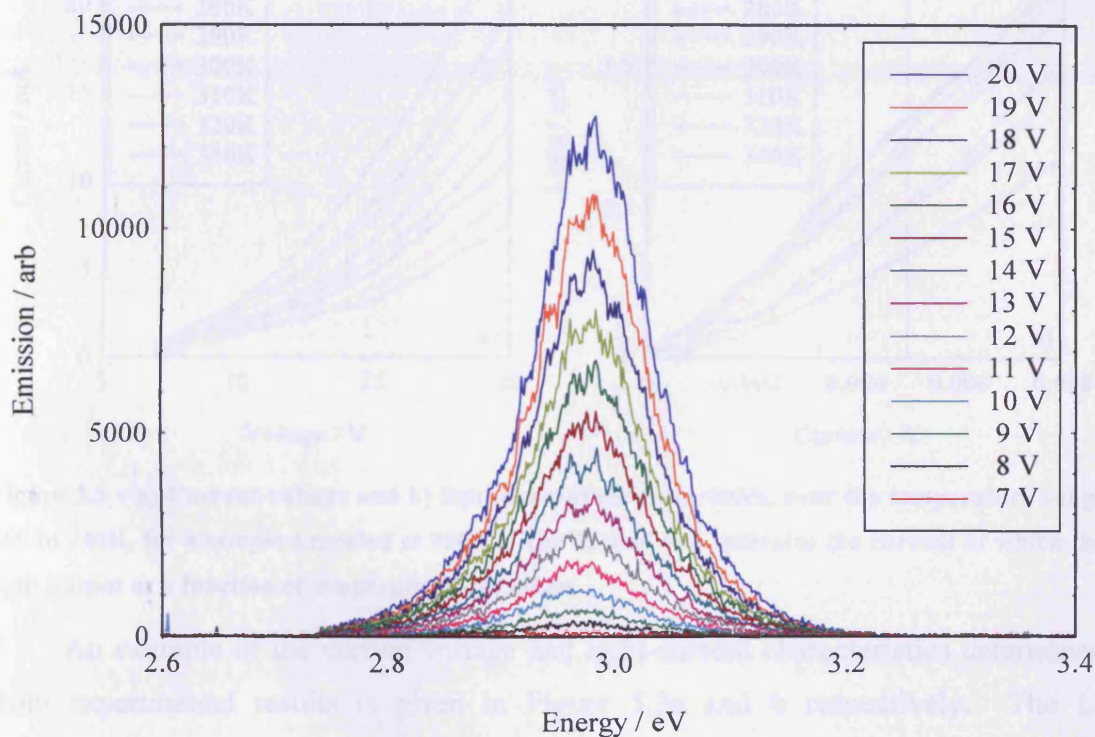
Figure 5.2 – Emission spectra for a device annealed at 900°C, typical of all emission spectra.

Emission spectra for a device annealed at 900°C are shown in Figure 5.2. The spectra were recorded at 300K over the voltage range 7 to 20V. The area under each spectrum was integrated to obtain the light output. The subsequent LI characteristics are shown in Figure 5.3a & b. There was no significant difference between the emission spectra illustrated in Figure 5.2 and those of all the devices, with the peak wavelength approximately equal across all anneal temperatures. Again this indicates that annealing has not affected the band structure or the composition of the QW.

Closer inspection of Figure 5.2 reveals that emission extends down to a photon energy of 2.73eV, 0.19eV below the low energy edge of the absorption spectrum in

Figure 5.1. This was also seen in the results of chapter 3 and was attributed to emission occurring from localised regions where the sub-band separation is smallest[3, 4], due for example to composition fluctuations, or well width non-uniformity[5].
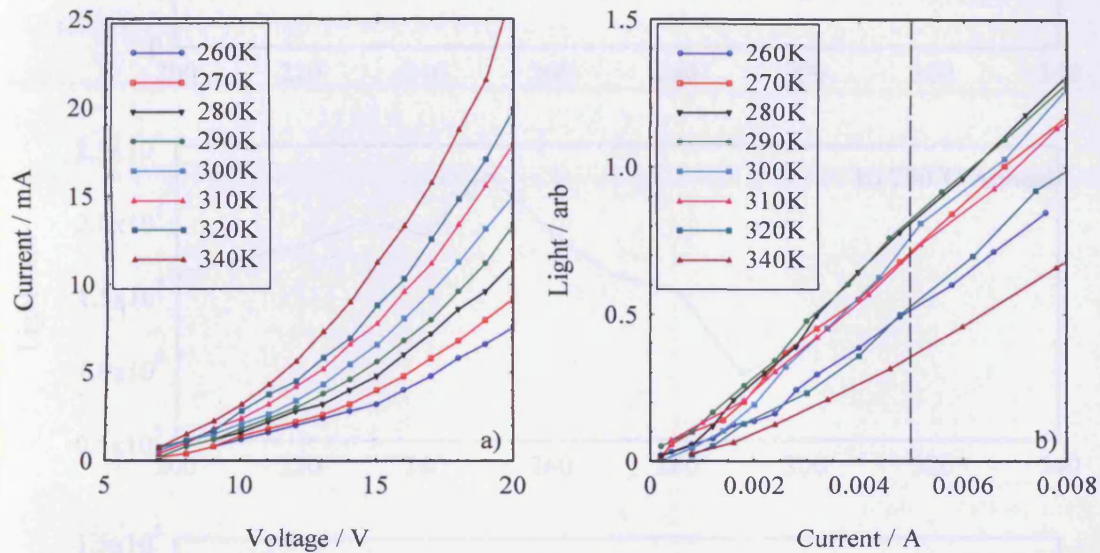
5.2.3   IVL Characteristics

Figure 5.3 – a) Current-voltage and b) light-current characteristics, over the temperature range 260 to 340K, for a sample annealed at 900°C. The dashed line indicates the current at which the light output as a function of temperature was taken.

An example of the current-voltage and light-current characteristics determined from experimental results is given in Figure 5.3a and b respectively.   The LI characteristics do not exhibit the sub-linear behaviour seen in Figure 3.9, rather they appear to be linear to slightly super-linear.   The fact that the devices do not have sub-linear LI characteristics does not mean there are no leakage currents present within the device, nor that leakage is not a significant process.   It must be remembered that the LI curves represent the balance between all the recombination processes.   While a linear LI curve is a characteristic of a perfect LED a linear LI curve may also be achieved if the leakage current balances out the other non-radiative current process. It seems highly improbable we are dealing with a perfect LED, therefore the linear LI characteristics are an indication of a leakage current balancing out the non-radiative current.

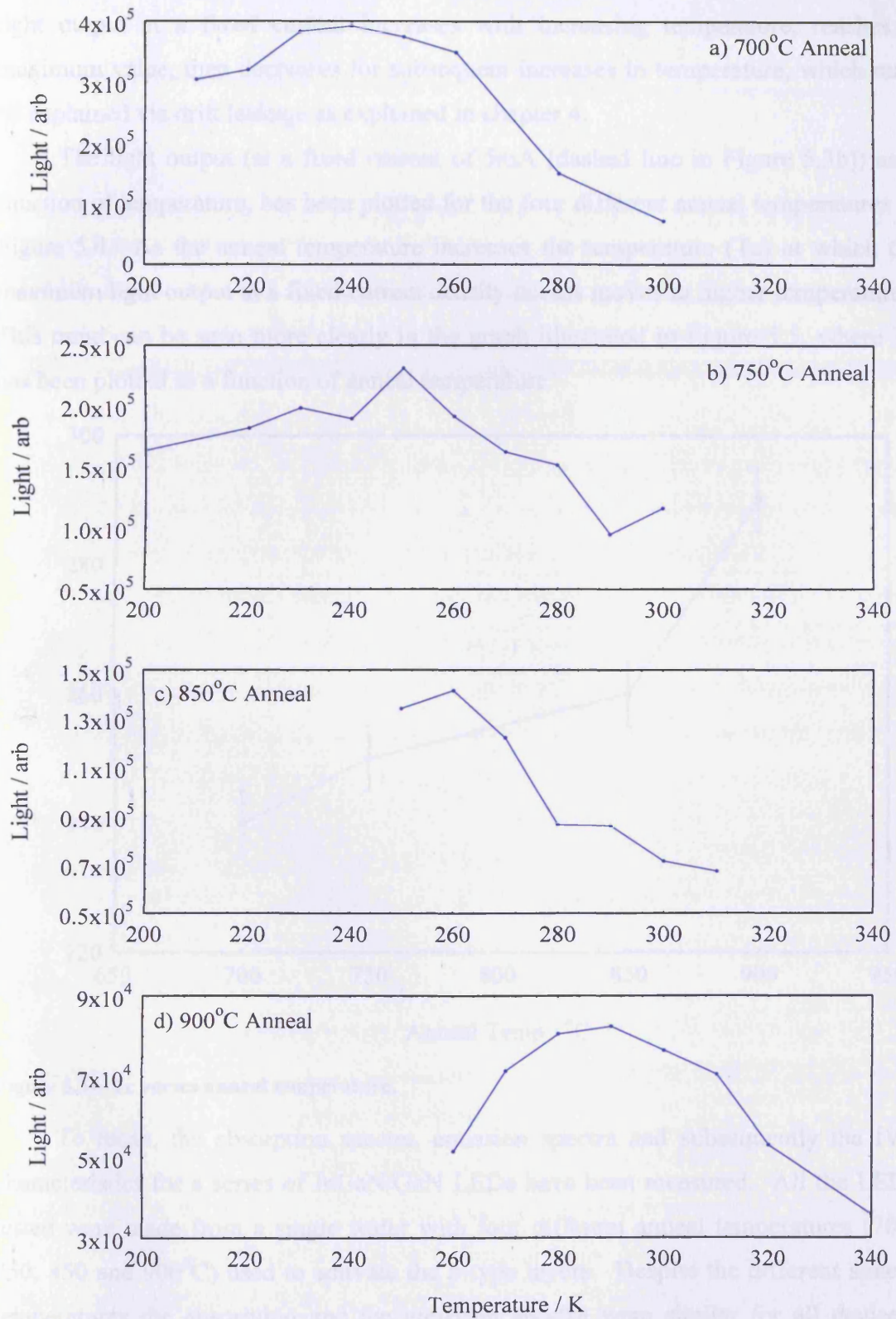### 5.2.4 Light Output at a fixed Current

Figure 5.4 – Light output (at a fixed current of 5mA) as a function of temperature for devices annealed at a) 700°C b) 750°C c) 850°C and d) 900°C.

Further evidence for the presence of a significant leakage current can be seen in the temperature dependence of the LI characteristics, Figure 5.3b & Figure 5.4. The light output at a fixed current increases with increasing temperature, reaches a maximum value, then decreases for subsequent increases in temperature, which may be explained via drift leakage as explained in chapter 4.

The light output (at a fixed current of 5mA [dashed line in Figure 5.3b]) as a function of temperature, has been plotted for the four different anneal temperatures in Figure 5.4. As the anneal temperature increases the temperature (Tc) at which the maximum light output at a fixed current density occurs moves to higher temperatures. This trend can be seen more clearly in the graph illustrated in Figure 5.5, where Tc has been plotted as a function of anneal temperature.
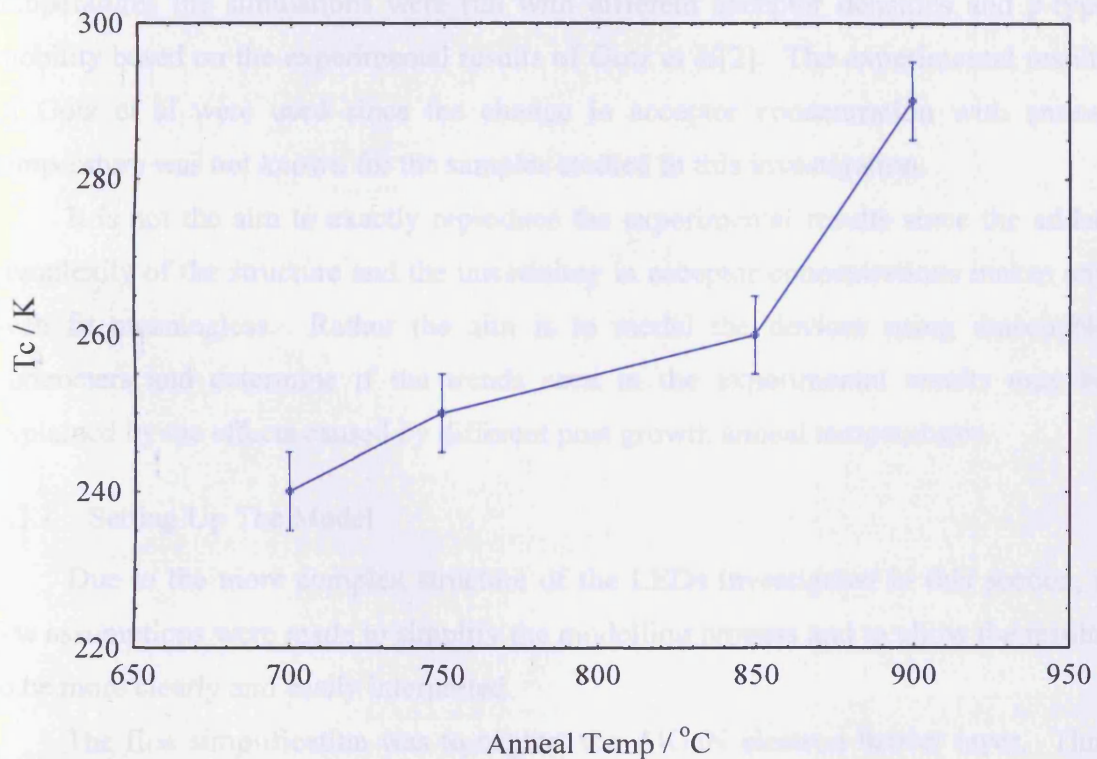
Figure 5.5 – Tc verses anneal temperature.

To recap, the absorption spectra, emission spectra and subsequently the IVL characteristics for a series of InGaN/GaN LEDs have been measured. All the LEDs tested were made from a single wafer with four different anneal temperatures (700, 750, 850 and 900°C) used to activate the p-type layers. Despite the different anneal temperatures the absorption and the emission spectra were similar for all devices, indicating annealing did not affect the quantum well band structure. The shape of the individual LI curves were also similar and appear to be linear or slightly super-linear.

However, the light output as a function of temperature, for a fixed current, was different for the different anneal temperatures. With the peak light output at a fixed current (Tc) moving to higher temperatures as the anneal temperature is increased. There is also an overall drop in the intensity of the light output at Tc as a function of increasing anneal temperature.

5.3 Simulations

In this section the trends seen in the experimental results of section 5.2 will be modelled using the same approach taken in chapter 4, that is the use of a drift-diffusion model to reproduce the LI characteristics and the value of light output at a fixed current density. To simulate the effect of different post growth anneal temperatures the simulations were run with different acceptor densities and p-type mobility based on the experimental results of Gotz et al[2]. The experimental results of Gotz et al were used since the change in acceptor concentration with anneal temperature was not known for the samples studied in this investigation.

It is not the aim to exactly reproduce the experimental results since the added complexity of the structure and the uncertainty in acceptor concentrations makes any such fit meaningless. Rather the aim is to model the devices using reasonable parameters and determine if the trends seen in the experimental results may be explained by the effects caused by different post growth anneal temperatures.

5.3.1 Setting Up The Model

Due to the more complex structure of the LEDs investigated in this section, a few assumptions were made to simplify the modelling process and to allow the results to be more clearly and easily interpreted.

The first simplification was to neglect the AlGaN electron barrier layer. This action was taken to avoid the need to include quantum mechanical effects (e.g. tunnelling, which is assumed to be effective) due to the barriers narrow width. Neglecting the AlGaN barrier also reduces the number of material parameters needed in the model. It was felt this action was justified since there is some debate over the effectiveness of AlGaN barriers at reducing leakage currents and also there is evidence for significant leakage currents in the experimental results of section 5.2.

The second simplification was to only model the device to the end of the first Mg-doped GaN layer after the QW (i.e. up to the wave-guide region). Again this

reduces the complexity and the number of material parameters needed in the model. This action was justified by the fact that due to the large E-field across this layer once an electron had been extracted as far as the wave-guide it was unable to return to the QW and thus contribute to the radiative process.

The highlighted cells in Table 5.1 indicate all the layers included in the simulations.

As in chapter 4 the QW was described using a triangular density of states (DOS) function, defined using the experimental absorption and emission spectra. The DOS is taken to extend from the lowest photon emission energy E_1 (2.73eV) to E_2 (3.20eV), which is assumed to be the energy of the lowest lying sub-band, as depicted in Figure 5.6.
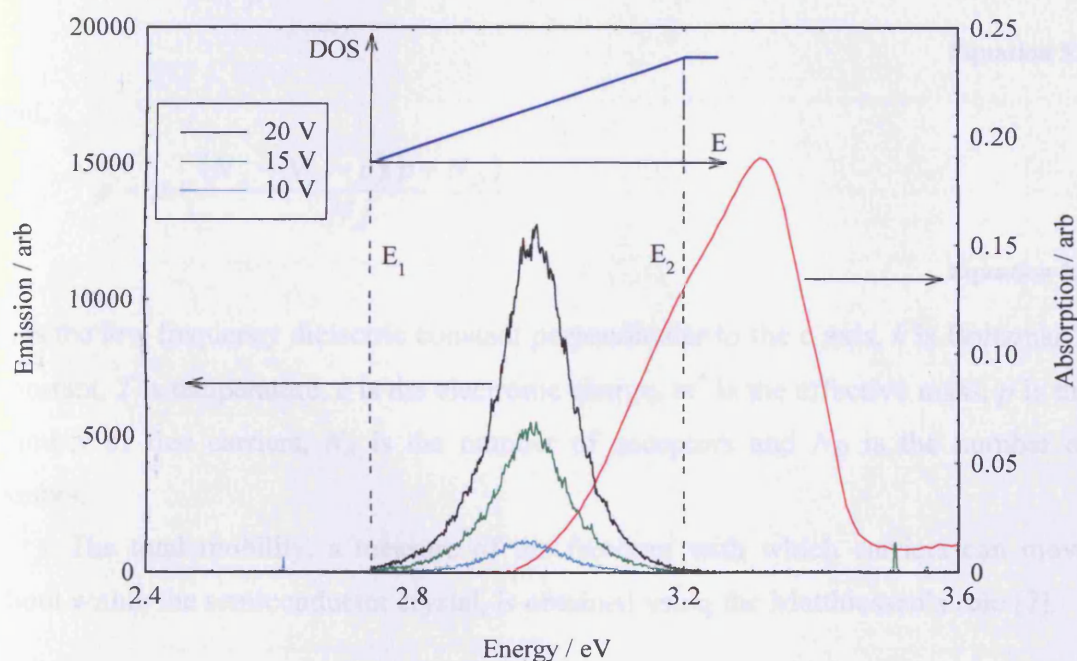
Figure 5.6 – Top absorption (right axis) and emission (left axis) spectra, both at room temperature, for a device annealed at 900°C. Inset shows a schematic diagram of the triangular density of states used in the computer simulation.

To simulate the effect of different anneal temperatures, three different acceptor concentrations (6×10^{17}, 6×10^{18} and 6×10^{19} cm^{-3}, corresponding to the hole concentrations in the experimental results of Gotz et al. [2]) were used in the simulations. As explained in chapter 1 annealing the p-type layer breaks the Mg-H complexes which passivate the material, however the freed hydrogen also has to be removed from the material since in its ionised state it acts a compensator. Thus there is no reason to expect the number of compensating donors to remain constant with

anneal temperature, therefore the number of donors are also assumed to increase with anneal temperature so the number of donors are assumed to be half the number of acceptors. The concentration of activated acceptors and donors also affect the temperature dependent hole mobility, via ionised impurity scattering, μ_{Ion} [6, 7].

$$\mu_{Ion} = \frac{128(2\pi)^{\frac{1}{2}} \varepsilon_s^{\ 2}(kT)^{\frac{3}{2}}}{e^3(m^*)^{\frac{1}{2}}(p+2N_A)}\left[\ln(1+b)-\frac{b}{1+b}\right]^{-1}$$

<div align="right">**Equation 5.1**</div>

where,

$$b = \frac{24m^*\varepsilon_s(kT)^2}{e^2\eta^2 p'}$$

<div align="right">**Equation 5.2**</div>

and,

$$p' = p + \frac{(N_A - N_D - p)(p + N_D)}{N_A}$$

<div align="right">**Equation 5.3**</div>

ε_s is the low frequency dielectric constant perpendicular to the c axis, k is Boltzman's constant, T is temperature, e is the electronic charge, m^* is the effective mass, p is the number of free carriers, N_A is the number of acceptors and N_D is the number of donors.

The total mobility, a measure of the freedom with which carriers can move about within the semiconductor crystal, is obtained using the Matthiessen's rule [7].

$$\mu_{total} = \left(\sum_i \frac{1}{\mu_i}\right)^{-1}$$

<div align="right">**Equation 5.4**</div>

where μ_{total} is the mobility and μ_i refers to the mobility calculated from the various scattering mechanisms. The different scattering mechanisms have different temperature dependencies and thus limit the mobility over different temperature ranges, therefore to accurately calculate the temperature dependence of the mobility for the different acceptor concentration all of the individual scattering mechanisms would need to be simulated. Given this and the uncertainty in GaN parameter values

the mobility used in the simulations was based on experimental results of Gotz et al. [8], Figure 5.7, thus accurately representing the corresponding variation in hole mobility with acceptor concentration. The experimental data was incorporated into the computer model by fitting each set of data points in Figure 5.7b with a set of polynomial equations, which were then used in the simulations. All other parameters used were the same as in chapter 4 (see Table 4.1) with the exception of the non-radiative lifetime in the QW. Using a value of 30ns (as in Table 4.1) produced superlinear LI curves consequently the non-radiative lifetime in the QW was reduced to 5ns. Reducing the non-radiative lifetime increases the non-radiative current, producing a more linear LI curve.
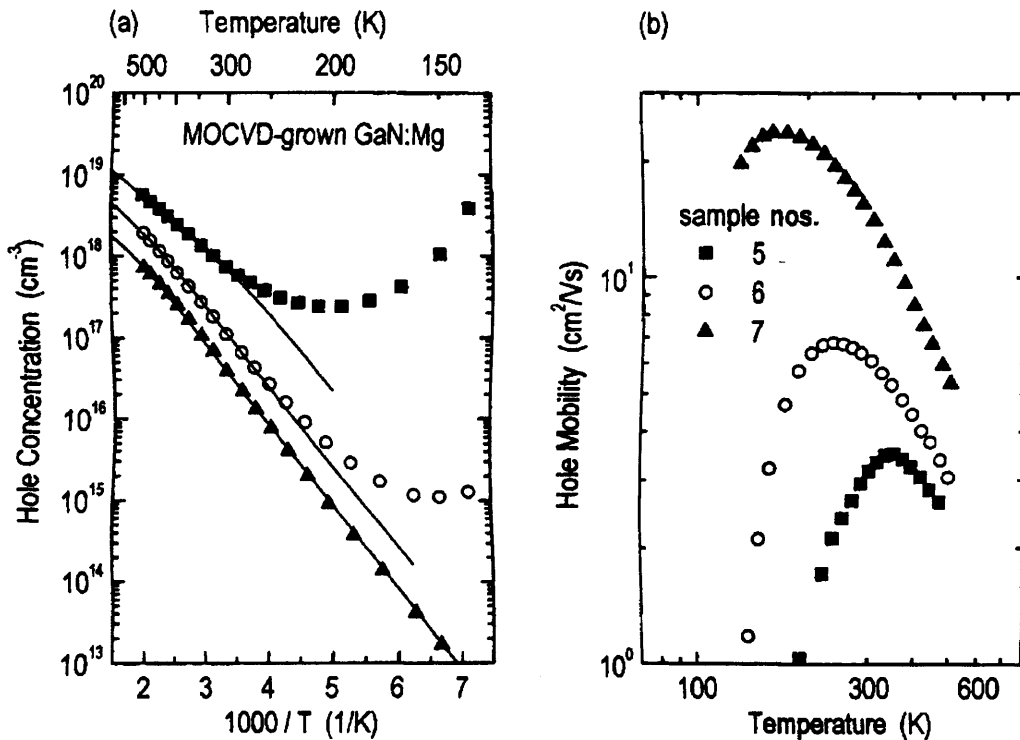
Figure 5.7 – Experimental results of Gotz et al. [2] a)Hole concentration versus reciprocal temperature and b)corresponding Hall mobility versus temperature.

5.3.2 Simulation Results

The aim of the simulations was to see if the trends visible in the experimental results, presented in section 5.2, could be explained in terms of the effects caused by different post growth anneal temperatures, namely, as the post growth anneal temperature is increased, the activated acceptor concentration increases, modifying

the hole mobility and shifting Tc (the peak light output at a fixed current density) to higher temperatures.

Three separate simulations were run for the three acceptor concentrations and corresponding hole mobilites presented in the experimental results of Gotz et al[2], which are reproduced in Figure 5.7. The results of the simulations are presented below in Figure 5.8b.

There are two discernible trends visible in Figure 5.8b. Firstly as the acceptor concentration is increased the value of Tc moves to higher temperatures. Secondly, there is an overall drop in the light intensity with increased acceptor concentration. Both of these trends are seen in the experimental results presented in Figure 5.4 which, have been combined in Figure 5.8a to allow easy comparison between simulated and experimental results.
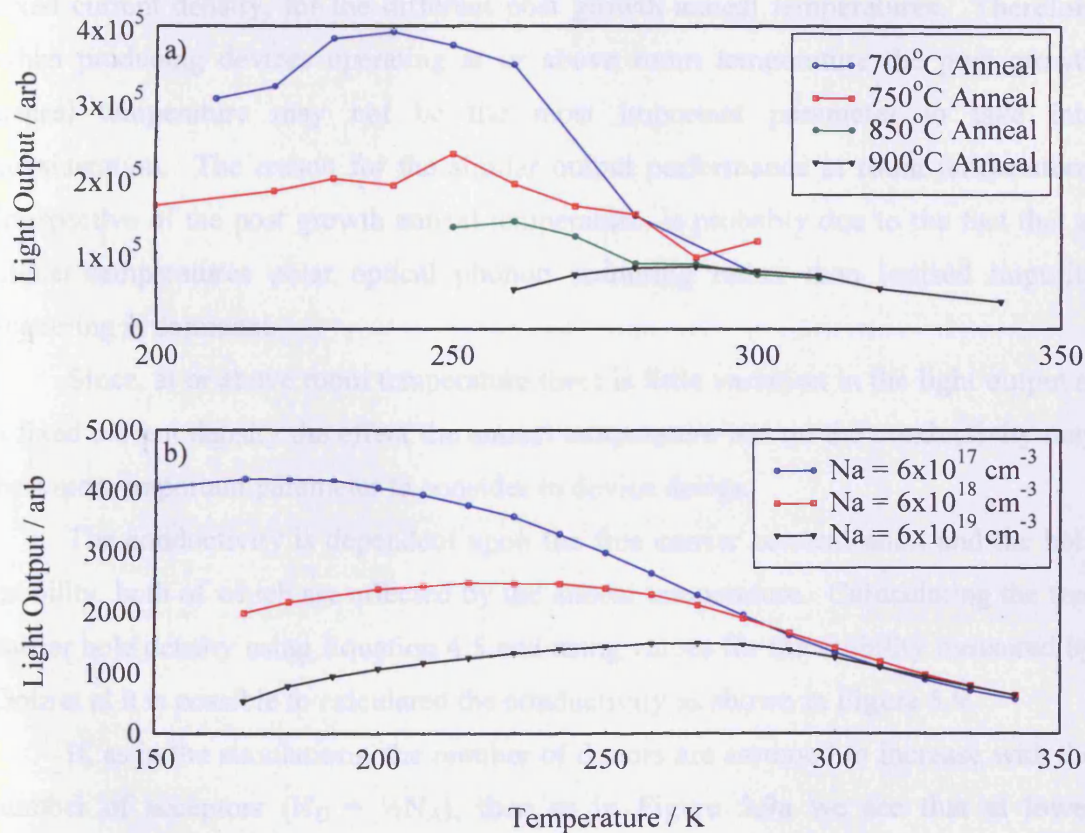

Figure 5.8 – Light output, at a fixed current, as a function of temperature. a) Experimental results for three separate anneal temperature and b) Simulated results for three separate acceptor concentrations.

There is clearly a degree of correlation between simulated and experimental results, strongly supporting the theory that the increase in Tc with anneal temperature

is a result of the increasing acceptor concentration and corresponding change in p-type mobility. Moreover it further backs up the claim, made in chapter 4, that leakage currents form a significant current path in GaN based devices and have an influential role on device characteristics.

Again it is important to state that without leakage currents in the model it would not be possible to reproduce the observed trends seen in the experimental data and that it is the balance between the E-Field in the p-type layer and the number of electrons thermally excited out of the QW that determines the leakage current.

As regards device design and performance if the device has to work at low temperatures then the 700°C anneal undoubtedly gives the highest light output intensity. On the other hand it is interesting to note that at and above room temperature there is little variation in the intensity of the measured light output, at a fixed current density, for the different post growth anneal temperatures. Therefore when producing devices operating at or above room temperature the post growth anneal temperature may not be the most important parameter to take into consideration. The reason for the similar output performance at room temperature, irrespective of the post growth anneal temperature, is probably due to the fact that at higher temperatures polar optical phonon scattering rather than ionised impurity scattering is dominant.

Since, at or above room temperature there is little variation in the light output at a fixed current density the effect the anneal temperature has on the conductivity may be a more important parameter to consider in device design.

The conductivity is dependent upon the free carrier concentration and the hole mobility, both of which are affected by the anneal temperature. Caluculating the free carrier hole density using Equation 4.5 and using values for the mobility measured by Gotz et al it is possible to calculated the conductivity as shown in Figure 5.9.

If, as in the simulations, the number of donors are assumed to increase with the number of acceptors ($N_D = \frac{1}{2}N_A$), then as in Figure 5.9a we see that at lower temperatures, below 350K, the conductivity decreases as the anneal temperature is increased. This decrease leads to an increase in the E-field across the p-layer and consequently an increase in the leakage current, which intern leads to a decrease in the light output at a fixed current density.

If the number of compensating donors were unaffected by anneal temperature and remained constant the conductivity would be dominated by the increases in the

free carrier density with anneal temperature, over the entire temperature range, this is illustrated in Figure 5.9b. Such an increase in the conductivity would lead to a decrease in the E-field across the p-type layer and a reduction of the leakage current, hence the light output at a fixed carrier density would increase with increased anneal temperature. However this trend is not seen in the experimental results, supporting the assumption, made in the simulations, that in the measured devices the number of donors must increase along with the number of acceptors as the anneal temperature is increased.
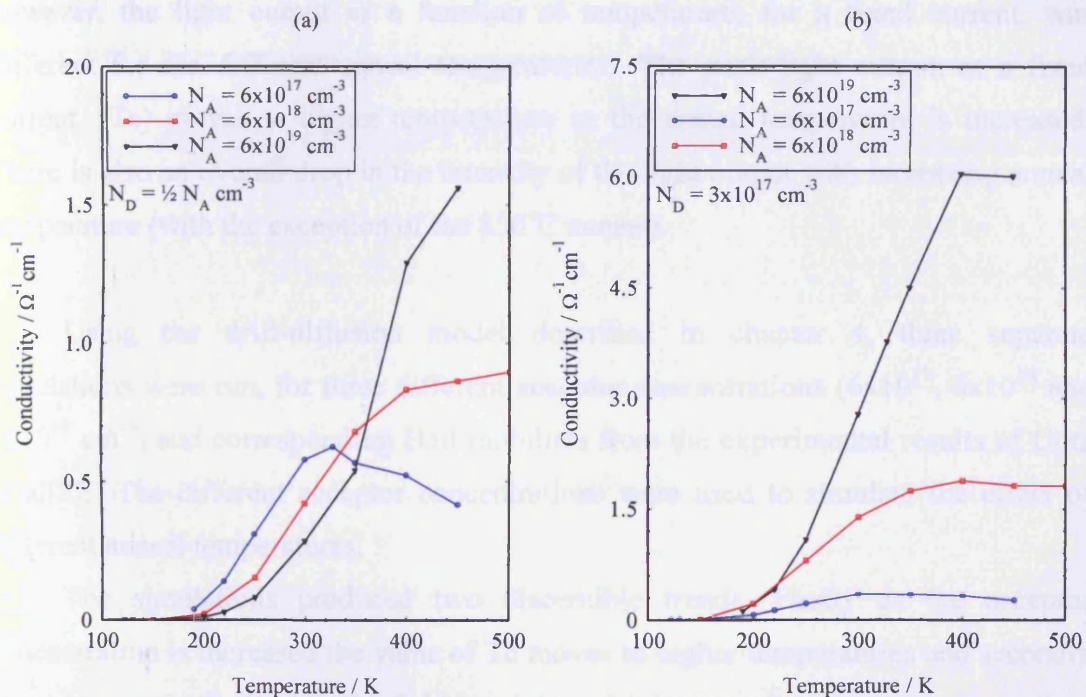

Figure 5.9 – Calculated p-type conductivity using values for the mobility measured by Gotz et al and free carrier densities determined using Equation 4.5 a) assuming the number of compensating donors increase with anneal temperature and b) assuming the number of compensating donors remains constant.

5.4 Summary

The absorption spectra, emission spectra and IVL characteristics for a series of InGaN/GaN LEDs have been measured. All the LEDs tested were made from a single wafer with four different anneal temperatures (700, 750, 850 and 900°C) used to activate the p-type layers.

The absorption and the emission spectra were similar for all the devices across all anneal temperatures. The shape of the individual LI curves were also similar however, the light output as a function of temperature, for a fixed current, was different for the different anneal temperatures. The peak light output, at a fixed current, (Tc) moves to higher temperatures as the anneal temperature is increased. There is also an overall drop in the intensity of the light output with increasing anneal temperature (with the exception of the 850°C anneal).

Using the drift-diffusion model described in chapter 4, three separate simulations were run, for three different acceptor concentrations (6×10^{17}, 6×10^{18} and 6×10^{19} cm^{-3}) and corresponding Hall mobilites from the experimental results of Gotz et al[2]. The different acceptor concentrations were used to simulate the effect of different anneal temperatures.

The simulations produced two discernible trends. Firstly as the acceptor concentration is increased the value of Tc moves to higher temperatures and secondly there is an overall drop in the light intensity with increased acceptor concentration. Both of these trends were seen in the experimental results and there is clearly a great deal of correlation between simulated and experimental results. This strongly supports the hypothesis that the increases in Tc with anneal temperature is a result of the increased acceptor concentration and corresponding change in p-type mobility. It also demonstrates the robustness of the drift-diffusion model used in the simulations and further illustrates the significance of leakage currents within GaN based devices. Since without the inclusion of leakage currents it would not be possible to reproduce the observed trends seen in the experimental data.

The number of activated acceptors within the p-doped regions is strongly dependent on the anneal temperature, increasing the anneal temperature increases N_A increasing the number of free carriers. Increasing N_A also has the effect of reducing

the overall mobility and moving the peak mobility to higher temperatures. These three factors have a strong influence on the conductivity, which in turn, affects the E-field in the p-doped layer. Since it is the balance between the E-field in the p-doped layer and the number of electrons thermally excited out of the QW, which determines Tc and only the E-field is affected by the increase in N_A, samples from the same piece of wafer annealed at different temperatures should have different values of Tc.

5.5 References

1.   D. Lancefield, A. Crawford, B. Beaumont, P. Gibart, M. Heuken, and M. Di Forte-Poisson, *Temperature dependent electroluminescence in GaN and InGaN/GaN LEDs*. Materials Science and Engineering B-Solid State Materials for Advanced Technology, 2001. **82**(1-3): p. 241-244.

2.   W. Gotz and N.M. Johnson, *Characterization of Dopants and Deep Level Defects*, in *Gallium Nitride (GaN) II*, J.I. Pankove and T.D. Moustakas, Editors. 1998, Academic: New York.

3.   H.K. Cho, J.Y. Lee, J.H. Song, P.W. Yu, G.M. Yang, and C.S. Kim, *Influence of strain-induced indium clustering on characteristics of InGaN/GaN multiple quantum wells with high indium composition*. Journal of Applied Physics, 2002. **91**(3): p. 1104-1107.

4.   Y. Narukawa, Y. Kawakami, M. Funato, S. Fujita, and S. Nakamura, *Role of self-formed InGaN quantum dots for exciton localization in the purple laser diode emitting at 420 nm*. Applied Physics Letters, 1997. **70**(8): p. 981-983.

5.   J.A. Davidson, P. Dawson, T. Wang, T. Sugahara, J.W. Orton, and S. Sakai, *Photoluminescence studies of InGaN/GaN multi-quantum wells*. Semicond. Sci. Technol., 2000. **15**(6): p. 497-505.

6.   D.C. Look, *Electrical Characterization of GaAs Materials and Devices*. Design and Measurement in Electronic Engineering, ed. D.V. Morgan and H.L. Grubin. 1989, Bury St. Edmunds: John Wiley & Sons.

7.   H. Morkoc, *Nitride Semiconductors and Devices*. 1999, Berlin: Springer.

8.   W. Gotz, N.M. Johnson, J. Walker, D.P. Bour, and R.A. Street, *Activation of acceptors in Mg-doped GaN grown by metalorganic chemical vapor deposition*. Applied Physics Letters, 1996. **68**(5): p. 667-669.

6 Summary and Future Work

6.1 Summary of Findings

The main findings described in this thesis are summarised below:

6.1.1 Determining the Piezoelectric Field

Large differences are reported in the literature between experimentally determined and theoretically calculated piezoelectric fields in nitride structures[1]. Since this is one of the key features of the physics of nitride devices and since we need to know the strength of the piezoelectric field in order to predict LED and laser performance we used reverse bias photocurrent absorption to determine the strength of the piezoelectric field within a set of InGaN/GaN QW devices. The reverse bias needed to obtain a square QW was determined to be 8.5V and using an equation for the depletion width appropriate for a p-i-n structure, the piezoelectric field within the QW was determined to be (1.9 ± 0.15) MVcm^{-1}, in good agreement with the value of 1.8 MVcm^{-1}[2] calculated theoretically using values for the piezoelectric coefficients interpolated from the binary values of InN and GaN. We suggest that calculation of the piezoelectric effect in GaN based LEDs and laser diodes should be done using piezoelectric coefficients determined from the binaries as the best available description of expected behaviour.

6.1.2 Evidence for Localised States

There are two pieces of evidence that suggest the presence of localised regions within the QW due to inhomogeneities in the active region.

The peak wavelength as a function of temperature was measured and fitted using the Varshni equation. Using parameter values interpolated from the binaries it is impossible to obtain a fit to the experimental data using the Varshni equation if an In concentration of 16% (the value obtained by X-ray diffraction) is used, since the interpolated bandgap energy of 2.96 eV, is too large. The calculated bandgap energy (2.90 eV at 300K) is also larger than the observed peak in the spontaneous emission, which occurs at 2.58 eV and corresponds to an indium concentration 26.4% (as

interpolated from the binaries). Using this indium concentration a good fit to the experimental data can be achieved, suggesting the presence of localised regions in the QW due to the clustering of indium during growth.

Secondly, the photocurrent absorption was measured. Above 2.90 eV, the calculated bandgap energy for an $In_{0.16}Ga_{0.84}N$ QW, the absorption spectrum flattens out, before increasing again as the bandgap of GaN is approached. However there is no well-defined absorption edge to the low energy side of the QW, rather there was an absorption tail which extended to low energies and which corresponds the peak emission, suggesting that the QW is inhomogeneous, due for example to composition fluctuations or well width non-uniformity[3] and that the radiative emission is occurring from these regions.

6.1.3 Light-Current Characteristics

The light-current (LI) characteristics of InGaN/GaN QW LEDs were investigated as function of current and temperature . All the LEDs examined in chapter 3 had sublinear LI curves at all temperatures while in chapter 5 more linear LI curves were measured however both exhibited a distinctive temperature dependence; the light output at a fixed current density initially increases with increasing temperature, reaches a maximum value at 250K and then decreases for subsequent increases in temperature. Both the sub-linear behaviour and the temperature dependence would be expected to occur in the presence of thermally activated drift leakage currents.

6.1.4 Leakage Currents

It was postulated that the sublinear light-current curves and their distinctive temperature dependence may be explained via thermally activated leakage currents through the p-doped layers. To test the validity of the postulate the light-current characteristics were simulated using a drift diffusion model.

Results from the model showed the sublinear light-current curves and their distinctive temperature could be explained by the influence of the large acceptor ionisation energy on electron leakage by drift through the p-GaN cap layer. However, it was only possible to achieve detailed agreement with experimental LI data and emission spectra by using a non-square density of states function, characteristic of an inhomogeneous quantum well. This has the effect of giving emission at the observed

wavelength while placing the quasi-Fermi energy sufficiently close to the conduction band of the p-GaN layer for the leakage current to make a significant contribution to the total current. Carrier leakage would be insignificant in the modelled structure for uniform wells emitting at the observed photon energy. This highlights the profound effect of localisation on the behaviour of GaN based LEDs, in particular their LI characteristics and the importance of including such effects when modelling these devices. It is also important to stress that without the leakage of carriers in the model it would not be possible to reproduce the observed temperature dependence, of the light output at a fixed current density, seen in the experimental results.

6.1.5 Effect of Anneal Temperature

The annealing of the p-type layers is an essential processing step in the fabrication of GaN based devices. To examine the affect anneal temperature has on device performance the absorption spectra, emission spectra and IVL characteristics for a series of InGaN/GaN QW laser structures (operated as LEDs) were measured. All the LEDs tested were made from a single wafer however four different anneal temperatures (700, 750, 850 and 900°C) were used to activate the p-type layers.

The measured absorption and emission spectra were similar for all the devices across all anneal temperatures and the shape of the individual LI curves were also similar, however the light output as a function of temperature, for a fixed current, was different for the different anneal temperatures. It was found that peak light output, at a fixed current (Tc), moves to higher temperatures as the anneal temperature is increased, there was also an overall drop in the intensity of the light output with increasing anneal temperature. It was postulated that the increases in Tc was a consequence of an increase in the strength of the leakage current brought about by the increased acceptor concentration and corresponding change in p-type mobility with increased anneal temperature.

To test this hypothesis the drift-diffusion model, described in chapter 4, was used. The simulations produced two discernible trends. Firstly as the acceptor concentration is increased the value of Tc moves to higher temperatures and secondly there is an overall drop in the light intensity with increased acceptor concentration, both of which are seen in the experimental results.

From the simulations it was concluded that the increase in anneal temperature leads to an increase in the number of activated acceptors and donors within the p-

doped regions, and a corresponding reduction in the overall mobility with the peak mobility moving to higher temperatures. The combined affect is a relative decrease in the conductivity, which leads to an increase in the E-field in the p-doped layer at a given temperature and current density. The balance between the E-field in the p-doped layer and the number of electrons thermally excited out of the QW determines the value of Tc and since the E-field increases with anneal temperature the value of Tc also increases.

This demonstrates the robustness of the drift-diffusion model used in the simulations and further illustrates the significance of leakage currents within GaN based devices. Also since the devices tested were fabricated from a laser structure it shows that even with the inclusion of barrier layers, designed to stop carrier leakage, leakage currents play an influential role in device performance. Thus the effects of leakage currents need to be considered when designing GaN based lasers.

6.2   Future Work

The work done modelling the light-current characteristics within this thesis is useful for determining the physical processes occurring within devices. However if the models are to be used to accurately reproduce device characteristics, helping to design more efficient devices, a greater accuracy is needed when measuring the fundamental properties of GaN devices. For example at present it is difficult to accurately measure the acceptor concentration in p-doped layers, yet work done in chapter 5 shows the value of the acceptor concentration has a significant effect on the strength of the light output at a fixed current density. The value of the acceptor concentration is also important when determining the value of the piezoelectric field using reverse bias photocurrent absorption as described in chapter 2. It is essential that more work be carried out in accurately determining the dopant concentrations in GaN based devices if the modelling of device characteristics is to progress to the levels seen in GaAs based devices.

Another important part of the modelling is based about the assumption light is emitted from localised regions which form a band tail in the absorption spectra. For simplicity within the model the density of states produced by this band tail was assumed to be triangular, however in reality the density of states are more likely to have an exponential form. Thus more work is needed to determine exactly what

effect localised regions have on the density of states and how they may best be described.

Although the work described in this thesis (using LEDs and laser structures operated as LEDs) and the conclusions drawn are of direct relevance to LED performance it is also relevant to all laser diodes fabricated from GaN based material. In addition to the work presented in this thesis experiments were performed on the samples described in chapter 2 to measure the modal gain using multisection techniques developed by Thomson et al. [4]. However due to poor confinement of the optical mode, leakage of carriers and device processing (50μm oxide stripe) it was not possible to achieve a high enough carrier density to overcome the losses and obtain optical gain[5]. It is suggested that future work aimed at measuring the modal gain should use devices processed with ridges, as this will help with the lateral confinement of the optical mode and enable larger current density to be achieved. The loss of light into the substrate was also a major problem, thus future devices will need more effective waveguides. This may be obtained by using thicker cladding layers with larger aluminium compositions, however increasing the Al composition and thickness can lead to cracking within the device. To avoid the problem of cracking repeats of thinner high/low Al composition layers can be used to form a super-lattice structure with an average refractive index of the two layers[6-8]. Alternatively indium can be added to the layers to help compensate the build up of strain[9].

Experiments to measure the modal gain were also performed at reduced temperature in an attempt to increase the confinement of the carriers. However as the devices were cooled their resistance increased and they were prone to shorting and catastrophic failure, believed to be the result of metal migrating through the device down cracks and threading dislocations in the material. The quality of device contacts was also an issue when performing reverse bias photocurrent absorption measurements as many of the devices had a tendency to short out under reverse bias conditions. This highlights the problem of the current contact technology and work is needed to improve this area of device performance.

In conclusion the major problems holding back the research into optical gain in electrically pumped III – Nitride materials are poor confinement of the optical mode, poor contact technology and device reliability. Further technological development is

necessary if the performance of GaN based devices manufactured at university level is to match that of the current commercially available devices produced by industry.

6.3 References

1. T. Takeuchi, C. Wetzel, S. Yamaguchi, H. Sakai, H. Amano, I. Akasaki, Y. Kaneko, S. Nakagawa, Y. Yamaoka, and N. Yamada, *Determination of piezoelectric fields in strained GaInN quantum wells using the quantum-confined Stark effect.* Applied Physics Letters, 1998. **73**(12): p. 1691-1693.

2. I.H. Brown, I.A. Pope, P.M. Smowton, P. Blood, J.D. Thomson, W.W. Chow, D.P. Bour, and M. Kneissel, *Internal Field Effects in InGaN Quantum Wells.* Submitted to Applied Physics Letters.

3. J.A. Davidson, P. Dawson, T. Wang, T. Sugahara, J.W. Orton, and S. Sakai, *Photoluminescence studies of InGaN/GaN multi-quantum wells.* Semicond. Sci. Technol., 2000. **15**(6): p. 497-505.

4. J.D. Thomson, H.D. Summers, P.J. Hulyer, P.M. Smowton, and P. Blood, *Determination of single-pass optical gain and internal loss using a multisection device.* Applied Physics Letters, 1999. **75**(17): p. 2527-2529.

5. H.D. Summers, P.M. Smowton, P. Blood, M. Dineen, R.M. Perks, D.P. Bour, and M. Kneissel, *Spatially and spectrally resolved measurement of optical loss in InGaN laser structures.* Journal of Crystal Growth, 2001. **230**(3-4): p. 517-521.

6. M. Hansen, A.C. Abare, P. Kozodoy, T.M. Katona, M.D. Craven, J.S. Speck, U.K. Mirhra, L.A. Coldren, and S.P. DenBaars, *Effect of AlGaN/GaN Strained Superlattice Period on InGaN MQW laser diodes.* Mrs Internet Journal of Nitride Semiconductor Research, 2000. **5**(S1): p. W1.4.

7. J. Zhang, *Crack-free thick AlGaN grown on sapphire using AlN/AlGaN superlattices for strain management.* Applied Physics Letters, 2002. **80**(19): p. 3542-3543.

8. T. Whitaker, *SUVOS pushes UV LEDs and lasers to shorter wavelengths,* in *Compound Semiconductor.* 2004.

9. J.F. Carlin and M. Ilegems, *High-quality AlInN for high index contrast Bragg mirrors latticed matched to GaN.* Applied Physics Letters, 2003. **83**(4): p. 668-670.